

Cluster Explosions
and
Characterization of Ultrashort
XUV Pulses

VRIJE UNIVERSITEIT

Cluster Explosions
and
Characterization of Ultrashort
XUV Pulses

ACADEMISCH PROEFSCHRIFT

ter verkrijging van de graad van doctor aan
de Vrije Universiteit Amsterdam,
op gezag van de rector magnificus
prof.dr. T. Sminia,
in het openbaar te verdedigen
ten overstaan van de promotiecommissie
van de faculteit der Exacte Wetenschappen
op donderdag 21 februari 2002 om 13.45 uur
in het hoofdgebouw van de universiteit,
De Boelelaan 1105

door

Elena-Simona Toma

geboren te Boekarest

promotor: prof.dr. H.G. Muller

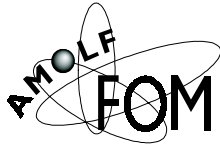
This thesis is based on the following publications:

- Chapter 2 *Resonance-enhanced high-harmonic generation*
E.S. Toma, Ph. Antoine, A. de Bohan, H.G. Muller
J. Phys. B 32, 5843 (1999)
- Chapter 3 *Ponderomotive streaking of the ionization
potential as a method for measuring pulse
durations in the XUV domain with fs resolution*
E.S. Toma, H.G. Muller,
P.M. Paul, P. Breger, M. Cheret, P. Agostini,
C. Le Blanc, G. Mullot, G. Cheriaux
Phys. Rev. A 62, 061801(R) (2000)
- Chapter 4 *Observation of a Train of Attosecond Pulses
from High Harmonic Generation*
P.M. Paul, E.S. Toma, P. Breger, G. Mullot,
F. Auge, Ph. Balcou, H.G. Muller, P. Agostini
Science 292, 1689 (2001)
- Chapter 5 *Laser disintegration of Van-der-Waals clusters
of carbon-containing molecules*
E.S. Toma, H.G. Muller
submitted to Phys. Rev. A
- Chapter 6 *X-ray emission after laser disintegration
of clusters of carbon-containing molecules*
E.S. Toma, H.G. Muller
to be submitted

The author also participated in the following publication:

- Population transfer via adiabatic passage in the rubidium
quantum ladder system*
D.J. Maas, C.W. Rella, P. Antoine, E.S. Toma, L.D. Noordam
Phys. Rev. A 59, 1374 (1999)

The experiments described in this thesis were performed at the following institutes:



FOM Institute for Atomic and Molecular Physics
Kruislaan 407
1098 SJ, Amsterdam, The Netherlands

ENSTA, Laboratoire d'Optique Appliquee
Ecole Polytechnique
91761 Palaiseau Cedex, France

This work is part of the research program of the Stichting voor Fundamenteel Onderzoek der Materie (Foundation for Fundamental Research on Matter) and was made possible by financial support from the Nederlandse Organisatie voor Wetenschappelijk Onderzoek (Netherlands Organization for the Advancement of Research).

ISBN: 90-9015483-3

Contents

1	Introduction	9
1.1	Ionization mechanisms	10
1.2	High-harmonic generation	13
1.3	Double ionization	18
1.4	Stabilization	22
1.5	X-ray lasers	23
I	High-Harmonic Generation	27
2	Resonance-enhanced HHG	29
2.1	Introduction	29
2.2	Experimental setup	31
2.3	Results and discussion	33
2.4	Conclusions	37
3	Ponderomotive streaking	39
3.1	Introduction	39
3.2	Description of the method	40
3.3	Experimental setup	42
3.4	Results and discussions	43
3.5	Conclusions	45
4	Reconstruction of attosecond beatings	47
4.1	Introduction	47
4.2	Theoretical description	49
4.3	Setup and results	51
4.4	Conclusions	54

II	Cluster Explosions	57
5	Production of highly charged ions	59
5.1	Introduction	59
5.2	Cluster-size determination	61
5.3	Cluster explosion	66
5.3.1	CO ₂	66
5.3.2	C ₃ H ₈	68
5.4	Theoretical model of the explosion	70
5.5	Conclusions	77
6	X-ray emission from cluster debris	79
6.1	Introduction	79
6.2	Experimental setup	80
6.3	Results	81
6.3.1	CO ₂	83
6.3.2	C ₃ H ₈ . Auger decay in argon	86
6.4	Conclusions	90
	Bibliography	93
	Summary	101
	Samenvatting	105
	Acknowledgment	109
	Curriculum Vitae	111

Chapter 1

Introduction

The interaction between atoms and electromagnetic radiation has become a point of interest in physics since the first detection of the photoelectric effect in the experiments performed by Hertz at the end of the XIX-th century, in order to prove the existence of electromagnetic waves. The emission of electrons at the interaction of photons with metals was successfully explained by Einstein in 1905 in terms of Planck's hypothesis, which states that the electromagnetic radiation has a discrete structure, each photon carrying a certain amount of energy and momentum, given by the wave frequency. As the studies of the atomic structure of matter and the advancements in the newly born quantum theory were progressing, the effect of photoionization was discovered and explained. The energy of a free electron can take any positive value. But once the electron is bound to an atom, the condition that its wavefunction is finite and continuous results in discrete negative values for the electron energy (the energy levels of the atom). The photoionization theory states mainly that if the photon energy is larger than the absolute binding energy of the electron in the atom, there is a finite probability that the electron is released into the continuum (becomes free) by absorption of one photon. In the quantum description, the ionization rate of the atom is given by Fermi's "golden rule":

$$\Gamma = \frac{2\pi}{\hbar} |\langle \Psi_f | H_{\text{int}} | \Psi_i \rangle|^2 \rho(K). \quad (1.1)$$

In this expression, Ψ_f is the wavefunction of the final state, Ψ_i of the initial state, and ρ is the density of states in the continuum at the energy K of the ejected electron. The Hamiltonian H_{int} of the interaction with the electric field is proportional with the field strength E , so the rate is increasing linearly with intensity as long as the initial state is not depleted. This description applies to weak electric fields, for which the electric force is smaller than the atomic force binding the electron to the nucleus, and the

1.1. Ionization mechanisms

interaction can be treated as a perturbation to the atomic Hamiltonian. The discovery of light amplification by stimulated emission of radiation (LASER) in the middle of the XX-th century and the development of intense sources of laser radiation resulted in the observation of new non-perturbative effects in the atom-light interaction. We shall describe some of those in the next paragraphs.

The discussion will take place in the frame of the dipole approximation, which states that the electric field is homogeneous over the volume of the atom. This implies a negligible magnetic field, which is a correct assumption because, in the problems to follow, the electron does not reach relativistic speeds.

1.1 Ionization mechanisms

Subject to an infrared radiation of low frequency, such that the photon energy is less than the ionization potential of the atom, the atom can still be ionized by absorption of multiple photons [1,2]. The process is called multiphoton ionization (MPI), and the free electrons are detected with the energy $n\hbar\omega - I_p$, I_p being the ionization potential of the atom, and ω the (angular) laser frequency. If the electric field is weak, the interaction can be described with perturbation theory of higher order, applied to a bound-free transition. The ionization rate is then given by $\Gamma_n = \sigma_n I^n$, where n is the minimum number of photons needed for ionization, I is the light intensity and σ is the generalized ionization cross section. The yield ($\sim 1 - \exp(-\Gamma_n \tau)$) saturates if τ , the duration of the pulse, is long enough such that all the atoms in the focus are depleted and no ionization takes place anymore. Increasing the peak intensity more does not change anything in the yield, as long as the interaction remains perturbative. The occurrence of a resonance, when $m(< n)$ electrons hit an excited state, complicates the description of the process. As the intensity increases, the bound states of the atom shift in energy under the influence of the electric field, and the interaction becomes non-perturbative. This shift is called AC-Stark shift, and the magnitude of the energy change depends on the coupling between the atomic states and the laser field, which is higher for weakly bound states. The ground state is hardly perturbed, and in many situations the ground-state shift can be neglected, but the Rydberg states of the atom and the continuum states shift by a significant amount that approximately equals the cycle-averaged kinetic energy of a free electron oscillating in the laser field [91]. This also called ponderomotive energy is given by

$$U_p = \frac{e^2 E_0^2}{4m_e \omega^2} \quad (1.2)$$

(for non-relativistic velocities), where E_0 is the amplitude of the electric field $E(t) = E_0(t) \sin(\omega t)$, and e and m_e are the charge and respectively the mass of the electron. (In practical units this is $U_p[\text{eV}] = 9.33 \times 10^{-14} I[\text{W}/\text{cm}^2] \lambda^2[\mu\text{m}]$, λ being the wavelength.)

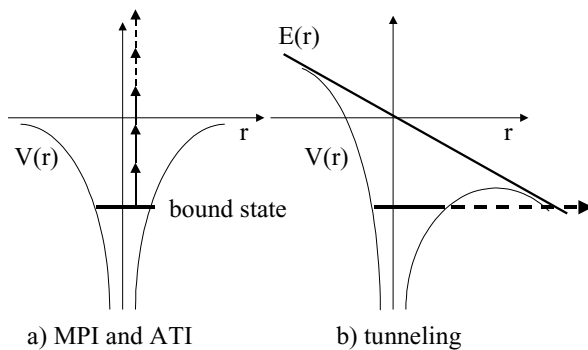


Figure 1.1: *Different photoionization mechanisms. The atomic potential is represented as a function of the distance from the core. At low intensities, the ionization takes place mainly via multiphoton processes: MPI and ATI. At high intensities, the potential is distorted by the laser electric field $E(r)$, and the main mechanism is tunneling through the potential barrier (or even ionization over the barrier at extreme intensities).*

The perturbative approach becomes non-valid as soon as U_p is of the order of the photon energy ($U_p \geq \hbar\omega$). At intensities above 10^{13} W/cm² ionization with photons in excess (s , the number of absorbed photons, $> n$, the minimum number of photons needed for ionization) was observed [3], and the process was named, somehow pleonastically, above-threshold ionization (ATI) (see Fig. 1.1a). The spectrum shows narrow peaks spaced by one photon energy, whose magnitudes do not follow the usual power law ($\sim I^s$). For pulses longer than 10 ps (the approximate time it takes the electron to leave the laser focus), the electron gains back the ponderomotive energy by travelling down on the potential slope created by the spatial distribution of the field, and the $U_p(I)$ shift is not detected in the spectrum. This means that the position of the peaks is not intensity dependent, but the peaks can change in magnitude as a function of intensity, even disappearing as the ionization channels close because of larger ponderomotive shifts of the ionization threshold. During short, femtosecond laser pulses, the electron does not have time to move a significant distance in the focus and the $U_p(I(t))$ shift is detectable in the electron spectrum. The ATI peaks move to lower energies as the maximum intensity is increased and exhibit a resonant substructure that peaks up each time excited states of the atom are Stark-shifted into multiphoton resonance during the pulse [4–6].

If the intensity is further increased, such that U_p approaches in magnitude the ionization potential of the atom, the electric field becomes strong enough to tilt the ionization threshold in the direction of the laser polarization, creating a potential

1.1. Ionization mechanisms

barrier which the electron can tunnel through, or even escape over if the threshold is lowered enough [7, 8] (see Fig. 1.1b). The condition for tunneling ionization is given by $\gamma < 1$, where the adiabaticity parameter γ equals $\sqrt{I_p}/2U_p$ [9]. The electrons are released with almost zero initial velocity, and accelerated by the field along the polarization axis. The large ponderomotive shifts smoothen out the ATI peaks in the spectrum, although they could still be visible in a single-intensity experiment. The tunneling rate is roughly proportional to $\exp(-\text{const} \frac{(2I_p)^{3/2}}{E})$, increasing exponentially with E if E is weaker than required to suppress the potential barrier [138]. The rate expression changes for over-the-barrier ionization. In a classical approach, considering that no ionization occurs before the barrier is suppressed, the threshold intensity is given by:

$$I_{\text{OTBI}}[\text{W}/\text{cm}^2] = 4 \times 10^9 \frac{I_p^4[\text{eV}]}{Z^2}, \quad (1.3)$$

where Z is the charge of the final state (multiple ionization can occur, and I_p changes accordingly) [109].

The envelope of the ATI spectrum can be explained in an intuitive way with a two-step model [10, 11, 52] which assumes in the first step that the electron is ionized via MPI or tunneling in the vicinity of the parent ion and then treats classically the motion of the free electron in the laser field. After having been released from the atomic potential well at the moment t_0 with an initial velocity v_0 , the free electron is driven by the laser field (assumed linearly polarized) in an oscillatory motion with the total velocity $v_0 + 2\sqrt{U_p/m}(\cos\omega t - \cos\omega t_0)$. The cycle-averaged kinetic energy in the focus is then given by:

$$K = K_0 + U_p + 2U_p \cos^2 \omega t_0 - \sqrt{8U_p K_0} \cos \omega t_0, \quad (1.4)$$

where the first term, $K_0 = (m_e/2)v_0^2$, is the initial kinetic energy, the second term, U_p , is the ponderomotive (quiver) energy, and the subsequent terms give the drift energy [108]. In case of zero initial velocities, the maximum energy the electron can get on the detector is $3U_p$ for long pulses (picosecond range), and $2U_p$ for femtosecond pulses (for which the electron does not retain the ponderomotive energy on leaving the focus). If $K_0 \neq 0$, the cross-term adds its contribution to the energy spectrum and the ATI envelope expands to larger energies.

If the electric field is circularly polarized, the electron drift velocity has a constant transversal component that drives the electron away from the parent ion. If the laser field is linearly polarized, there are two types of electron trajectories: those that return to the nucleus and those that escape to infinity. Which kind of trajectory occurs depends on the field phase at the moment of ionization (see Fig. 1.2). Electrons that are released at maximum value of the field or immediately after it, with small

initial velocities, do return at least once to the core. When the electron returns to the nucleus (the recollision stage of the classical model), several things can happen to it:

- (i) it can elastically scatter (with backscattering as a special case).
- (ii) inelastically scatter, losing energy by ionization or excitation of the atom, or by emission of radiation.
- (iii) it can be recaptured by the atom, the energy difference being released as a photon of high energy. This last situation is referred to as high harmonic generation (HHG), because the radiation emission occurs at multiple frequencies of the driving infrared field.

Electrons that backscatter on the core (i) show up in the ATI spectrum at high energies. The collision is elastic, but it helps the electrons to "rephase" themselves in the laser field, from which they gain additional drift velocity. This way of gaining energy in the presence of a laser field is called inverse bremsstrahlung. After the collision, at moment t_r and angle θ , the cycle-averaged drift energy is (if $K_0 = 0$):

$$K_{\text{drift}} = 2U_p \cos^2 \omega t_0 + 8U_p \frac{1 - \cos \theta}{2} (\cos^2 \omega t_r - \cos \omega t_r \cos \omega t_0). \quad (1.5)$$

The laser phase at ionization time determines the return time. The maximum K_{drift} is $10U_p$, at $\theta = 180^\circ$ (backscattering at the first return of the electron) [108].

It was expected that the angular distributions of the electrons is more peaked along the laser polarization axis for higher energies, because higher angular-momentum states are favored by absorption of more photons. This turns out to be true, except for very high-energy electrons whose angular distributions show narrow rings 45° off the polarization axis [65]. The energy range where this happens is intensity dependent and it is centered around $8U_p$, which means that backscattered electrons are involved in the process. Calculations done in the single-electron approximation could reproduce the scattering rings and suggest a quantum interference interpretation. Nevertheless classical calculations of Paulus *et al.* [11], based on the two-step model, predicted from a uniform distribution of t_0 and θ , the apparition of lobes at 30° for electrons of $8U_p$ energy. Only first-return times were considered in the calculation, but electrons born between the peak of the field and $t_0 = 0.285T$ ($\omega t_0 = 102.55^\circ$) can return at least once more to the core, if forward scattered after the first impact (Fig. 1.2). In the quantum interpretation the interferences occur between the returning wave packet and the new outgoing one [12].

1.2 High-harmonic generation

As discussed before, HHG takes place if the returning electron, instead of being scattered, is recaptured by the parent ion (iii). The energy range of the photon spectrum is determined by the instantaneous velocity the electron has at the moment of recapture. The maximum instantaneous return energy is $3.17U_p$, corresponding to an

1.2. High-harmonic generation

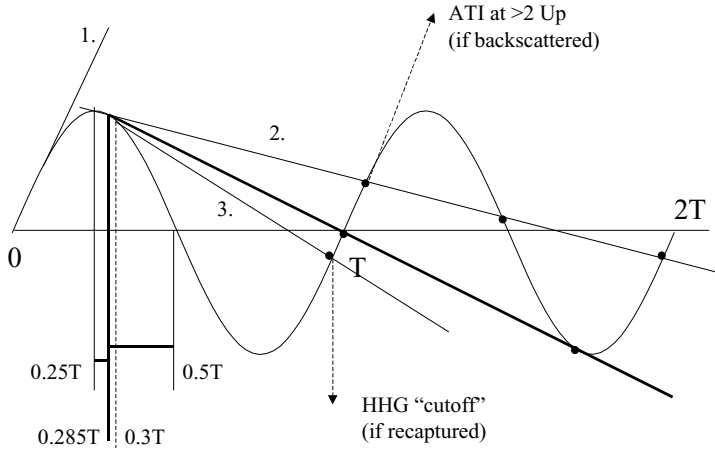


Figure 1.2: Classical electron trajectories represented as straight lines in the frame that follows the quiver motion. The electrons are ejected via tunneling, and follow the tangent to the sinusoidal function representing the nuclear displacement, in phase with the electric-field variation in time. 1. Electrons ejected at $0 \leq t_0 < \frac{1}{4}T$ never return to the core ($T = 2\pi/\omega$). They appear in the ATI spectrum at low energies. 2. Electrons ejected at $\frac{1}{4}T \leq t_0 \leq 0.285T$ return at least twice to the core. Electrons born at field maximum or immediately after return with very small velocities. Those born a bit later return with large velocities and appear at high energies in the ATI spectrum (if backscattered) or generate high-order harmonics (if recaptured). 3. Electrons ejected at $0.285T < t_0 < \frac{1}{2}T$ return only once to the core. Their destiny is similar to that of electrons following type 2 trajectories. Electrons born at $t_0 = 0.3T$ return at the nucleus with maximum kinetic energy $3.17U_p$. The return time of the first impact is $\frac{1}{2}T < t_r < \frac{5}{4}T$, depending on t_0 , but $t_r - t_0$ is shorter than T . The story is the same for each half period.

initial phase $\omega t_0 = 108^\circ$ ($t_0 = 0.3T$). This sets the "cutoff" of the harmonic spectrum, which contains photons of energies $(2l + 1)\hbar\omega$ ($l = 0, 1, 2, \dots$) up to $3.17U_p$, the maximum impact energy the colliding electron can have [47] (fig. 1). The expression for the instantaneous kinetic energy is:

$$K_{\text{return}} = 2U_p \cos^2 \omega t_0 + 2U_p (\cos^2 \omega t_r - 2 \cos \omega t_0 \cos \omega t_r). \quad (1.6)$$

Because everything repeats every half-cycle with the opposite orientation (the field is linearly polarized and the atom has spherical symmetry), the sign of the generated fields changes every half-cycle, and only odd harmonics are emitted. The magnitude of the peaks is more or less the same for the middle harmonics (region referred to as "plateau"), and decreases sharply at the "cutoff". High orders of $\simeq 297$ have been measured using very short laser pulses, of only few optical cycles [13]. The wavelengths of these harmonics go to few nm, deep into the soft X-ray domain.

Numerical calculations for the single-atom response suggest that there are two electron trajectories that give a significant contribution to the harmonic emission, both corresponding to return times shorter than one optical period T . To the "cutoff" harmonics, only one trajectory contributes. This trajectory corresponds to electrons that are ejected soon after the field reached the maximum value ($t_0 \simeq 0.3T$) and return to the nucleus $\frac{3}{4}T$ later with very high velocities (Fig. 1.2). The "plateau" harmonics and the lower ones receive the contribution of two trajectories. The parameters of trajectories depend on intensity and on the harmonic order. The longest trajectory takes almost one optical period and corresponds to electrons freed immediately after the field peaked, the shortest one takes $\simeq \frac{1}{2}T$ and is due to electrons born at $0.3T < t_0 < 0.5T$. Even if the harmonics are born with different initial phases, the calculations indicate that the total emission as a function of time has two dominant peaks per half cycle of the fundamental field, corresponding to the trajectories mentioned before [101].

After being emitted by the atom, the harmonic radiation has to propagate through the medium, out of the laser focus. This sets phase-matching conditions of geometrical nature (due to focusing) or related to the dispersion and the degree of ionization of the gas. Due to the phase-matching, the harmonics are emitted preferably along the propagation axis of the fundamental, although the angular distribution can become annular under the special condition of ionization-depleted medium [14]. The propagation through the macroscopic medium seems to favour only one of the electron trajectories described in the previous paragraph, selecting only the photons emitted through this trajectory. The peaks suffer no additional broadening in time. Which trajectory is favoured depends on the focusing conditions. The harmonic emission consists of a train of very short pulses, one per half of the period. In the frequency domain this means that the envelope peaks at odd multiples of ω . If a large number of pairs of consecutive harmonics have all the same constant phase difference (as the theory predicts), the train will contain pulses of only few tens of attoseconds [101].

1.2. High-harmonic generation

In the strong-field limit, the plateau harmonics have a similar, weaker dependence on the infrared intensity, $\sim I^p$, with the power factor p experimentally found smaller than 8. Assuming a Gaussian distribution for the infrared intensity, the far-field spatial distribution of harmonic q is proportional to:

$$I_q(r, z) \sim \exp\left(-2\frac{q^2}{p} \frac{k^2 w_0^2}{4z^2} r^2\right), \quad (1.7)$$

where $k = 2\pi/\lambda$, w_0 is the focal infrared beam waist, r is the radial coordinate in the transversal plane, z is the coordinate along the propagation axis, and $p < q$ [109]. The beam waist is the radius of the intensity profile that contains 86.5% of the beam energy, and for a Gaussian beam equals $0.85 \times \text{FWHM}$ (full width at half maximum). (In general the harmonic spatial distribution is not Gaussian. See for details [47].) The harmonic beam waist (from 1.7) and the harmonic pulse duration scale as a function of the fundamental-beam parameters as follows:

$$w^{(q)}(z) = \frac{\sqrt{p}}{q} w(z), \quad (1.8)$$

$$\tau_q = \tau / \sqrt{p}. \quad (1.9)$$

The harmonic beam is thus narrower than the fundamental, and its pulse duration is shorter. In experiments performed with short infrared pulses (7 fs, 800 nm), the duration of X-ray pulses from harmonic 55 and 57, was determined to less than 2.5 fs, which is shorter than the oscillation period of the driving field [98].

There is no direct correspondence between the ATI and the HHG spectrum. The energy of the electrons depends on the cycle-averaged drift velocity and, in the short pulse limit, gives a precise indication of the intensity at which the ionization occurred. So we can do experiments that integrate over all intensities in the focus, and still see the effects of all intensities separately. The photon energy is related to the instantaneous velocity the electron had at the moment of recapture, and it is impossible to distinguish between photons created at different intensities [64]. The only way to study the harmonic signal as a function of intensity is by exposing all the atoms in the focus to the same intensity. A more homogeneous distribution of intensities can be achieved by spatially shaping the focal intensity profile to a square pulse. It still means that there is left some averaging over the temporal distribution. We present such an experiment in **Chapter Two**. The results show evidence of a resonant atomic process. The 13th harmonic (60.5 nm) of a Ti:sapphire laser is initially suppressed at intensities where the 15th harmonic is already present, and then suddenly enhanced at 9×10^{13} W/cm², as soon as the 5g state of argon is shifted into a 13-photon resonance.

HHG proved to be a very good source of bright, coherent, short-wavelength radiation, of very short duration for experiments. More to it, if a reasonable number of harmonics are considered, pulses of tens of attoseconds can be available, although ways of selecting only one pulse from the train have still to be developed [96]. Interaction of high harmonics with a gas jet provides an easy way of doing pump-probe experiments at different wavelengths, two-photon ionization in extreme ultraviolet (XUV) [81], two-color ionization in the presence of an infrared field [15, 82, 97, 98].

If a group of consecutive harmonics is focused on a gas jet, the photoelectron spectrum contains peaks resulting from single-photon ionization with the harmonics, spaced by $2\hbar\omega$, twice the fundamental-photon energy. If a weak infrared field is added that, contrary to the harmonics, is not strong enough to ionize the atoms, certain changes will occur in the photoelectron spectrum [82]. The most obvious of those is the apparition of intermediate peaks between the harmonics, at equal distance $\hbar\omega$ from the neighbouring harmonics 1.3. These new peaks, also called "sidebands", are created through absorption or emission of infrared photons by the free electron, already ejected from the atom by the harmonic radiation in a one-photon transition. It is the same process of free-free transitions in the presence of a low-frequency field, that is involved in ATI. More than one harmonic contributes to one sideband peak. The energy range over which harmonic q is extending its influence is given by the last term appearing in equation 1.4 and equals $\pm\sqrt{8U_pK_0^{(q)}}$, in which $K_0^{(q)} = q\hbar\omega - I_p - U_p$. If the ponderomotive shift is negligible (less than 0.1 eV), which is the case for $I_{\text{IR}} \leq 10^{12}$ W/cm², the harmonics restrict their contributions only to the closest sidebands. Larger ponderomotive shifts of the ionization threshold are responsible for a second change in the spectrum: the displacement of the peaks to lower energies because of the less initial kinetic energy of the electrons. If the intensity of the infrared pulse is not constant during the presence of the harmonic pulse, the peaks will also get broader because of the variation of the ponderomotive shift with the intensity. In case of spatially-constant infrared intensity, the amount of broadening depends only on the delay between the two pulses. On these principles we based a successful method of measuring pulse durations in the XUV, with fs resolution. This method, which we call ponderomotive streaking, is presented in **Chapter Three** and was applied to measuring the duration of the 15th harmonic ($\simeq 53$ nm) pulse of a Ti:sapphire laser. We found $\tau_{15} = 10$ fs, almost 3 times shorter than the fundamental.

For measuring the temporal beating between the harmonics, that occurs on an attosecond scale, much better time resolution is required. Nevertheless, there is enough information in the photoelectron energy spectra, with and without infrared, to make possible the reconstruction of the total harmonic field. The relative amplitudes of the individual harmonic fields are given by the magnitudes of the harmonic peaks in the absence of the infrared field, and the relative phases are obtained from the energy spectrum in the presence of infrared. Under the condition of negligible U_p , two interfering paths contribute to each sideband, each path involving one of the

1.3. Double ionization

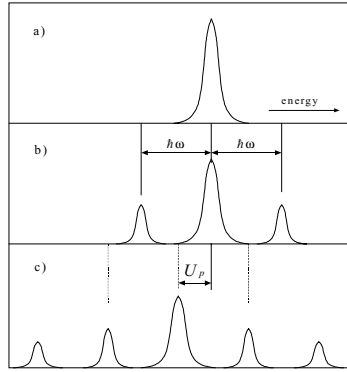


Figure 1.3: *a) The photoelectron spectrum of one harmonic. b) A weak infrared field is added and two "sideband" peaks appear to the left and right of the harmonic peak, at one infrared-photon energy distance. c) A larger infrared field is added and more "sidebands" are created. All peaks shift by U_p to lower energies.*

closest harmonics and one infrared photon, emitted or absorbed. Hence, the relative phases of the individual harmonic fields can be deduced from the sideband amplitudes, which contain information about the phase difference in their proportionality to $\cos(-2\varphi_{\text{IR}} + \varphi_q - \varphi_{q-2} + \Delta\varphi_{\text{atomic}})$. Here, φ_{IR} is the infrared field phase, φ_q , and φ_{q-2} are the phases of the harmonic fields that contribute to the sideband. The significance of $\Delta\varphi_{\text{atomic}}$ is described in **Chapter Four**. This chapter presents a method of measuring relative phases of consecutive harmonics (orders 11 to 19), concluding in the reconstruction of their total-field temporal profile. The method is similar to that used in spectral phase interferometry for direct electric field reconstruction (SPIDER) [16], but only operates on a single (harmonic) pulse and recovers the phase difference by changing the delay $\tau = \varphi_{\text{IR}}/\omega$ between the infrared pulse and the harmonic one. We may call our method reconstruction of attosecond beatings by interferences in two-photon transitions (RABBITT). It is the first experimental proof of the fact that the harmonics are emitted in very short bursts of light, of, in this case, 250-as duration.

1.3 Double ionization

If the electron scatters inelastically (*ii*) on the parent ion, it loses energy by exciting or even further ionizing the ion, or by emitting radiation due to its acceleration in the atomic potential (bremsstrahlung radiation). We shall discuss mainly the

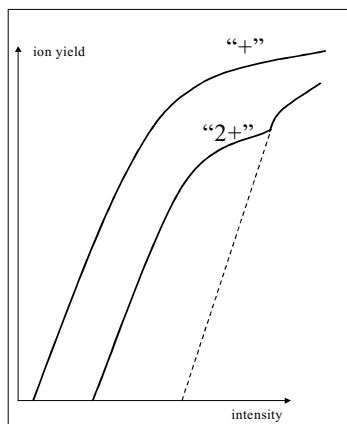


Figure 1.4: Ion signal as a function of intensity on logarithmic scales (schematically depicted). The “2+”-charge state appears at a lower intensity than predicted by the tunneling ionization theory (dashed line).

double ionization case. Multiphoton double ionization was observed first time in mid-seventies [108], and the rate measured was several orders of magnitude larger than that predicted by lowest-order perturbation theory assuming sequential non-resonant ionization, that is solving single-active-electron (SAE) problems for each electron as they leave the atom one after each other, without interacting. An experiment of L’Huillier *et al.* on xenon [17] provided evidence of non-sequential ionization in the profile of Xe^{2+} yield as a function of intensity, which presented a “knee” as if a different mechanism was initially producing doubly charged ions, and only later, after saturation of the Xe^+ signal, the sequential ionization occurred (Fig. 1.4). The “knee” saturated in parallel with the Xe^+ yield. A direct mechanism of double ionization was proposed in which both electrons are simultaneously pushed above the first ionization threshold via quasicontinuum doubly-excited states, but it was soon realized that the doubly excited electrons decay much faster to a single ionization continuum than to a double continuum, and that the ionization takes place somehow sequentially [108]. Nevertheless, subsequent interaction between the electrons has to be considered. The results on xenon were explained via a higher-order sequential process involving two-electron resonances that autoionize, followed by efficient ionization of the excited ion [18, 19].

A similar “knee” was observed in the yield of He^{2+} [20, 21], and, as in the case of xenon, the “knee” was strongly dependent on the light polarization. It is reduced even

1.3. Double ionization

for small degrees of ellipticity. Numerical calculations (SAE and tunneling) estimate the apparition intensity of He^{2+} via sequential ionization at 2×10^{15} W/cm². In the experiment, He^{2+} was detected already at ten times lower intensities. Because the ionization of helium is non-perturbative (tunneling), the resonant mechanism proposed for xenon cannot be applied here. Numerically solving the time-dependent Schrödinger equation (TDSE) for an atom with 2 electrons, one of them oscillating at large distance from the nucleus, was beyond the power of any computer of that time, and semiclassical explanations were proposed initially.

The shake-off model of Fittinghoff *et al.* [20] assumes that the potential seen by the inner electron changes so rapidly because of the outgoing electron, that the probability of two-electron ejection is much increased. The first electron leaves the atom so rapid that the second electron is left in an excited state, which is immediately ionized by the laser. The results fit the experimental curve, but the model cannot explain the polarization dependence of the non-sequential yield.

The explanation suggested by Corkum, based on the two-step model described above, implies an (e,2e) scattering process when the free electron returns to the parent ion [52]. This recollision model is supported by the results of Muller obtained from numerically solving the TDSE for a 2-electron He atom, on an L-shaped grid (fewer grid points are necessary for the radial coordinate of the inner electron that moves very close to the nucleus). Whatever escapes at the end of the grid arms is product of single ionization, and only what leaves via the inner edge of the grid is the result of double ionization. Calculations done for 390-nm linearly-polarized light of intensity 1.1×10^{15} W/cm² (at which values the He^{2+} yield from sequential ionization is negligible), show that the electron emission, integrated on the inner edge of the grid close to the corner, as a function of time peaks immediately after the maximum of the field, with no peaks for the first optical cycle [22]. The results can be interpreted in a semiclassical manner. One electron is ionized via tunneling ionization and then driven back to the core by the field, where it finds the bound electron. Only a free electron created at the maximum of the field returns to the core one period later, with very small velocity. It does not have enough kinetic energy to impact ionize the other electron, but it comes so close to this one that builds up enough repulsive potential that added to the potential of the laser *pushes out* the inner electron as well. The peaks in the electron emission have a kind of shoulder at earlier times, that covers almost a quarter of a period. These electrons are the result of impact ionization. If the outer electron is born slightly after the maximum of the field, it has a large kinetic energy at the moment of return and simply *knocks out* the inner electron.

If the wavelength is 780 nm, the ponderomotive energy is larger, at the same intensity, and the contribution from impact ionization increases. The shoulder transforms into a peak of the same size with the peak produced by the *push-out* mechanism. The calculations at this wavelength revealed a third possible mechanism for non-sequential double ionization [23]. For these calculations the grid arms had to be longer because the outer-electron oscillation had a larger amplitude. The maximum quiver amplitude

is given by:

$$\alpha_0 = \frac{eE_0}{m_e\omega^2}. \quad (1.10)$$

Thus it is 4 times larger for 780 nm than for 390 nm. If the electron emission is integrated on the inner edge of the grid close to the end of the arm, it is equivalent to detecting double-ionization products under the condition that one of the electrons is distant from the core. The two previous mechanism will give insignificant contributions because both of them require the presence of the two electrons close to the nucleus. Nevertheless, the electron production shows some small peaks, at time moments corresponding to a field of maximum amplitude. What happens is that some outer electron born at the field maximum might not approach the nucleus close enough to *push out* the inner electron, but it might well *knock up* the inner electron to an excited state. Very soon after, the field will be maximum and will ionize the excited electron. Meanwhile, the outer electron travels some distance away from the nucleus.

For an atomic gas, the ion yield from non-sequential ionization is quite low. For clusters, forms of matter containing atoms (or molecules) linked together by Van-der-Waals bonds, multiply charged states appear in large amounts in the ion spectrum at intensities three orders of magnitude lower than necessary for sequential ionization [123]. Due to the high local density, the electron-ion collision rate increases very much and the electrons get very high kinetic energies. At around 10^{15} W/cm² direct optical field ionization (OFI), via tunneling, creates at most doubly-charged states, but the free electrons are heated, via backscattering at multiple collisions with the ions, to hundreds of eV [117]. The very hot electrons leave the cluster, but many others are trapped inside and produce higher-charge ionic states by impact ionization. The field of the neighbouring ions can also contribute to an increase in the tunneling ionization rate. The pressure of the hot electrons and the repulsion between ions make the cluster expand very fast. Ions of around 1 MeV energy were detected in some experiments [110, 114].

We studied the production of highly charged ions from laser-irradiated clusters of carbon-containing molecules (propane and carbon dioxide). A Ti:sapphire laser (800 nm, 170 fs) was used as driving laser. The results are presented in **Chapter Five**. At 4×10^{14} W/cm² O⁶⁺ and C⁴⁺ ions were detected from explosion of carbon-dioxide clusters, and C⁵⁺ from the larger propane clusters. Some of them had energies of more than 1 keV, indicating average electron temperatures of 300 eV. This experiment was meant as a preliminary study of the possibility to develop an X-ray laser by creating population inversion in highly charged excited ions, that decay to the ground state via direct short-wavelength transitions. We shall discuss X-ray lasers in section 1.5, after a short review of one more non-perturbative effect in the atom-laser interaction.

1.4 Stabilization

In all cases discussed before, an increase of intensity was also resulting in an increase of ionization. Ionization saturated only by depletion of the atomic medium or in the special case of population trapping in highly excited states. The last situation is referred to as dynamic stabilization [24], and can occur at intensities below 10^{15} W/cm². It is in general explained by quantum destructive interferences between contributions from closely-spaced ionizing bound states. Various mechanisms were proposed: destructive interferences between bound states of the same parity as the initial state, populated by stimulated Raman transitions through the continuum [25]; delocalized Rydberg wavepackets also produced by a Raman coupling mechanism between the continuum and Rydberg states that cancel each other's contributions [26]; creation of spatially extended wavepackets via indirect population, that are hard to ionize because they are localized far from the nucleus where further absorption of photons is inhibited [27]. The results of some experiments performed by Jones *et al.* [28] and Hoogenraad *et al.* [29] were explained in terms of this last mechanism.

The "pearl" of stabilization is called adiabatic stabilization and it manifests itself in the decrease of the ionization rate as the intensity increases ($\Gamma \sim \omega^4/I^{3/2}$). It requires super intense fields ($> 10^{17}$ W/cm²) and high frequencies, and begins as soon as the quiver amplitude of the electron motion is larger than the atomic size. Pont and Gavrilă have given the following conditions for stabilization: the photon energy shall be larger than the absolute binding energy of any involved atomic state, and the field large enough to drive the electron in a wide motion ($\alpha_0^2\omega \gg 1$, when expressed in atomic units) [30]. The electron is oscillating very fast, and tends to localize at distance α_0 from the nucleus, in a region where the probability for photon absorption is very low. The lifetime of the state plotted as a function of intensity shows an initial decrease up to a critical point where $\alpha_0\omega^2 \simeq 1$, and then a strong increase as the intensity increases further. Because the atom can easily ionize before the peak of the field, the pulse duration shall be carefully chosen to help the neutral atom survive till the high intensities are reached. For all these, it is very hard to stabilize the ground state of an atom and no experiment has been reported yet. The problem is the absence of strong sources of soft X-ray radiation, of short duration. (More than 10^{16} W/cm² are necessary at 160 nm, and a pulse duration of 15 fs for stabilizing a quasihydrogenic atom with $I_p = 18$ eV [31].) The high harmonics so far have too low intensities. Things are different for excited states. States with high magnetic quantum numbers can be stabilized at 1064 nm with only 10^{14} W/cm², according to a calculation by Vos and Gavrilă [32]. Experimental adiabatic stabilization of excited states was reported by de Boer *et al.* [33] and van Druten *et al.* [34] for the circular 5g state of neon. The laser pulse characteristics were: 620 nm, 90 fs, around 10^{14} W/cm² intensity. At the moment, these are the only experiments to report adiabatic stabilization.

1.5 X-ray lasers

This section will treat a somehow different problem: the development of laser sources of soft X-ray radiation that can be easily available in the laboratory. The soft X-ray domain extends between 0.2 and 30 nm wavelength (41.3 to 6200 eV, in terms of energy). It is preceded towards longer wavelengths by the XUV domain (30 – 100 nm) and vacuum-UV domain (100 – 200 nm), in which range of frequencies HHG is already a very good source of radiation for experiments.

The (soft) X-ray lasers can be classified, depending on the pumping method, in three categories: lasers pumped by collisional excitation of plasma ions, lasers pumped by inner-shell ionization of atoms or ions and recombination-pumped lasers [35].

The first X-ray laser was demonstrated at 21 nm by Matthews *et al.* in mid-eighties [36]. The population inversion was created between $2p^53p$ and $2p^53s$ levels of Se^{24+} , a neon-like ion, by electron-collisional excitation from the ground state $2p^6$, which is also the final state in the lasing scheme. This has the advantage of self-contained population replenishment. The plasma was formed by irradiation of a thin selenium foil with green light (532 nm) of 5×10^{13} W/cm² intensity in a linear, 1-cm-long focus. The green laser ionized the selenium atoms sequentially to 24+. The enhancement of a spectral line is equal to $\exp(GL)$ if a seed beam is amplified and to $\frac{\exp(GL)-1}{GL}$ in the case of amplified spontaneous emission (ASE). G is the gain coefficient and L is the length of the amplification medium [35]. In this experiment the gain coefficient was 5.5 ± 1.0 cm⁻¹.

In other experiments using the same pumping method, the radiation wavelengths was even shorter. A gain coefficient of 2.3 cm⁻¹ was measured for Ta^{45+} (Ni-like ion) at 4.5 nm ($4d - 4p$ transition), and of 2.6 cm⁻¹ for W^{46+} (also Ni-like) at 4.3 nm, within the "water-window" [37]. The "water-window" is the wavelength region between the K absorption edge of oxygen and the K absorption edge of carbon: 2.3 – 4.4 nm. Because of the low absorbance of oxygen, this region is important for X-ray microscopy of biological samples.

The trouble with this type of lasers, pumped by electron-collisional excitation and working on $\Delta n = 0$ transitions, comes from the process of plasma production. Kilojoules of laser energy are necessary for the creation of hot free electrons and the solid-density target is damaged and has to be renewed after each shot. Besides, more than one line is usually amplified. Nevertheless these lasers are quite wide-spread, especially in the XUV [35]. The first demonstration of an (XUV) laser based on a gaseous target and using a table-top laser to create the plasma ions was reported by Lemoff *et al.* [38]. They observed lasing at 41.8 nm in Xe^{8+} (the $4d^95d^1S_0 - 4d^95p^1P_1$ line) with an estimated G of 13 cm⁻¹.

The method of ionization pumping is based on the creation of an inner-shell hole (by collision with an electron or an ion, or by photoionization), which can lead to population inversion with respect to an outer-shell electron. The lasing transition is of $\Delta n = 0$ or $\Delta n = 1$ type. For a Na-like ion ($1s^22s^22p^63s$) the ionization cross-

1.5. X-ray lasers

section is 100 times larger for the $2p$ electron than for the $3s$ electron, provided the photon energy is high enough. The lasing transition would be $3s - 2p$ at 37.2 nm. A K-shell vacancy can also be created in Li-like ions or in Ne atoms, but photons of very high energy are necessary. In general for this method, the laser radiation is of longer wavelength than the ionizing radiation, which on the other hand does not have to be coherent. The experimental attempts to produce lasers based on Na-like ions or on the neutral-Ne scheme were unsuccessful.

The first successful report of a photoionization-pumped laser was based on Auger-decay pumping, a scheme in which the population inversion is produced by the branching of the Auger-decay process [39]. The high-energy photons necessary for inner-shell ionization are obtained from a radiative plasma of tantalum. A $4d$ electron is ejected from neutral Xe, and the Xe^+ ion undergoes Auger decay, a non-radiative process in which the vacancy is filled by a higher-level electron. The energy is released by ejection of another outer-shell electron. The population inversion occurs between the levels $5s^05p^6\ ^1S_0$ and $5s^15p^5\ ^1P_1$ in Xe^{2+} (108.9 nm). A maximum gain coefficient of 0.8 cm^{-1} was reported.

The third type of X-ray lasers is based on electron recapture into excited ionic states. The high-charge ions are created collisionally or by photoionization and they can recapture a free electron (three-body recombination) or an electron from a neutral atom (charge transfer) in a highly excited state. To obtain population inversion, the recombination process has to occur on a time scale shorter than the natural lifetime of the lasing transition. Thus, the free-electron temperature has to be low. This is the case if plasma production is more rapid than the recombination. Usually, the recombination process is too slow to produce population inversion with respect to the ground state, and the lasing transition occurs between two high levels. Radiation of very short wavelength can be obtained from H-like and He-like ions.

The first experiment on recombination pumping reported a gain of 6.5 per pass for the 18.2 nm transition ($3 \rightarrow 2$) in C^{5+} [40]. The plasma was created by a CO_2 laser (1 kJ) in a solid carbon target and confined in a strong solenoidal magnetic field. The plasma was cooled by radiation losses, which proved to be a more efficient way of cooling than adiabatic cooling of an expanding plasma. Since then, many experiments have been reported on solid targets or microcapillaries [35].

Optical-field-induced (OFI) ionization (rather than collisional ionization) has been suggested for the production of highly charged ions, by means of high-intensity tabletop lasers as drivers [41, 42]. Because of the very short duration of the laser pulse, the intensity is high enough at only 100 mJ for ion production by tunneling ionization. OFI in the gas phase produces much cooler plasmas than in solid targets, and, as a consequence, the recombination is faster.

In the first experiment to observe ASE in a scheme based on OFI ionization [43], a gain coefficient of 20 cm^{-1} was measured for the 13.5 nm transition in H-like lithium ($4 \rightarrow 2$). In the first step, a long-pulse laser was focused on solid Li to create a singly ionized Li plasma of 1.5 eV electron temperature, and afterwards a high-intensity

KrF laser (50 mJ, 500 fs), focused slightly above the surface, in the vapors created by the first pulse, was used to produce fully stripped Li^{3+} ions. Some experiments revealed that the cold electrons involved in the recombination process are produced by the second, very intense pulse [44].

The solid target is completely destroyed by the intense laser. Using clusters as targets brings important improvements in this respect. The local density of the cluster is comparable to a solid target, and the target is renewed very simply in the jet flow. Collisional ionization in the expanding cluster helps the production of highly charged ions, and much lower laser intensities are sufficient [123]. This is very helpful because a larger focal volume can be created, thus a larger gain-length product.

Our attempt of developing an X-ray laser was based on recombination pumping, and was focused on the wavelength region known as the "water window". The project prescribed irradiation of carbon clusters as source for the creation of C^{6+} , with the advantages mentioned right above. A better solution for a fast recombination was to use a buffer gas (of helium) which remained neutral in the laser field, thus fulfilling the conditions of high electron density and low electron temperature. Recombination via charge transfer is faster than via three-body collisions. The third innovation in the initial project was the fast excitation of the $3d$ state in C^{5+} (populated by charge transfer) to $4p$ with five infrared photons exactly tuned to the frequency of the transition, followed by the lasing transition to the ground state $1s$ (at 2.7 nm). For a gain coefficient of 2.5 cm^{-1} , a gain length of 10 cm would amplify a single X-ray photon to the μJ range.

Chapter Six is devoted to our study of the development of a table-top X-ray laser. The first step, the production of highly charged carbon ions, is discussed in **Chapter Five**, as we mentioned above. **Chapter Six** describes the second step, the analysis of the radiation emitted by the carbon ions and of the process of resonant charge transfer from the neutral helium we used as buffer gas. We detected radiation of less than 15 nm (more than 83 eV) from transitions in O^{5+} ($4p-2s$ at 11.6 nm, $4s, d-2p$ at $\simeq 13$ nm), and C^{4+} ($4p-1s$, $3p-1s$ and $2p-1s$ at less than 4 nm). Unfortunately, we could not produce a significant amount of C^{6+} in the cluster explosion, and our study had to stop here.

The remainder of this thesis is structured in two parts. The first part contains three chapters about characterization of soft-X-ray sources, focused on HHG. It includes the measurement of the (15th) harmonic-pulse duration and, the most important fact, the reconstruction of the temporal profile of the harmonic emission. The second part contains two chapters devoted to the study of table-top sources of X-ray laser radiation.

Part I

High-Harmonic Generation

Chapter 2

Resonance-enhanced HHG

In this chapter we present some results of a high-harmonic generation experiment in argon, performed with a Ti:sapphire laser (787 nm, 140 fs) and a spatially shaped focus (flat top). The range of intensities is 3 – 100 TW/cm². The intensity dependence of the harmonic signal shows an interesting behavior of the 13th harmonic, namely an initial suppression followed by a strong enhancement at $\simeq 85$ TW/cm², exceeding in magnitude the 11th harmonic. This behavior is a consequence of a resonant atomic process. Numerical calculations were also performed. They partly reproduced the experiment.

2.1 Introduction

The fascinating subject of high-harmonic generation (HHG) from a laser beam focused in a gas jet stimulated the publication of a large number of papers over the last ten years. Experimental results obtained at the end of 80's (see [45,46], for example) at high laser intensities led to the development of theoretical non-perturbative methods of study (numerical integration of time-dependent Schrödinger equation, methods based on Floquet theory or approximate models, path-integral calculations) [47] and various models describing both the single-atom response and the propagation effects were proposed [47]. Driven by the experimental data obtained since 1992, which addressed questions regarding the cutoff of the harmonic spectrum, the spatial distributions and the intensity profiles of the harmonics, the propagation and phase-matching effects gained increasing attention in the theoretical papers devoted to the subject [48–51]. The semiclassical two-step model developed by Corkum [52] and Kulander [53] gave a fairly accurate description of the atomic behavior and has been successfully extended to include some quantum effects, by Lewenstein, Becker and their co-workers [54–56].

2.1. Introduction

A number of experiments were dedicated to the study of the harmonic signal as a function of intensity and the role of atomic resonances in harmonic generation was a main subject of discussion in the early days of HHG. We refer especially to the papers of L'Huillier and Balcou [57,58] who attribute the structures from the harmonic-yield vs intensity graphs to resonance effects and also to previous papers of Crane *et al.* [59] and Miyazaki and Sakai [60] who consider the resonances responsible for plateau formation. The relation between above threshold ionization (ATI) and HHG has also received attention, and although initially one expected similarities between the two spectra (see [61], a paper which theoretically predicts the existence of a plateau due to couplings in the continuum, and [62,63]), the experiments did not confirm these predictions ([64] and the references therein). It has been accepted that there is no direct correspondence between the electron and photon spectrum, the energy of the photoelectrons depending on the cycle-averaged (drift) velocity they gain from the field or by successive collisions with the core, while the energy of the emitted photons is related to the instantaneous velocity the electron had at the moment of recapture [65].

The problem of resonant effects in both type of spectra is still open. It was not difficult to explain the features present in the low-order ATI peaks within the limits of the standard ATI model, but the enhancement and the intensity-selective substructures observed in the high-energy part of the spectrum (more than two times the ponderomotive shift) so far can only be explained by fully solving the time-dependent Schrödinger equation [66,67]. The fact that the production of high-energy electrons is enhanced at specific intensities suggests the existence of a resonant process which increases the number of collision events by generating more free electrons or by directing them more efficiently to the nucleus. Since the HHG process is the result of similar impacts on the core, followed by recapture, it is likely that an increased number of electron-ion collisions due to resonant ionisation will also affect the harmonic spectrum.

The main goal of the experiment presented in this paper is the study of the harmonic signal as a function of intensity. As L'Huillier *et al.* [58] have also emphasized, the main problem in such an attempt is the presence of many intensities in the focus which makes it very difficult to extract data about the behavior of the elementary processes from the harmonic yield. Unlike photoelectrons which by their energies give a precise indication of the intensity at which the ionisation occurred, photons created at different intensities are indistinguishable. Even worse, such photons interfere, making it impossible to use deconvolution techniques to recover the atomic response from the harmonic yield. Consequently, it seems worth-while to perform an experiment that exposes all atoms to the same intensity. This can be achieved with a spatially shaped focus that has a flat-top intensity profile. This will provide a more homogeneous distribution of intensities in the gas jet and a more direct way of studying the harmonic emission as a function of intensity.

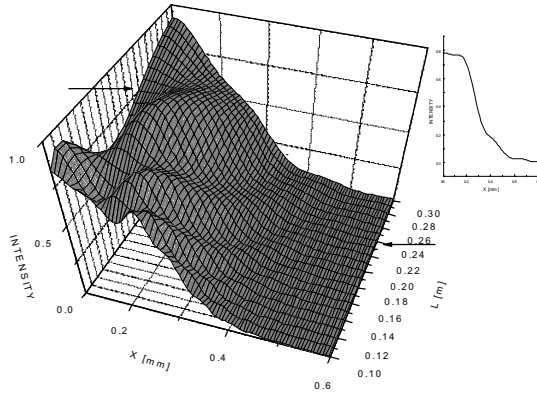


Figure 2.1: *The intensity profile of a gaussian beam after diffraction on a circular aperture with a diameter of 2 mm (numerical calculations). The picture is symmetric with respect to the left coordinate plane. L is the distance from the aperture. The beam-intensity FWHM at the aperture is 0.92 mm. In the upper corner it is depicted the spatial profile at $L=0.77$ m, the position of the flat-top.*

2.2 Experimental setup

A Ti:sapphire laser system has been used for this experiment. It can deliver 4 mJ pulses at a repetition rate of 10 Hz. The pulse duration is 140 fs and the central wavelength has been set at 787 nm.

Placing an aperture in a Gaussian beam the spatial profile of the beam changes immediately after the aperture due to diffraction. This can produce both dark and light spots in the centre. At a certain position behind the aperture the spatial intensity distribution becomes approximately flat. In Fig. 2.1 we present the variation of the intensity profile along the propagation axis of an initially Gaussian and parallel beam after a circular aperture as it results from numerical calculations done in the near-field region using the Huygens-Fresnel principle. The position of the flat top is dependent on the beam and aperture diameters. In our experiment a circular aperture ($\simeq 2$ mm in diameter) was placed in the beam between the amplifier and the compressor for the shaping of the beam. The dimension of the aperture being much larger than the full width at half maximum (FWHM) of the beam only a small amount of energy was lost. The flat top occurred in the beam profile at a distance of $\simeq 70$ cm behind the aperture.

We imaged this profile in the focus of the beam, at the cross-point with the argon jet, using a telescope with a demagnification factor of 12. The telescope was composed

2.2. Experimental setup

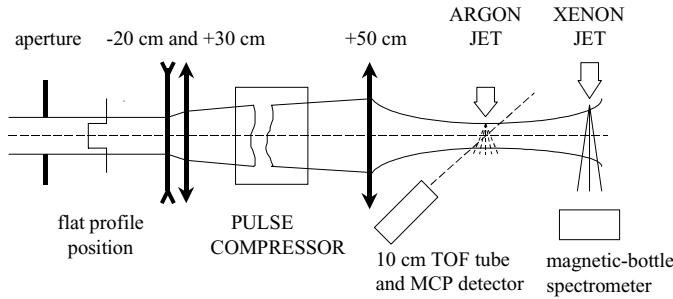


Figure 2.2: A schematic of the experimental setup.

of a lens pair (-200 mm and $+300$ mm) with an effective focal length of 6 m and a 0.5 m positive lens (see Fig. 2.2). The length of the entire setup of the telescope is almost 14 m. The advantage of using a telescope instead of a single lens is that the image can be formed in the focus, i.e., at the place where the beam is most narrow. A single lens, on the other hand, would form the image behind the focus in a zone where the beam is divergent leading to a large inhomogeneity of intensity in the propagation direction of the light. The shaped profile is placed in the object focus of the lens pair and is imaged in the focus of the $+0.5$ m lens. The diameter of the beam (FWHM) at the aperture is 0.9 mm and in the focus almost 75 μm . The diameter of the flat part is $\simeq 50$ μm . The quality of the imaging is restricted by the dimensions of the optics and by the aberrations of the lenses. The spherical aberrations can be reduced by a proper choice of the focal distances of the lens pair, the astigmatism can be corrected by tilting the lenses. The resolution of the imaging system was optimized this way while imaging a very small pinhole 100 μm in diameter. The focus could be viewed by inserting a reflective plate in the beam (after reducing the energy by neutral density filters) and it was imaged by an achromatic doublet onto a CCD camera, magnifying it six times. Due to the fact that the beam diameter on the compressor gratings is around 2.5 mm (FWHM) the beam energy had to stay below 2 mJ in order to protect the gratings. The maximum intensity which can be reached in these conditions in the focus is $\simeq 100$ TW/cm^2 , considering the losses on the aperture and in the compressor. The intensity resolution that theoretically can be achieved with this method is 11% .

After interaction with the Ar in the primary gas jet, the light including the harmonics was sent to a Xe gas jet. Electrons generated in the process of ionization of Xe were detected in a magnetic-bottle spectrometer using a microchannel plate (MCP). We binned the spectra based on pulse energy measured on a photodiode. For the calibration of the focal intensity, a 10 cm time-of-flight tube and another MCP have been installed near the interaction point of the light with the Ar jet in order to detect the photoelectrons produced by ionization of Ar there.

2.3 Results and discussion

The ionisation potential of Xe is 12.127 eV so the Xe atom can be ionised by at least 8 photons at the wavelength of 787 nm. Consequently, odd harmonics starting from the 9th can be detected, and at the intensities we can afford the highest harmonic generated is the 21st. The use of a Soleil compensator and a polarizer placed between the amplifier and the aperture makes the variation of the intensity in the focus possible. For the calibration of the photodiode signal with the intensity some photoelectron spectra of the Ar were measured simultaneously with the harmonic ones (Fig. 2.3). The peak at 40 ns corresponds to the high energy electrons of the first plateau of the ATI spectrum of Ar (15 – 30 eV). This peak did not disappear when a retarding voltage of 15 V was put on a grid placed in front of the detector. It is known [66] that electrons in this energy region start being enhanced at an intensity of 67 TW/cm². In the marked intensity trace the ratio between the narrow peak and the low-energy electron peak starts changing and we assigned to this trace the intensity corresponding to the initiation of the enhancement.

Fig. 2.4 shows the harmonic spectrum of Ar at different laser intensities, obtained with a flat-top intensity profile of the beam at the focus. Each plot is averaged over 1000 shots for the lower bins and around 100 for the highest. Each harmonic results in two peaks due to the spin-orbit interaction in Xe. The most interesting harmonic in the spectra is the 13th. This harmonic is absent for intensities lower than 70 TW/cm², then increases very quickly, even exceeding the 11th harmonic at 82 TW/cm² and it stays dominant for the rest of the intensity range of the measurements. In Fig. 2.5a we present the integrated area of each peak as a function of intensity. Three features catch the eye in this picture: the absence of the 13th harmonic for a range of intensities where the 15th is already present, the sudden and abrupt increase of the same harmonic and the shoulder in the graph of the 11th. Next to it in Fig. 2.5b similar areas extracted from the harmonic spectrum obtained with a Gaussian focus are plotted. Although also there the 13th harmonic appears in the spectrum later than the 15th, it doesn't grow higher than the 11th. The comparison between the two spectra clearly demonstrates the possibility provided by the flat-top distribution to study intensity dependence. In the present case, it reveals additional features which otherwise are smeared out by the Gaussian profile.

2.3. Results and discussion

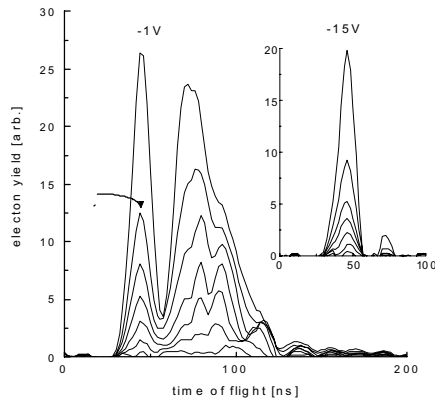


Figure 2.3: *Electron spectra of argon for different intensities (from 42 to 72 TW/cm² in steps of 5 TW/cm²) and two different retarding potentials (-1 V and -15 V). The narrow peak is corresponding to the high-energy electrons (above 15 eV).*

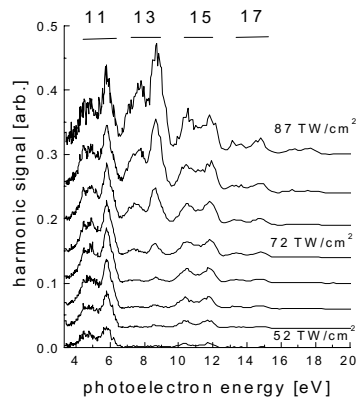


Figure 2.4: *Electron spectra from xenon ionised by harmonics generated in argon, at different intensities, from 52 to 87 TW/cm² in equal steps. The spectra are arbitrarily offset vertically for a better comparison. The numbers above give the harmonic responsible for the various peaks.*

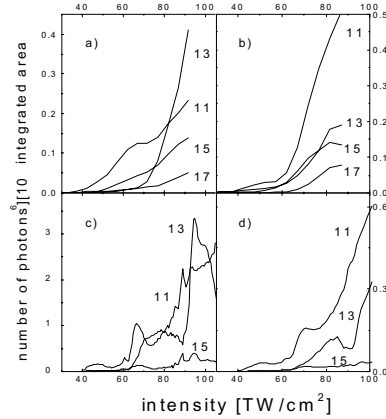


Figure 2.5: *Integrated areas of the harmonics as a function of intensity for a spatially shaped focus (flat top) (a) and for a gaussian focus (b) obtained from the experimental data and also the numerical results for a shaped (c) and a gaussian focus (d). The dashed lines represent the 13th harmonic.*

Numerical calculations were performed in an attempt to explain this behavior. Two steps were considered in such a simulation: the single-atom response and the propagation through the medium. The dipole moment was calculated using the numerical integration of the time-dependent Schrödinger equation, method described in [68]. The square modulus of its three Fourier components of interest were plotted in Fig. 2.6. The 13th component has a strong resonance at around 93 TW/cm².

The study of the macroscopic response starts from Maxwell's propagation equations which one can solve using the slowly varying envelope and the paraxial approximation [69]. The dispersion effects due to linear polarizability of atoms can be reasonably neglected because of the low density regime and small interaction length we consider. The fundamental beam can still be modified by the free electrons resulting from the partial ionisation of the medium. It leads to defocusing and blueshifting of the fundamental, but these effects can also be neglected [69, 70] in the regime of intensity and low density we performed the experiment. We therefore assume that the fundamental field will not be modified while propagating through the medium. We have considered two different shapes in space. The first one is the flat top and comes from the superposition of two Gaussian beams with different confocal parameters but focused at the same position $z = 0$. The amplitudes of these beams have been chosen such that they partly cancel each other in the $z = 0$ plane. This superposition gives an intensity profile very similar to the observed one, and also predicts the phase dependence (which was not directly observable in the experiment). The second beam

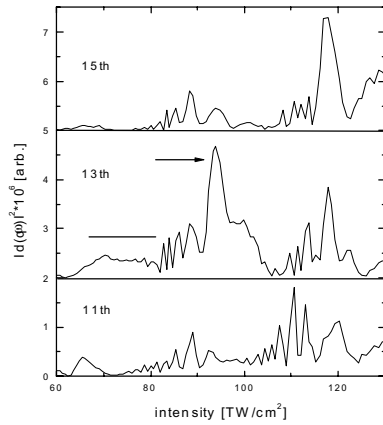


Figure 2.6: *The 11th, 13th and 15th harmonic component of the dipole moment plotted with an arbitrary offset. The arrow indicates the strong resonance present in the 13th harmonic at 93 TW/cm² and the horizontal line marks the pedestal.*

shape we considered was a Gaussian with approximately the same confocal parameter as the resulting previous flat-top pulse. The propagation equation concerning the harmonic field is then solved using a finite-difference technique and this allows us to get the harmonic field $\vec{E}_q(\rho, z, t)$ for the cylindrical coordinate z sufficiently far behind the focus, and therefore the number of photons for each harmonic, which is proportional to: $\int_0^\infty d\rho \rho \left| \vec{E}_q(\rho, z, t) \right|^2$.

We perform the calculations for a range of intensity between 40 and 110 TW/cm². The results are plotted in Fig. 2.5c and d. The simulation reproduces quite well the steep increase of the 13th harmonic but not the initial absence of this harmonic. In the calculation, there is a pedestal before the 13th enhancement. It is already present in the atomic response and survives the propagation. The nature of this pedestal is still not understood. The 13th harmonic peaks to a high value at 93 TW/cm² and then decreases, something not seen in the experimental picture due to the intensity limitation. From the total ionisation rate as a function of intensity [71] we can associate this resonance with a 13-photon transition to the 5g state of Ar. The shoulder of the 11th harmonic can be a consequence of the broad peak at 67 TW/cm². In general the calculations reveal more detail, but most of these structures are not resolved in the experiment. Everything in the theoretical graph seems to happen at slightly higher intensities than in the experimental one. The experimental intensities calculated directly from the pulse energy and the focal parameters are 10% higher

than the ones obtained using the ATI spectra of Ar for calibration. We did not use the direct way of calculation because it is notorious for overestimating the values of the intensity, although for our comparatively large and well-defined focus it can be expected to perform better.

As for the Gaussian plots, there is still some competition between the 13th and 15th harmonic present in the experimental graph (Fig. 2.5b) and there are also some structures in the numerical one (Fig. 2.5d) but the fast varying intensity in the Gaussian focus smooths out most of the peaks of the dipole moment (Fig. 2.6).

2.4 Conclusions

To the best of our knowledge this is the first experiment of high-harmonic generation performed with a spatially shaped focus. The imaging technique described proved to be successful in increasing intensity resolution and it can be a viable solution for other experiments which require a homogeneous distribution of intensities at the focus. The harmonic spectrum measured in these conditions shows distinct features not present in the spectrum obtained with a Gaussian focus. The most peculiar feature is likely to be the signature of a resonant process of enhancement. Unfortunately, due to our detection system, we are not able to give absolute values for how efficient this process is in terms of number of photons. The theoretical results do not fit exactly the experimental ones in the matter of the suppression of the 13th harmonic, but they do reproduce the enhancement of the same harmonic. The flat-top profile provides an improved intensity distribution with respect to the Gaussian beam but the phase distribution is an open issue in view of comparison with theory.

Chapter 3

Ponderomotive streaking

In this chapter we present an alternative method for measuring ultrashort extreme-ultraviolet pulses that can be synchronized with an intense infrared pulse. The method, based on photoionization of a target atom by the extreme-ultraviolet pulse in the presence of the infrared pulse, has a potential accuracy of close to 1 fs and is susceptible to single-shot operation. It is demonstrated on harmonic 15 of a titanium:sapphire laser. The minimum pulse duration that can be measured is limited only by the frequency of the radiation used for the ponderomotive shift of the ionization potential (3 fs in the case of the Ti:sapphire fundamental).

3.1 Introduction

The progress made in the last years in obtaining ultrashort light pulses at frequencies in the extreme ultraviolet (XUV) demands the development of new methods for studying their characteristics and in particular their duration. Current infrared lasers can produce pre-amplified pulses of only 8 fs and pulses of 16 fs after amplification [72–75]. Further compression by means of hollow-fiber chirped-mirror compressors can bring the duration to 5 fs [76, 77]. Since such pulses contain only a few cycles, they are close to the theoretical limit. With radiation generated from such lasers by frequency conversion to shorter wavelengths, the period of the optical cycle is shorter so that the theoretical limit is pushed to the subfemtosecond range.

High-harmonic generation, one of the most utilized in applications among such XUV secondary sources, produces extremely short pulses. According to theory, both in the perturbative and in the non-perturbative regimes, the duration of the harmonic pulses is shorter than the duration of the fundamental [48, 49]. For temporal characterization of such pulses few methods are available. The first one is autocorrelation, although this does not give complete information about the temporal shape of the

3.2. Description of the method

pulse. Here one records the result of a non-linear process, in which two copies of the pulse contribute simultaneously, as a function of the delay between these pulses. Examples of such processes are second-harmonic generation in a non-linear crystal, two-photon ionization or index variation in a Kerr medium [78]. Mathematically, the measured quantity is the convolution of the pulse with itself, and there are no fundamental limitations regarding the duration of the pulse to be measured. A serious drawback is that the efficiency of non-linear processes depends on the pulse intensity, and if the intensity is too low the method is inapplicable. The (generalized) cross section [79] for two-photon ionization decreases rapidly with wavelength, and for argon at 53 nm it is only $2.1 \times 10^{-52} \text{ W}^{-2}\text{cm}^6$ (results obtained from numerically solving the time-dependent Schrödinger equation [68]). To measure a statistically significant autocorrelate in a reasonable time (say 10^5 shots), then requires 2 nJ of focused harmonic radiation, about an order of magnitude more than usually can be obtained. Only for very low harmonics, where the two-photon cross section is three orders of magnitude larger [68], is autocorrelation feasible in the face of losses associated with purification of a single harmonic [80, 81]. Single-shot measurements require a million times higher signal level, (i.e. a thousandfold increase in pulse energy), and are completely infeasible for the moment.

To circumvent these problems, cross-correlation techniques were developed as an alternative. By replacing one of the XUV beams by a "probe" beam of longer wavelength (visible or infrared), where virtually unlimited intensities are available, it is the single-photon XUV process that becomes the limiting factor. Again for argon at 53 nm this is $8 \times 10^{-20} \text{ cm}^2$, and 5 fJ of XUV energy per pulse would already provide a detectable signal, while single-shot capability occurs at 5 nJ. The duration of the XUV pulse can be extracted from the cross correlate by deconvolution [82, 83]. The disadvantages come from the fact that the probe pulses that are available tend to be longer than the XUV pulse and this imposes a serious limitation on the temporal durations that can be measured. If the probe pulse contributes in a higher order to the process its effective duration shrinks accordingly and shorter pulses can be measured [84, 85]. Cross-correlation techniques can also be used by means of Auger decay processes [86], changes in the bound-free absorption of the XUV radiation [87, 88], ionization-induced defocusing [89].

3.2 Description of the method

We present a different method for measuring pulse durations in the XUV domain. It preserves the high sensitivity of cross-correlation methods, but it can beat the limit due to the duration of the dressing pulse by nearly two orders of magnitude. The method is based on the change of individual peaks of the photoelectron energy spectrum resulting from ionization with the high-frequency pulse due to the ponderomotive shift of the atomic ionization potential induced by an intense "dressing" pulse

of longer wavelength. In this respect it is similar to one of the schemes proposed by Constant *et al.* that measures the shift in the envelope of the photoelectron spectrum due to the presence of circularly polarized 10- μm radiation [90]. We demonstrate our method by measuring the duration of high harmonics generated by an infrared laser beam in an Ar gas jet. These harmonics are sent on a second Ar jet to ionize atoms that are exposed at the same time to part of the fundamental beam. This infrared shifts the ionization threshold of the Ar atoms, but is not intense enough to ionize the atoms by multiphoton processes. The XUV photons are energetic enough to ionize the atoms in a one-photon process.

It is well established [91] that the ionization potential increases ponderomotively when the atoms interact with a strong electric field. This ponderomotive shift equals the time-averaged kinetic energy of an electron oscillating in a laser field and depends on intensity I as: $U_p[\text{eV}] = \alpha I [\text{W}/\text{cm}^2]$, with $\alpha = 9.33 \times 10^{-14} \lambda^2 [\mu\text{m}^2]$. The method makes use of this change in ionization potential with intensity. It requires temporal overlap between the two pulses and also a spatially homogeneous distribution of infrared-beam intensity over the size of the harmonic beam. The energy of the photoelectrons is dependent on the instantaneous value of the ionization potential, which is changing rapidly in time according to the variation of the infrared-pulse intensity.

The presence of the infrared manifests itself in three ways in the XUV photoelectron energy spectrum. First, a down-shift of the mean energies due to the increased value of the ionization potential. Second, a broadening of the peaks due to the fact that the intensity of the dressing pulse is not constant during the presence of the XUV pulse. Finally, the apparition of 'sidebands' in the electron spectrum, as a consequence of multiphoton free-free transitions induced by the dressing light.

The characteristics of the shift, broadening and sideband amplitude depend on the delay of one pulse with respect to the other. If the two pulses come peak to peak the infrared intensity does not change too much during the XUV pulse and the extra broadening of the peaks in the electron spectrum is very small. On the other hand the shift of the peaks in this situation will be maximum. If the XUV arrives during the rising edge of the infrared pulse, where the intensity changes very fast, the broadening is large, while the shift is less. This region of quasi linear variation of the infrared intensity in time is the most suited for time measurements of short XUV pulses, because it implies a linear dependence on time for the U_p mapping of the pulse duration into broadening of electron peaks. This duration can then be derived from the FWHM of the corresponding photoelectron peak.

Theoretically the method can provide accurate measurement of very short pulses. An infrared Gaussian pulse of 50 fs duration and 10 TW/cm² peak intensity changes the ionization potential by 20 meV per femtosecond around the inflection point. An electron spectrometer having a resolution of 20 meV can measure broadening differences of this magnitude, implying an accuracy of 1 fs for the time measurement. Independent of this accuracy, there is a lower limit on the pulse duration that can be measured, however. For too short pulses the peak profile will start to overlap that of

3.3. Experimental setup

the nearest sidebands, making it impossible to determine the broadening. The lower limit is about 3 fs in the case of 800-nm light, but could be pushed even lower by using shorter dressing wavelength.

3.3 Experimental setup

For the experiment, a Ti:sapphire laser system has been used, producing pulses of 40 fs, at a central wavelength of 800 nm and a repetition rate of 1 kHz, with energies up to 8 mJ. The beam was divided by a mask and an iris in an annular part used for the generation of the harmonics and a small central part (diameter up to 2 mm) used as a dressing beam [84] (see the setup in Fig. 4.2). The mask was implemented as a metal ball with a diameter of 8 mm, having a central octagonal hole designed such that on rotation of the ball around the vertical axis all sides of the hole move symmetrically towards the center thus keeping the shape the same while reducing the size of the hole. The energy in the central part of the beam could be adjusted from zero to a maximum of 60 μ J. The energy in the annular beam can be changed by modifying the iris diameter, and it was usually kept at 3 mJ for the best harmonic signal. The masked beam was focused by a 1-m focal-distance lens on a continuous-flow Ar jet, and the position of the focus with respect to the gas jet was adjusted for a maximum harmonic yield. The intensity in the focus was $\simeq 100$ TW/cm². The harmonics propagate in the direction of the fundamental. Somewhere after the focus an image of the masking device forms, and the infrared recovers a sharply delimited annular shape. The outer ring is blocked there by a 2.5-mm pinhole, and only the generated harmonics and the central infrared beam are transmitted into a magnetic-bottle spectrometer chamber. At this position of the pinhole, the mask image is demagnified by a factor of 2. The two beams are refocused on a second Ar jet by a spherical off-axis tungsten-coated mirror with a focal length of 35 mm, and the photoelectrons are detected at the end of the time-of-flight (TOF) tube by microchannel plates. This setup guaranties optimal alignment on the same axis and makes possible the determination of the absolute zero of the delay. Data acquisition has been done using a transient-digitizer board at a sampling rate of 500 MHz, which allowed the acquisition of a full time-of-flight trace at 980 shots per second.

The diameters of the two beams on the spherical mirror are 2.5 mm for the XUV and 0.8 mm for the infrared. Consequently, the two FWHM in the focus are 0.88 μ m (for the 15th harmonic) and, respectively, 40 μ m for the infrared. This large ratio assures a homogeneous spatial distribution of the dressing-beam intensity over the focus of the XUV beam. The confocal parameter of the infrared beam is very long, and the diameter hardly changes on propagation in the volume seen by the electron spectrometer. The XUV beam, on the other hand, diverges much faster due to its small focal size and numerical aperture. The sensitivity area of the spectrometer has a radius of 125 μ m and at this distance the ratio of the two beam diameters is still

large, $\simeq 15$.

The two pulses could be delayed with respect to each other using two antireflection coated glass plates of 6-mm thickness, a small one for the central infrared beam and a large one with a hole in the center for the annular part of the infrared beam. The plates were cut from the same window, to ensure equal thickness, and thus knowledge about the absolute timing of the beams with respect to each other. The path of a beam through its plate depends on the incidence angle, so by tilting one plate or the other any of the pulses can be delayed. Close to normal incidence, the time delay has second-order dependence on the incidence angle, and very small delays can be obtained at easily measurable angles. For the dimensions of our plates, a delay of 1 fs could be obtained by a tilt angle of 1° . Another advantage of this way of delaying is that it does not affect the spatial overlap of the beams.

3.4 Results and discussions

The W-coated mirror is not wavelength selective and, hence, ionization of argon by all odd harmonics above order 11 is possible. Fig. 3.1a shows photoelectron energy spectra taken at different intensities of the infrared dressing beam and at zero delay between the two pulses. An intensity-dependent shift and practically no broadening are observed. Sidebands also appear at non-zero intensity. The shift measured as a function of the delay of the XUV pulse with respect to the infrared yields the temporal profile of the latter, if the harmonic pulse is much shorter than the infrared one. We observed that the maximum of the shift occurs for a delay of 4 fs, indicating that the harmonic pulse peaks 4 fs before the infrared maximum. In Fig. 3.1b we present spectra taken at constant intensity of the infrared beam but at different time delays between the two pulses. As the XUV is delayed towards the tail of the infrared the shift decreases and the peaks become initially broader and then narrow again. The maximum shift at 4 fs (0.7 eV) corresponds to a peak intensity of $\simeq 13$ TW/cm² in the infrared beam focus. The peak asymmetry present at small delays comes from the non-linearity of the temporal profile of the infrared pulse around the top.

The spectra can be modeled by a single bound level (the initial state) with a binding energy $|E_0| + \alpha I_{\text{IR}}(t)$ dependent on the instantaneous infrared intensity I_{IR} , coupled by a XUV pulse of electric field $E_{\text{UV}}(t)$ to a flat continuum. In this case the final population of the continuum level with energy E is proportional to

$$\left| \int_{-\infty}^{+\infty} \exp[-i(\hbar\omega_{\text{UV}} - |E_0| - E)t + i\alpha \int_{-\infty}^t I_{\text{IR}}(t')dt'] E_{\text{UV}}(t) dt \right|^2.$$

Using this expression for the profile of the photoelectron peak, we fitted the pulse shapes $I_{\text{IR}}(t)$ and $E_{\text{UV}}(t)$ to the experimental data, taking account of broadening due to the spectrometer resolution (20 meV).

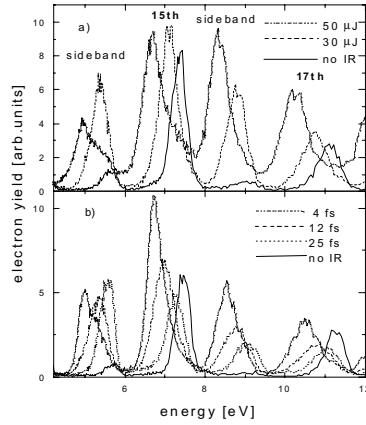


Figure 3.1: (a) Photoelectron spectra from ionization with harmonics in the presence of an infrared beam of various intensities. (b) Photoelectron spectra at 13 TW/cm^2 ($50 \mu\text{J}$) peak intensity in the infrared focus and at various delays of the XUV pulse with respect to the infrared.

By fitting the experimental shifts and the broadenings of the 15th-harmonic peak versus delay, a duration of $10 \pm 2 \text{ fs}$ (FWHM) has been determined for this harmonic (Fig. 3.2). The intensity profile of the infrared pulse, as determined by plotting the shift as a function of delay, is fitted well by a sum of two Gaussians, 33% 55-fs FWHM and 67% 15-fs FWHM. For the profile of the harmonic, a Lorentzian shape has been used. The experimental data are also plotted in Fig. 3.2 for comparison with the numerical results. The error bar of 2 fs mentioned above is mostly due to spectrometer resolution and imperfection in the fit of the infrared-pulse profile. The relatively long duration of the XUV pulse with respect to the one expected from the order of the harmonic is probably an indication of the saturation of the harmonic-generation process. The effective non-linear index is then about 4, yielding a harmonic pulse twice shorter than the fundamental.

At the infrared intensity used for the shifting, the formation of sidebands is completely saturated, and each harmonic peak is expected to have several sidebands. Thus contributions from the sidebands of the 13th, 17th and 19th harmonic add to this peak, and the determined duration is a sort of average over these harmonics. It also implies that the amplitude of the photoionization peaks becomes a function of the infrared phase and intensity. However, this does not affect the outcome of the present method where all the information is derived from the spectral profile of a single peak. It should be pointed out that the procedure for obtaining the XUV pulse duration involves taking the spectra at only one delay. Although this operation is reasonably

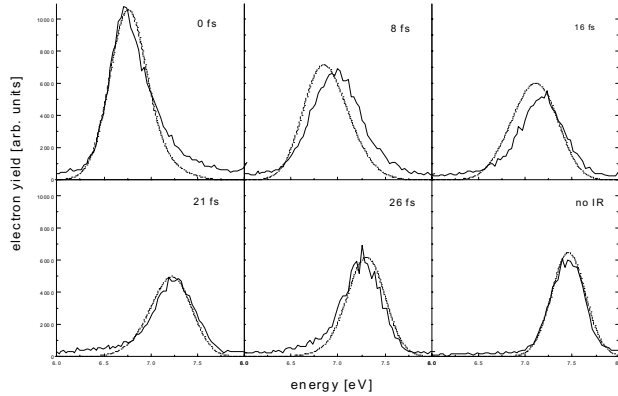


Figure 3.2: *Experimental data (solid line) and numerical simulations (dashed line) of the photoelectron peak corresponding to the 15th harmonic at different delays and $13 \text{ TW}/\text{cm}^2$ peak intensity of the fundamental. A duration of 10 fs for the harmonic has been used in the simulations.*

fast with the present setup (a few seconds) it still requires an averaging over a large number of laser shots in order to build up a decent electron-energy spectrum. It is not however out of reach of the magnetic bottle spectrometer to record a TOF spectrum over one single shot, perhaps at the cost of deteriorating the resolution.

Our method also allows the detection of an eventual chirp of the XUV pulse because in that case the maximum-shift position would not correspond to the narrowest peaks. The peaks would be the narrowest at a time delay for which the ponderomotive-shift contribution cancels the chirp. Such a chirp has been predicted [92] for harmonics in the cutoff. Our experimental data do not indicate the existence of any chirp, though. This might be a consequence of the fact that we did the measurements at low gas pressure in the harmonics jet, in order to avoid contamination of the harmonic beam with infrared light scattered on this jet (which would interfere with the infrared in the dressing beam). In an improved setup this scattered light could be blocked by a filter, which at the same time could be used to select a single harmonic.

3.5 Conclusions

In conclusion, we presented an alternative method for measuring very short pulse durations in the XUV, and demonstrated it on high-harmonic radiation. In principle it could be used on any XUV pulse with a bandwidth smaller than the photon energy of the dressing beam, provided that it can be synchronized with the laser.

Chapter 4

Reconstruction of attosecond beatings

In principal, the temporal beating of superposed high harmonics obtained by focusing a femtosecond laser pulse in a gas jet can produce a train of very short intensity spikes, depending on the relative phases of the harmonics. We present a method to measure such phases through two-photon, two-color photoionization. We found that the harmonics are locked in phase and form a train of 250-attosecond pulses in the time domain. Harmonic generation may be a promising source for attosecond time-resolved measurements.

4.1 Introduction

The advent of subfemtosecond or attosecond (as) light pulses will open new fields of time-resolved studies with unprecedented resolution. Just as subpicosecond or femtosecond (fs) pulses have allowed the resolution of molecular movements, attosecond ones may enable us to resolve electronic dynamics. Several groups in the world are researching the generation of subfemtosecond pulses. Large bandwidths are required to support such pulses: the spectrum of a 200-as unipolar pulse covers the optical spectrum from the near infrared to the extreme-ultraviolet range. There are two known kinds of sources with the potential to produce coherent radiation over such bandwidths: high harmonic generation (HHG) [47,93] and stimulated Raman scattering [94,95]. Both methods have, in theory, the tendency to produce not a single, but rather a train of closely spaced pulses. Even such trains of attosecond pulses, applied to experiments, can open a new field of attosecond physics, allowing the study of processes of unprecedented speed. Moreover, methods of selecting only one pulse from the train have already been suggested [96]. The present experimental study focuses

4.1. Introduction

on HHG and demonstrates that this process indeed results in a train of attosecond pulses.

If an intense femtosecond laser is focused on an atomic gas jet, the non-linear electronic response of the medium causes the generation of higher harmonics of the laser field. The harmonic spectrum consists of a series of narrow peaks separated by twice the frequency of the driving field, and it extends far into the extreme ultraviolet regime [47]. For reasons of symmetry, only odd harmonics are emitted. Although high harmonics have been a familiar presence in many laser laboratories for more than 10 years, and although their generation is well understood experimentally and theoretically [52, 55, 56], some features of the generation process have remained inaccessible to direct experimental measurement. In particular, questions relating to the time profile of the harmonic emission are not easily resolved. Measurements of the harmonic pulse duration shows that it is much shorter than that of the driving laser [81, 97, 98], and lasts for only a few femtoseconds. In addition to questions related to the pulse envelope of an individual harmonic, another measurement difficulty involves beating between various harmonics. This occurs on a subfemtosecond time scale, and no streak camera or autocorrelator developed for this wavelength range can reach such a high resolution.

Theoretical results for the temporal characteristics of the generation process are much more detailed, and predict that the harmonics are locked in phase. If this is correct, a group of neighboring harmonics could beat together to form a very short intensity spike, provided they all add constructively at the same instant. Because of the constant frequency spacing of the harmonics, this would happen twice per optical cycle of the driving laser. The duration of the spike could be as short as $T_{\text{laser}}/2N$, (N being the number of phase-locked harmonics) [99, 100]. At a laser wavelength of 800 nm, and $N = 5$, the output pulse would then be in the attosecond regime.

Numerical calculations for the single-atom response indicate that the harmonics are not emitted exactly in phase, leading to the generation of not one, but several spikes per optical half-cycle [101]. In practice, propagation of the electromagnetic fields through the medium affects the spatial and temporal coherence properties of the harmonic radiation. The theoretical conclusion is that per half cycle only one of the interference spikes survives the propagation, thus forming a train of attosecond pulses spaced by half the period of the fundamental [101–103].

A recent experiment [104] has confirmed that the harmonic radiation contains structure on an attosecond scale. However, as that experiment was based on measuring the field autocorrelate, which is equivalent to measuring the power spectrum of the harmonics, no information could be obtained about the relative phases of the harmonic components. It is exactly those phases that determine if the harmonic field exhibits strong amplitude modulation (i.e., forms an attosecond pulse train), rather than being a frequency-modulated wave of approximately constant amplitude.

Our experiment approaches the problem from a direction closely related to the theoretical work of Veniard *et al.* [105]. We seek to determine the phase relation

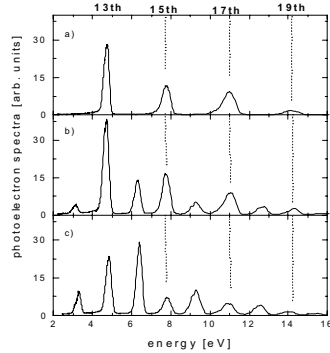


Figure 4.1: Photoelectron spectra of argon ionized by a superposition of odd harmonics from an infrared laser (a). In b and c co-propagating fundamental radiation was added, causing sidebands to appear in between the harmonic peaks. Changing the time delay between infrared and harmonics from -1.7 fs in b) to -2.5 fs in c) causes a strong amplitude change of the sidebands.

between the contributing harmonics by considering them in pairs. The periodic beat pattern of such a pair can be related to the phase of the infrared (IR) light from the driving laser according to how the combined fields ionize atoms. The intensities of the individual harmonics are too weak to cause non-linear effects on the target atoms, and thus only cause ionization by single-photon processes, each harmonic producing photoelectrons according to Einstein's equation for the photoelectric effect. The IR field, however, can easily be made to induce additional multiphoton transitions in the continuum [83]. Ionization with a harmonic photon can then be accompanied by absorption as well as emission of different numbers of IR photons. In the electron spectrum, this results in the appearance of sidebands (Fig. 4.1).

4.2 Theoretical description

At low IR intensities, where the problem can be treated in second-order perturbation theory, each harmonic creates only a single sideband on each side. These sideband peaks appear at energies corresponding to even multiples of the IR photon energy, and are thus located in between the peaks caused by the harmonics themselves. Only the two nearest harmonics contribute to each sideband peak, each through two quantum paths (Fig. 4.2) differing in the order in which the various photons are participating. According to Fermi's golden rule, the total transition probability from the initial ground state ψ_i , with energy E_0 , to all final states ψ_f (where f represents the angular quantum numbers of the continuum electron) at the sideband energy $E_q = E_0 + q\hbar\omega$

4.2. Theoretical description

is proportional to

$$S = \sum_f \left| M_{f,q-1}^{(+)} + M_{f,q+1}^{(-)} \right|^2,$$

with

$$M_{f,q}^{(\pm)} = \langle \psi_f | D_{\text{IR}}^{\pm} (E_q - H)^{-1} D_q^+ + D_q^+ (E_{\pm 1} - H)^{-1} D_{\text{IR}}^{\pm} | \psi_i \rangle.$$

In these expressions, \hbar is Planck's constant divided by 2π , ω is the IR field frequency, H is the atomic Hamiltonian, the dipole operators D^+ correspond to the energy-increasing part of the electromagnetic perturbation,

$$E(t) \cdot r = D^+ e^{-i\omega t} + D^- e^{i\omega t},$$

and their complex conjugates D^- to the energy-decreasing part. (The rotating-wave approximation is used.) The IR field is present as D^- in $M_{f,q+1}^{(-)}$, because of the emission of the IR photon, and it thus contributes a phase of the opposite sign with respect to $M_{f,q-1}^{(+)}$. Explicitly writing the phases $D^{\pm} = D_0 e^{\pm i\varphi}$, the interference terms in S become $A_f \cos(2\varphi_{\text{IR}} + \varphi_{q-1} - \varphi_{q+1} + \Delta\varphi_{\text{atomic}}^f)$, where $A_f = 2 \left| M_{f,q-1}^{(+)} \right| \left| M_{f,q+1}^{(-)} \right|$. Delaying the IR field by a time τ with respect to the harmonic fields sets $\varphi_{\text{IR}} = \omega_{\text{IR}}\tau$. By experimentally recording the magnitude of the sideband peak as a function of τ , and fitting a cosine to this, we determine $\varphi_{q-1} - \varphi_{q+1}$. The appearance of $\Delta\varphi_{\text{atomic}}^f$ is a consequence of the intrinsic complex phase of the matrix elements [106,107], resulting from $(E - H)^{-1}$ being applied at an energy in the continuous atomic spectrum. The turn-on boundary condition prescribes in ω_q an infinitesimal positive imaginary part $i\eta$, which defines the integral in the spectral representation of $(E - H)^{-1}$ as a real principal-value integral minus an imaginary delta function $i\pi\delta(E - H)$. This phase is small and can be obtained from established theory with high precision (Table I).

sideband	$\Delta\varphi_{\text{atomic}}^f$ [rad] / amplitude A_f [arb. units]			
	(1,0):(1,0)	(1,0):(3,0)	(1, \pm 1):(1, \pm 1)	(1, \pm 1):(3, \pm 1)
$E_0 + 12\hbar\omega$	0.438 / 6094	0.060 / 3659	0.125 / 1914	0.060 / 2440
$E_0 + 14\hbar\omega$	0.292 / 5135	0.102 / 2311	0.125 / 1281	0.102 / 1541
$E_0 + 16\hbar\omega$	0.221 / 3645	0.100 / 1349	0.108 / 763	0.100 / 899
$E_0 + 18\hbar\omega$	0.192 / 2444	0.090 / 742	0.090 / 427	0.090 / 494

Table I. *The atomic phases $\Delta\varphi_{\text{atomic}}^f$ and the relative strengths A_f of each two-photon transition responsible for the sideband peaks (angular and magnetic quantum numbers between brackets).*

4.3 Setup and results

The experimental setup has been described in detail in the previous chapter [97]. Briefly, we mention that the beam of a titanium:sapphire laser (800 nm, 40 fs, 1 kHz) is split by a mask in an outer, annular part (3 mJ) and a small central part (30 μ J). Both parts are focused by a +1 m lens into an Ar jet (see Fig. 4.2), where the smaller focus of the annular part generates harmonics (XUV). After the interaction with this first jet, the annular part is blocked by a pinhole and only the central part of the IR and the harmonics are allowed to propagate into a magnetic-bottle spectrometer. At an intensity of $\simeq 100$ TW/cm² many different odd harmonics are generated, but the tungsten mirror used to relay the beam into the electron spectrometer cuts off the spectrum beyond harmonic 19. The light is refocused by the mirror (35-mm focal length) onto a second Ar jet and the electrons resulting from photoionization in this jet are detected at the end of the time-of-flight tube by microchannel plates. The central part of the laser beam provides the IR light used to induce the sidebands. The two parts of the beam can be delayed with respect to each other using antireflection-coated glass plates (6 mm thick) cut from the same window. The plates could be aligned parallel with each other within a precision of 0.01°. The path of any of the beams through its plate depends on the incidence angle, which can be changed by rotating the plate. The plate responsible for the delay of the central part of the beam is mounted on a computer-controlled rotation stage, that can make steps of 0.005°. Very small delays can be achieved with it, because close to the normal incidence, the time delay has second-order dependence on the incidence angle. Given the dimensions of our plates, a tilt of 1° produces a delay of 1 fs of the pulse.

The spectrometer is observing an area with a radius of 125 μ m, located 1.5 mm before the focus of the spherical mirror. This was done in order to avoid the 180° phase slip that occurs when a light beam goes through a focus, and assures that the relative phase of IR light and harmonics stays constant over the observed volume. The IR peak intensity can be estimated as < 1 TW/cm², too weak to alter the photoelectron energies by ponderomotively shifting the ionization potential [97]. The harmonic peaks in Fig. 4.1b and c appear at the same energy position as they do in Fig. 4.1a. The intensity is also way below the threshold for multiphoton ionization of Ar by IR only.

The amplitudes of the first four sidebands, integrated over all corresponding energy channels, are plotted as a function of the time delay τ in Fig. 4.3. Each point is divided by the total signal at that delay to compensate for fluctuations in the harmonic intensity (which, due to the high order of the generation process, is an extremely sensitive function of laser intensity). The curves are oscillating in phase with a periodicity of 1.35 fs (i.e., half of the IR field period). The good modulation depth (a factor of about 2) shows that the relative phases do not fluctuate too much over the beam profile, between shots, or within the profile of a single pulse. The oscillation period is that expected for the sideband interference, which is half of that

4.3. Setup and results

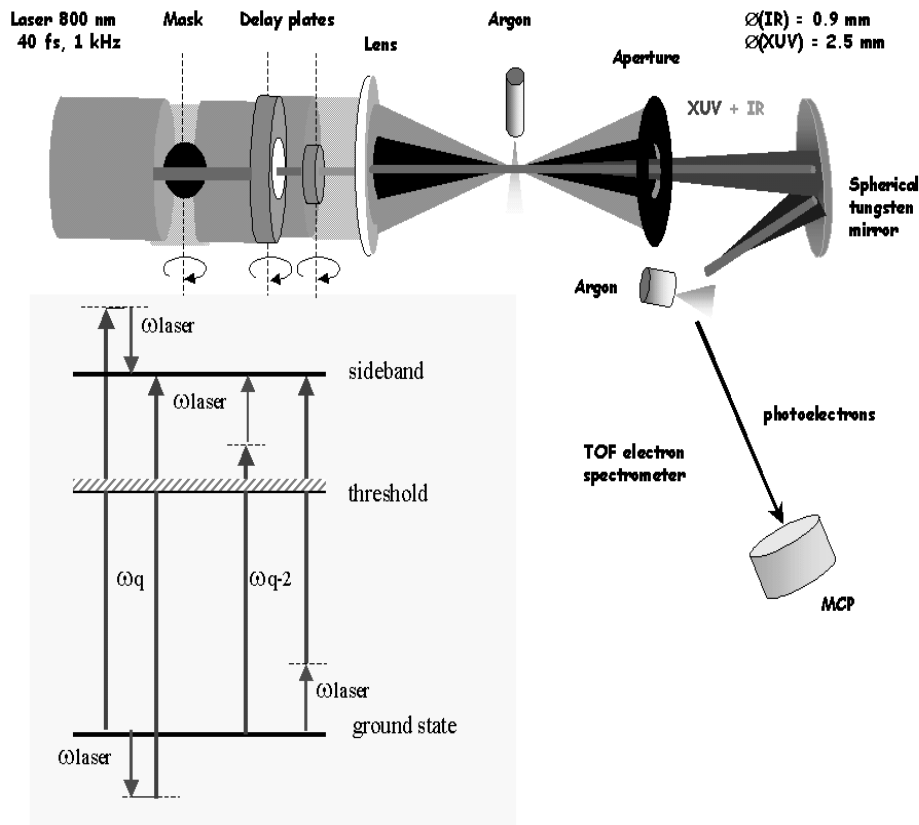


Figure 4.2: *Experimental setup.* The inset shows the quantum paths contributing to the photoelectrons generated in the second argon jet by mixed-color two-photon ionization. ω_{laser} is the infrared field frequency and ω_q equals $q\omega_{\text{laser}}$.

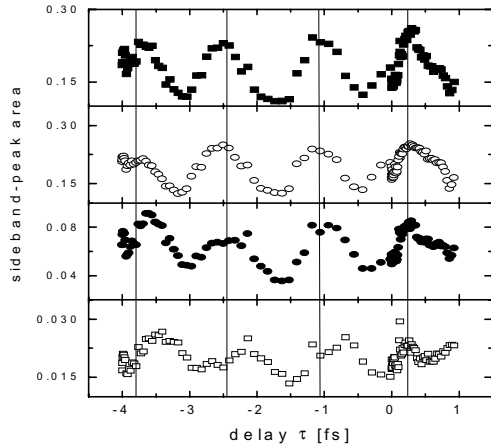


Figure 4.3: Area of the first four sideband peaks (to higher energies from up to down) as a function of the time delay between the infrared pulse and the harmonics. The first three curves oscillate in phase, the lowest one is forward shifted by 0.35 fs. The vertical lines are spaced by 1.35 fs, half the cycle time of the driving laser.

expected for interference between IR components in the two beam parts. (The gas pressures in the harmonics jet was deliberately kept low to avoid the contamination of the harmonics by scattered IR light.)

From the fitted pairwise phase differences, the phases of the involved harmonics (11 to 19) were found to be -2.6 , -1.3 , 0 , 1.8 , 4.4 radians respectively (arbitrarily assigning $\varphi_{15} = 0$). The standard deviation in these phases is about 0.3 radian. Together with the relative harmonic cross-sections (obtained from Fig. 4.1a and corrected for the different ionization cross-sections), they uniquely determine the temporal intensity profile of the total field (Fig. 4.4). This profile is thus found to be a sequence of 250-as peaks, full width at half maximum (FWHM), spaced by 1.35 fs. (The amplitude of the 11th harmonic was not directly measured. Since the modulation depths of all sidebands are similar, we can conclude that 11 is not much different in intensity than 13. In the calculations we used a value 1.5 times larger than the 13th-harmonic magnitude. Had it been twice smaller, the peak FWHM in Fig. 4.4 would have only been slightly longer.) Repeating this reconstruction several times with phases randomly modified according to the experimental standard error leads to very similar results, with a standard deviation of 20 as in the FWHM pulse duration. The phase differences of the first four harmonics are close, but not identical, so the resulting attosecond pulses will not be entirely bandwidth limited. Note that a constant phase

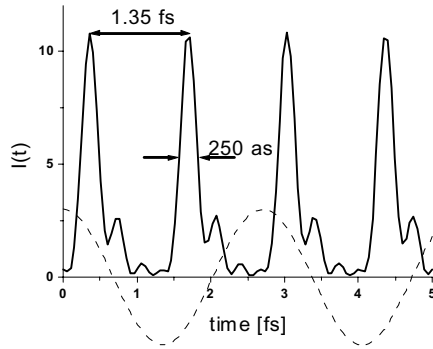


Figure 4.4: *Temporal intensity profile of a sum of five harmonics, as reconstructed from measured phases and amplitudes. The FWHM of each peak is $\simeq 250$ attosecond. The cosine function represents the infrared probe field for zero delay. Note that this reconstruction recovers 'typical' properties of pulses in the train by assuming all pulses are identical; in reality the pulse properties might have some variation around this 'average'.*

difference between harmonic pairs implies a linear (not flat) spectral phase distribution. This linearity is the only requirement for the building of attosecond pulses.

Provided the IR bandwidth is relatively small, our method in principle analyses all individual frequency components within the harmonics bandwidth simultaneously and independently, with each part of the sideband peak responding to the two frequency components that contribute to it. The sideband peak profile will thus show modulation with τ if phase differences vary over the bandwidth. Such profile changes are not apparent in our data, hence the harmonics must be frequency-modulated ("chirped") in a similar way. An identical chirp in all harmonics does not affect the intensity envelope of the attosecond pulses, only the phase of their carrier wave (which we can not measure).

4.4 Conclusions

The experimental evidence presented here for the existence of attosecond pulses in the process of HHG confirms theoretical predictions that the natural phase with which groups of neighboring harmonics are generated is sufficient to cause such pulse trains. In addition, our technique of phase measurement is a quite general one, applicable to deep in the extreme ultraviolet, and scales without difficulty to larger groups of harmonics. A measurement scheme for the phases may enable their purposeful ma-

nipulation (e.g., through dispersion when propagating through a gas cell), even if the harmonics were initially generated with undesirable phases. With such techniques, it should ultimately become possible to properly phase all harmonics emerging from the generation jet, leading to pulses perhaps as short as 10 as. The generation of these pulses still has to be investigated in more detail, and ways of control and selection have still to be developed before attosecond pulses can be routinely used as light sources in experiments.

Part II

Cluster Explosions

Chapter 5

Production of highly charged ions

We report production of highly-charged ions, C^{5+} and O^{6+} , obtained by Coulomb explosion of propane and, respectively, carbon dioxide clusters, exposed to laser pulses of $1 - 6 \times 10^{14}$ W/cm² intensity. At such intensities, only triply charged ions were created via tunneling ionization of isolated molecules. Carbon ions with energies of 1.2 keV and oxygen ions with energies of 2 keV have been detected. Some information about the explosion dynamics could be extracted from numerical simulations.

5.1 Introduction

Interaction of strong laser fields with atoms or molecules has been a major area of interest in atomic physics for the past decades. For long-wavelength radiation, in the near-infrared domain, the main ionization mechanism for intensities lower than 10^{14} W/cm² is multiphoton ionization via intermediate states. At higher intensities, the strong electric field can distort the atomic potential, lowering the barrier enough to make the electron able to tunnel through it [108]. Tunneling becomes dominant as soon as the Keldysh parameter $\gamma = \sqrt{I_p/(2U_p)}$ is smaller than 1. In this expression I_p is the ionization potential of the atom (or ion) and U_p is the ponderomotive energy given in eV by $9.33 \times 10^{-14} I[\text{W/cm}^2] \lambda^2[\mu\text{m}]$. The electron is even able to escape over the barrier for intensities larger than $I_{\text{OTBI}}[\text{W/cm}^2] = 4 \times 10^9 (I_p[\text{eV}])^4 / Z^2$, where Z is the charge state of the relevant ion [109]. For single charged ions I_{OTBI} is of the order $10^{14} - 10^{15}$ W/cm², but it gets very high ($> 10^{18}$ W/cm²) for production of highly charged ions, when removal of an inner-shell electron is required.

Because of their high local density and their efficient absorption of laser energy clusters offer an attractive alternative to atoms or molecules as a target substance

5.1. Introduction

for the creation of high-charge ionic states at much lower intensities than required by optical-field-induced (OFI) ionization of atomic gases. Many studies have been performed on noble-gas clusters, using short and intense laser pulses, concerning both ion and electron production, as well as radiation emission [110–112] and even production of fusion neutrons [113]. Ions with maximum energies of 1 MeV have been reported at laser intensities of $\simeq 10^{16}$ W/cm², charged as high as 40+ for Xe, or 25+ for Kr [114–116]. Such ions were obtained from explosion of clusters of less than 2500 atoms. Only Xe⁸⁺ and Kr⁸⁺ can be produced at 10^{16} W/cm² via over-the-barrier ionization of atoms. At the same intensities, electron spectra revealed the production of hot electrons, whose energies peak at 2.5 keV, besides slower ones, with energies less than 1 keV [116, 117].

The dynamics of cluster explosions received considerable attention up to date. Various models were proposed to explain the high charge states obtained in different experimental conditions and the non-thermal X-ray emission. McPherson *et al.* advanced the idea of coherent electronic motions in the strong laser field as being responsible for an enhanced probability of multiple ionization from an inner-shell [118]. Such motions then caused production of highly-charged ions (Xe⁴⁸⁺ and Kr²⁷⁺), which decay emitting X-ray radiation of 4 – 5 keV, in experiments performed with ultraviolet radiation at high intensities (10^{19} W/cm²) [110, 119]. In the ionization-ignition model the field of the neighbouring ions, created in the initial ionization events, assists the laser in lowering the ionization barrier, thus igniting the cluster to undergo further ionization [120, 121]. This model predicts very little dependence of the charge distribution on the cluster size, and it is only applicable to small clusters.

Classical simulations including both electron and ion dynamics proved that the space charge of the ions retains a significant fraction of ionized electrons in the core of a 55-atom cluster, diminishing the importance of ion-ion interactions and supporting the idea of treating the cluster as a nanoplasma [122]. According to the hydrodynamic model developed by Ditmire *et al.* [116, 123] collisions between ions (created initially by OFI ionization in low charge states) and laser-driven electrons form the main mechanism for further ionization of ions and heating of the electrons. The cluster will expand because of the pressure the free electrons exert on the ions. The fastest electrons will evaporate from the cluster [117], leaving the core positively charged. The heating is enhanced as soon as the electron density reaches 3 times n_{crit} (the density at which the laser frequency equals the plasma frequency). Experimental results showing that at a given cluster size (10^5 to 10^6 atoms for that experiment), there is an optimum pulse width for maximum absorption of laser energy, provide strong evidence for such resonant heating [124]. The ions will rapidly be ionized to high-charge states by the hot electrons. The combined action of the repulsive Coulomb forces between ions and the hydrodynamic pressure associated with the hot electrons will make the cluster explode. The electrons cool as they give some of their energy to the ions. The Coulomb pressure is more important for clusters of 2000 atoms or smaller, that do not retain much of the electrons [116]. For larger clusters, the

hydrodynamic expansion dominates, except for a short time after resonance, when the high electrostatic field (built up in the cluster because of the fast escape of the heated electrons) pulls the cluster apart, creating very energetic ions [125]. The big clusters expand more slowly, absorb more energy from the laser, and produce ionic states of higher charge in the expansion process.

Molecular clusters have received little attention up to now, in spite of the advantage they offer of studying elements that are hard to cluster in pure form [120, 126]. We focused our attention on clusters of carbon-containing molecules: carbon dioxide (CO_2) and propane (C_3H_8). K-shell ionization of carbon ions via barrier suppression requires laser intensities higher than $2.6 \times 10^{18} \text{ W/cm}^2$ because of the deep ionization potentials of C^{4+} (392 eV) and C^{5+} (490 eV). As shown on noble gases, a gas of clusters can very much lower the intensity needed for production of high-charge ions. Previous experiments produced fair amounts of C^{4+} at intensities around 10^{15} W/cm^2 , from small acetone clusters [120] and C_{60} [127]. Using big clusters as target, we exposed carbon atoms to low laser intensities (of the order 10^{14} W/cm^2) which, according to the equation for I_{OTBI} , can create at most doubly charged ions by tunneling ionization of carbon atoms. From the ion spectra, we also extracted information about the dynamics of the explosion.

5.2 Cluster-size determination

Fig. 5.1 presents a schematic of our experimental setup. A Ti:sapphire laser was used for the experiment, working at a repetition rate of 10 Hz. The characteristics of the pulse were 800 nm central wavelength and 170 fs duration, with pulse energies up to 6 mJ. The clusters were created in an adiabatic expansion that took place in a chamber installed on the top of an electron spectrometer, which could also be used for time-of-flight measurements on ions. A mixture of helium and a carbon-containing gas at high backing pressure (up to 30 bar) was made to flow into the low-pressure expansion chamber (10^{-7} mbar background pressure) by a pulsed, solenoid-controlled valve synchronized with the laser. Only the central part of the jet could pass into the spectrometer through a skimmer that was placed between the chambers, 2 cm below the nozzle.

The interaction of the laser beam with the clusters took place between the two extraction plates depicted in the figure by thick lines, in the interaction chamber of the spectrometer. The ions were detected in the time-of-flight chamber (1 m long) by a multichannel plate (MCP) connected to a computer through an HP oscilloscope, after being extracted from the interaction region and accelerated towards the MCP by negative voltages of 80 V on the plates and 2500 V on the flight tube. The solid angle that the spectrometer accepts is quite small, and is inversely proportional to the initial kinetic energy of the ions. Only particles with a velocity component in the direction of the detector can enter the flight tube, because the extraction voltage is not

5.2. Cluster-size determination

large enough to turn around ions that go in the opposite direction. In addition, the perpendicular velocity of the ions should not be larger than 1% of the total velocity they acquire in the flight tube, otherwise they will miss the 2-cm MCP.

Condensation in the free jet expansion produces van-der-Waals clusters of sizes that depend on the gas source parameters: pressure, temperature and nozzle size. In the absence of a general condensation theory that would exactly predict the average cluster size for a given set of initial expansion conditions (p_0, T_0, d) , empirical scaling laws were developed in order to correlate flow fields that are similar with respect to cluster formation or other expansion characteristics like terminal temperature. Through the concept of corresponding jets [128, 129] the scaling parameters have been extended for expansions of different gases [130, 131].

The scaling of the cluster size with the conditions of expansion is given by the Hagen parameter:

$$\Gamma^* = k(d/\tan \alpha)^q p_0 T_0^{-r}.$$

where:

- d is the diameter of the nozzle,
- α is the expansion half angle,
- p_0 is the source pressure,
- T_0 is the initial gas temperature, and
- $k = r_{\text{ch}}^{3-q} T_{\text{ch}}^{r-1} / k_B$.

In order to correlate rare gases with metals, the characteristics were defined as:

$$r_{\text{ch}} = (m/\rho)^{1/3} \text{ and } T_{\text{ch}} = \Delta h_0^0 / k_B,$$

where m is the atomic mass, ρ is the density of the solid state and Δh_0^0 is the sublimation enthalpy per atom at 0 K [130, 131].

The parameter r gives the scaling power of T_0 with p_0 for the same cluster size, when the nozzle diameter is not changed, and is related to the q parameter, that represents the scaling power of d with p_0 for the same output at constant source temperature, by the expression: $r = \frac{\gamma}{\gamma-1} - \frac{2-\gamma}{2(\gamma-1)}q$ (where γ is the adiabatic constant of the gas) [132]. The value of the q parameter is within 0.5 and 1, and can be determined precisely only from cluster size measurements. Experimental results give $q = 0.85$ for rare gases and metal vapours, and $q = 0.6$ for CO_2 [128, 132].

Based on experimental data, it is possible to affirm that the formation of clusters occurs if Γ^* exceeds 200, and that the clusters contain 100 atoms for $\Gamma \sim 1000$. The average cluster size is proportional to $(\Gamma^*)^f$, with $2 \leq f \leq 2.5$ [123, 131, 133]. Very big clusters of 10000 atoms (100 Å) were observed for $\Gamma^* > 50000$ [134].

It is difficult to experimentally determine the size of the clusters. We have applied the Rayleigh-scattering technique, which gives, in principle, information about the average size of the clusters. The Rayleigh-scattering partial cross-section is $\sigma(\lambda, \theta) \sim \frac{R_c^6(1+\cos^2 \theta)}{\lambda^4}$, where R_c is the cluster radius, λ is the scattered-light wavelength, and θ is

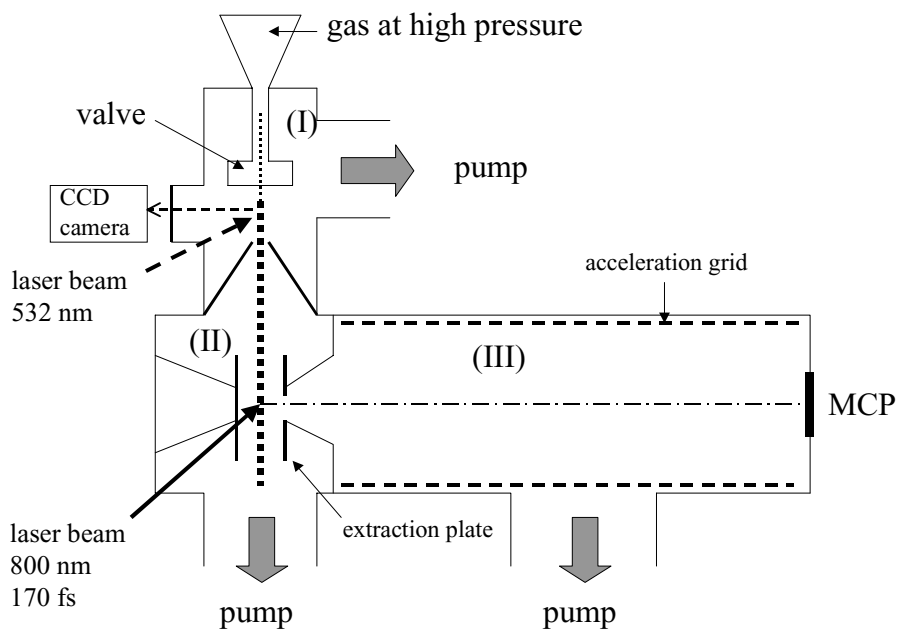


Figure 5.1: Schematic of the experimental set-up. (I) is the expansion chamber, where the clusters are formed. For the Rayleigh-scattering measurement the beam of a Nd:YAG laser was sent on the cluster jet, 5 mm below the valve, and the scattered light was detected on a CCD camera. The spectrometer consists of the interaction chamber (II), where the infrared laser irradiates the clusters, and the time-of-flight tube (III), where the ions are detected.

5.2. Cluster-size determination

the scattering angle. If n_c is the cluster density, the scattered signal S is proportional to $n_c\sigma$. Considering the expression for σ and the fact that R_c is proportional to $N_c^{1/3}$, N_c being the average number of atoms per cluster, we have $S \sim n_c N_c^2$. If all atoms condense into clusters, $n_c \simeq n_0/N_c$ and we can write $S \sim N_c p_0$, where n_0 and p_0 are the density and the pressure in the gas reservoir. If S scales as p_0^{f+1} , the average cluster size increases as p_0^f , with $2 \leq f \leq 2.5$, as measured in many experiments that have applied this technique [112, 116], confirming the result mentioned in the discussion about the Hagen parameter. (If no clustering occurs, S is simply proportional to p_0 .)

We did the measurements at room temperature ($T_0 = 300$ K) using a nozzle of $d = 500$ μm and $\alpha = 45^\circ$, and the only expansion parameter we could manipulate was the backing pressure p_0 . The beam of a Nd:YAG laser at the second-harmonic wavelength (532 nm, 6 ns, 20 mJ) was focused on the gas jet in the expansion chamber, 5 mm under the nozzle, by a lens of 250 mm focal distance. At this distance the collision frequency has dropped 10000 times compared to immediately after the nozzle, the condensation process stopped and the clusters flow free at terminal velocity [135]. Light scattered on the jet was detected at 90° by a calibrated CCD camera. Reflections of the laser beam on the windows were blocked by pinholes and the chamber walls were painted black in order to minimize the background signal.

The measurements were done initially on pure CO_2 and pure propane. In the case of propane, there was no scattered light detected for p_0 varied from 1 to 7 atm, so it can be concluded that no clustering occurred for this gas at these pressures. (For propane at room temperature, the phase transition to liquid takes place at $\simeq 8$ atm.) In the same range of pressures, the CO_2 forms small clusters, with a size of 120 molecules at 10 atm. N_c was found to be proportional to p_0^3 , a somehow large value for the power factor.

The difficult part in this measurement was the estimation of the proportionality constant between the scattered signal and the cluster size, because the signal given by individual atoms was below the detection limit. In $S = CN_c p_0$ the constant C is dependent on the detector sensitivity, on the light intensity and on the polarizability of the molecules. We estimated C from theoretical considerations for the pure gas from the expression $Cp_0 = N_{\text{tot}} n \sigma_m l a s$, where N_{tot} is the total number of photons in the laser pulse at the energy of reference, n the gas density in the focus, σ_m the molecular scattering cross-section at 90° , l the length of the focus, a the steric angle that hits the camera objective, and s the camera sensitivity in mV per photon. The camera sensitivity was determined by exposing the CCD chip to an isotropically scattered laser pulse of known energy. Then we could calculate it at different concentrations and beam energies according to: $C_{x\%} = x\% \cdot C_{\text{pure}} \cdot E_{\text{reference}}/E_{\text{beam}}$. The main error comes from the estimation of the gas density in the jet and translates into a relative error of approximately 50% in the average cluster size.

For rare gases, it was observed that the less 'ideal' the gas (the higher the critical-

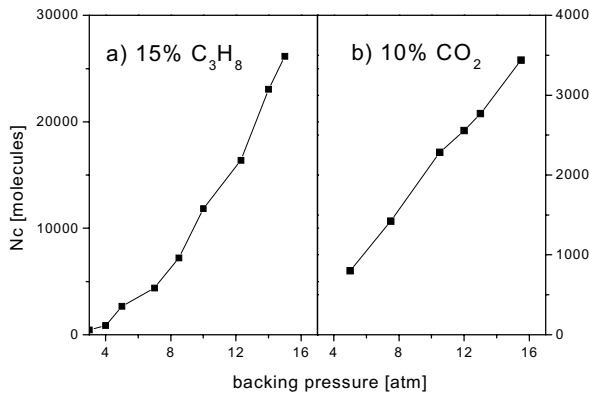


Figure 5.2: Average cluster size at different p_0 , derived from the Rayleigh-scattered signal, for propane (a) and carbon dioxide (b). Both gases have been mixed with He in the gas reservoir, in concentrations indicated on the figure. $N_c \sim p_0^{2.5}$ for propane, and $N_c \sim p_0^{2.3}$ for CO₂.

point temperature, for example), the highest the nucleation rate is [134]. Xe clusters better than Ar, and He forms clusters only at very low source temperatures. Pure propane is a very poor gas from the condensation point of view, although it has a higher critical temperature than CO₂ or Xe. But it should not be forgotten that it has a smaller adiabatic constant ($\gamma_{CO_2} = 1.3$, $\gamma_{C_3H_8} = 1.14$, also at 1 atm). For the same initial conditions, a gas of higher γ will cool faster than a gas of lower γ .

The formation of clusters can be enhanced by addition of a carrier gas, usually a light, monatomic gas. The mixture is meant to increase the adiabatic constant and to reduce faster the temperature, thus increasing the collision frequency of the expansion. It also makes possible the use of higher backing pressures than allowed by the thermodynamic properties of the seed gas. The γ constant of a mixture of He and propane, containing propane in proportion of 15%, is 1.4, and at 2 nozzle-diameters distance from the nozzle the density is twice higher than in the case of pure-propane expansion. Mixed with He, propane does form clusters starting from very low backing pressures, and reaching a value of 25000 molecules per cluster at 15 atm (Fig. 5.2a). N_c scales proportional to $p_0^{2.5}$. As the clusters grew larger with p_0 , the scattered signal increased above the saturation limit of the detector sensors, and the energy in the incident beam had to be reduced. The attenuation was taken into account in the calculation of N_c .

Mixing with He also improves the results for CO₂: the onset of clustering falls to

5.3. Cluster explosion

around 3 atm, and the power law changes to $N_c \sim p_0^{2.3}$. Clusters containing more than 3000 molecules are obtained beyond 14 atm (Fig. 5.2b). The cluster size is much lower as compared to a mixture of propane and He in spite of the higher γ . The reason might be the higher number of atoms contained in the molecule of propane, that increase the number of degrees of freedom per molecule, thus allowing a more rapid dissipation of the heat of cluster formation.

Unfortunately, apart from the average size, nothing can be learned about the cluster size distribution from the Rayleigh-scattered light measurements. If there is a significant fraction of the molecules that do not form clusters, the clusters that are present might have typical sizes much different from the average.

5.3 Cluster explosion

The central part of the jet passes through a skimmer with a diameter of 2 mm into the chamber where the interaction with the laser takes place. The skimmer cuts the wings of the jet, preventing the occurrence of frontal shock waves, and transmits further only a small amount of gas, thus maintaining a low pressure in the interaction chamber, 10^{-5} mbar on average. We shall discuss the results obtained for CO₂ and propane in two separate subsections.

5.3.1 CO₂

We took ion spectra from disintegration of CO₂ clusters, changing either the conditions of expansion or the characteristics of the laser pulse. The clusters were formed in an expansion of CO₂ mixed with He in proportion of one part in 10. At 20 atm backing pressure the average cluster size is 4500 molecules, as given by the Rayleigh-scattering measurement. The spectrum depends drastically on the intensity (Fig. 5.3). At 10^{14} W/cm² only two peaks are visible, each formed by the contribution of 2 ions, C³⁺&O⁴⁺ (that have the same mass/charge ratio and are indistinguishable in a time-of-flight measurement), and respectively C⁴⁺&O⁵⁺ (which could not be separated at our resolution). The O⁶⁺ peak clearly emerges from the wing of its neighbour peak at 1.5×10^{14} W/cm².

The calibration of the spectra with time was done on the H₂O⁺ peak, produced by ionization of the water molecules present in the background gas, and still visible when the valve is closed. The water molecules have very small initial velocities, and this calibration gives us information on the arrival time of ion species with zero initial kinetic energy. The detection method is such that we cannot distinguish between ions of the same m/q ratio. The time scale also contains information about the kinetic-energy distribution of the ions, in their displacement from the zero-velocity position. It is essential that the peaks do not overlap each other too much, in order for this information to be extracted unambiguously. The spectra were accumulated for 200

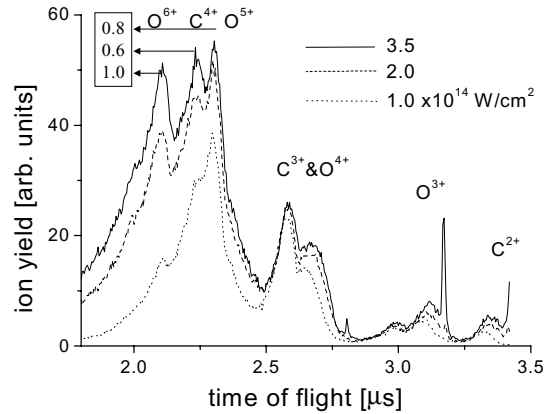


Figure 5.3: Ion spectra from Coulomb explosions of CO_2 clusters of $\simeq 4500$ molecules, at different laser intensities: 10^{14} W/cm^2 (dotted line), $2 \times 10^{14} \text{ W/cm}^2$ (dashed line), and $3.5 \times 10^{14} \text{ W/cm}^2$ (solid line). The little inset in the upper left corner shows in keV the kinetic energies of the most important ions, at the peak position.

shots and the average peak intensity was measured with a calibrated photodiode. The calibration was done in a separate measurement on the ionization threshold of He^+ . As the intensity increases, the signal gets stronger, but does not change in structure. Saturation is reached at $5 \times 10^{14} \text{ W/cm}^2$.

The very narrow peaks at 3.2 and $2.8 \mu\text{s}$ is due to ions of O^{3+} and, respectively, C^{3+} produced with almost zero initial velocity by direct OFI ionization of isolated molecules. These peaks appear at lower intensities than I_{OTBI} expected for atoms: O^{3+} at $2 \times 10^{14} \text{ W/cm}^2$, C^{3+} at $3.5 \times 10^{14} \text{ W/cm}^2$. The ions produced by Coulomb explosion appear at shorter time-of-flights and form broader peaks. By explosion, they are expelled with high initial velocities from the potential well caused by the evaporation of hot electrons. The excess kinetic energies at the peak indicate an average potential drop of 170 eV as ions depart to infinity. It acts differently on ions of different charge and this might explain why the $\text{C}^{3+} \& \text{O}^{4+}$ peak has a shoulder. The fastest ions are expected to come from the surface of the cluster, where electric fields are the strongest. The spectrum measured at $3.5 \times 10^{14} \text{ W/cm}^2$ shows O^{6+} ions of more than 2 keV , suggesting a maximum potential of around 300 eV at the surface of the expanding cluster. Because the peaks overlap, it is not possible to analyze each charge state individually.

A measurement of the ion spectrum at different backing pressures, 10 and 20 atm ,

5.3. Cluster explosion

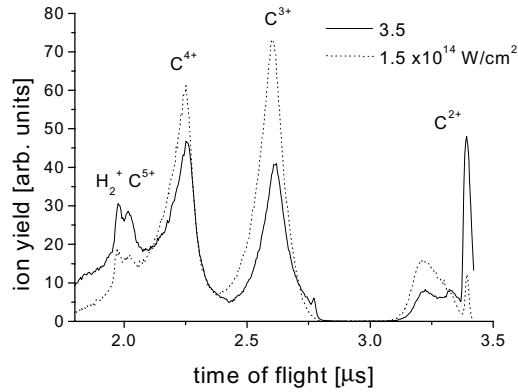


Figure 5.4: Ion spectra from Coulomb explosions of propane clusters of $\simeq 50000$ molecules, at two laser intensities: $1.5 \times 10^{14} \text{ W/cm}^2$ (dotted line), and $3.5 \times 10^{14} \text{ W/cm}^2$ (solid line).

reveals no change in the structure of the spectrum when increasing the average cluster size from 2000 to 4500 atoms.

5.3.2 C_3H_8

For the results presented in Fig. 5.4, the measurement was done on clusters of 50000 molecules on average, obtained from a mixture of 15% propane, at $p_0 = 20 \text{ atm}$. The ion spectrum from ionization of propane clusters shows carbon ions up to a charge state of 5+ and a peak corresponding to H_2^+ . The very narrow peaks correspond to ions created by direct OFI ionization. The ions from the much broader peaks are produced by Coulomb explosion of the laser-heated clusters. For the intensity measurement we did binning on a calibrated photodiode signal.

With only one mass present in the spectrum the peaks are fairly well separated, and it is relatively easy to plot the number of ions per charge state as a function of intensity (see Fig. 5.5). C^{5+} appears as a distinct peak at $\simeq 10^{14} \text{ W/cm}^2$. As the intensity increases, the amount of C^{4+} and C^{5+} is also increasing up to a saturation point after which it is slowly decreasing as the clusters are destroyed faster by the more intense laser. At $6 \times 10^{14} \text{ W/cm}^2$ the amount of C^{5+} is $\simeq 50\%$ that of C^{4+} . What happens after saturation is expected to be very dependent on the exact temporal pulse shape and focus geometry. Both of these are poorly known in our experiment, so we cannot draw any conclusion from the slight decrease of the ion signal in Fig. 5.5, at higher intensities.

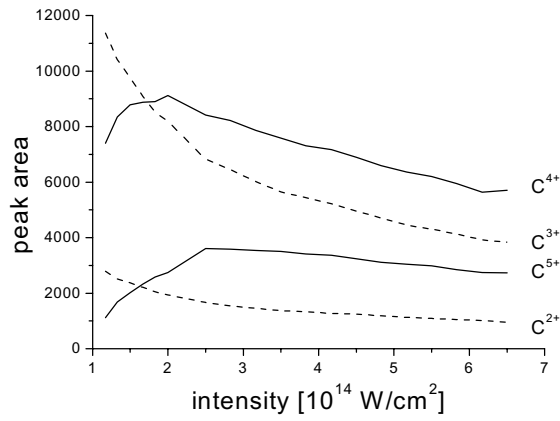


Figure 5.5: C^{n+} amount at different intensities, obtained from the ion spectra by integration of the corresponding peaks.

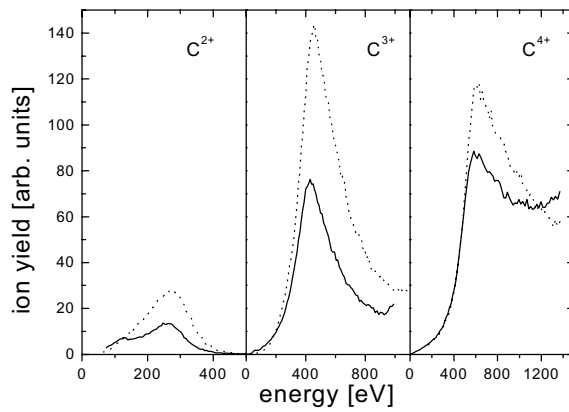


Figure 5.6: The peaks of C^{2+} , C^{3+} , and C^{4+} (from left to right) as a function of energy, at 1.5×10^{14} W/cm 2 (dotted line) and 3.5×10^{14} W/cm 2 (solid line).

5.4. Theoretical model of the explosion

The peaks of Fig. 5.4 could be also analyzed individually with respect to the energy of the ions. In Fig. 5.6 the peaks corresponding to three charge states 2+, 3+, and 4+, were plotted as a function of energy at the same intensities as in Fig. 5.4. A small correction was done in these graphs, for the fact that the acceptance angle of the spectrometer is smaller for ions of higher velocities. The C^{4+} ions acquire in the explosion energies of more than 1.2 keV, indicating a potential of 300 V at the surface of the cluster. The average charge per ion is $\simeq 3.5$. If all electrons were to leave the cluster, the radius of the sphere creating this potential would be $2.5 \mu\text{m}$, 125 times bigger than the initial cluster size. The cluster would reach this dimension only a few pulse durations after the pulse, which means that most of the free electrons were actually trapped in the cluster during the expansion, otherwise we would have seen higher ion energies in the spectrum. This implies the dominance of the hydrodynamic pressure in the process.

Electrons with kinetic energies lower than 300 eV cannot leave the potential well. They are left in the cluster volume, oscillating in the laser field. An electron of T_0 initial kinetic energy (gained by backscattering on ions) can get from the laser field an extra energy of maximum $\sqrt{8U_p T_0}$, which for $T_0 = 300$ eV, makes a total of 500 eV at 3.5×10^{14} W/cm². This can create even C^{6+} by collisional ionization.

5.4 Theoretical model of the explosion

To help interpreting the experimental results, we ran some numerical simulations of the propane-cluster explosion, using the simple classical model introduced by Ditmire [122]. We assumed that the exact initial location of the carbon atoms would not affect the later stages of the explosion very much. The carbon atoms were therefore arranged in a spherical subset of an FCC lattice, with lattice constant 4.7 Å. The proper volume of each atom is then 40 \AA^3 , which gives them the same density as in liquid propane. We considered only the carbon and neglected the protons. We want to have in the calculation a cluster with the biggest positive charge our computer can afford. Because the calculation time depends on the number of particles, we would have this positive charge as carbon ions rather than protons.

Initially only neutral atoms were filling the particle array, and free electrons added to the array later, as they were created by ionization. For each created electron, the charge state of the parent atom (or ion) was changed accordingly. The program calculates the total electric field at the position of each particle, and uses these values in the check for ionization events, and in determining the motion of the particles.

The instantaneous value of the laser electric field and the Coulomb-field value at the atom (ion) determine the conditions for ionization. The ionization can take place by tunneling or by inelastic collisions with (sufficiently fast) electrons. This last case was allowed to occur only if the impacting electron passes closer than 2.12 \AA from the ion (distance representing the radius of the proper volume), with a probability

that reflects the corresponding cross section. To this end we assumed that the target atom (or ion) was ionizing at a constant rate as long as a fast electron was within its proper volume. This collisional-ionization rate is given by the product of the Lotz cross section [136] with the relative velocity (extrapolated to its asymptotic value), divided by the proper volume. The expression of the Lotz cross section is, with a small approximation:

$$\sigma_L = a_L N_e \frac{\ln(K/I_p)}{KI_p},$$

where $a_L = 450 \text{ (eV)}^2 \text{ \AA}^2$, N_e is the number of electrons in the outer shell of the ion, K is the centre-of-mass energy, and I_p is the ionization potential of the ion [137].

The rate for tunnel ionization by the laser field is given by a more complex expression [123, 138]:

$$W_t = \text{factor} \frac{(2l+1)(l+|m|)!}{2^{|m|}|m|!(l-|m|)!} \left(\frac{2e}{n^*}\right)^{2n^*} \frac{I_p}{2\pi n^*} \left(\frac{2(2I_p)^{3/2}}{E}\right)^{2n^* - |m| - 1} \times \\ \times \exp\left(-\frac{2(2I_p)^{3/2}}{3E}\right),$$

in atomic units. E is the total field (laser+interaction) at the ion position, $e = 2.7183$, n^* is the effective principal quantum number ($n^* = Z/\sqrt{2I_p[\text{eV}]}$, Z being the core charge), l and m are the orbital and the magnetic quantum numbers. For $l = 0$, factor = 1, and for $l = 1$, factor = $(n^* - 1)/(n^* + 1)$. The rate is averaged over m for the $2p$ shell. At an intensity of $3.5 \times 10^{14} \text{ W/cm}^2$ the tunneling rate for neutral carbon is 0.83 fs^{-1} , for C^+ 0.11 fs^{-1} , and zero for all the other ionic states.

The electric field used in the expression for the tunneling rate was the combined field of the laser and the ions and electrons in the cluster. It was assumed that the distance to these other charges was for the largest part of the explosion large enough that over the distances relevant for tunneling such fields are sufficiently homogeneous to allow the use of the tunneling formula: due to their mutual repulsion ions never approach each other very closely. Electrons entering the proper volume of an atom could potentially create very high and inhomogeneous fields for which application of the tunneling formula would certainly not be justified; for this reason, tunneling was completely suppressed if there was an electron within this proper volume, the rate at those times being purely derived from the Lotz formula. The ionization probability during a time step of the numerical simulation is given by the product of the ionization rate and the time-step duration, $\delta t = 0.0024 \text{ fs}$ in our calculations. Whether ionization takes place or not is decided by comparison with a random number between 0 and 1. (Atomic units were used in the program.)

We did calculations for a cluster of 1500 carbon atoms (to which free electrons added to more than 9000 particles in total) irradiated by a sine-squared laser pulse of

5.4. Theoretical model of the explosion

160 cycles total duration. The algorithm used to calculate the motion of the particles is of the "leap-frog" type: the positions at time t were used to calculate the forces involved in the updating of velocities from $t - \delta t/2$ to $t + \delta t/2$, and the updated velocity was then used to calculate the new positions at time $t + \delta t$.

The most expensive part of the simulation, in terms of computational time, was the calculation of the Coulomb-force field. Because of the long-range nature of the Coulomb forces every pair of particles had to be taken into account. The duration of the force calculation thus scales proportionally to the square of the number of particles N . The interaction between particles i and j was modeled by a soft-core potential of the form $1/\sqrt{r_{ij}^2 + a_i + a_j}$, where a_i is a constant depending on the identity of particle i . An a constant was attached to each electron (the same for all of them) and ion (depending on the charge state), such that the value of the interaction term between an ion and an electron at $r_{ij} = 0$ equals the ionization potential of the respective ion. The square root and the division required to calculate the forces make this step, which already has the most unfavorable N -scaling, also computationally demanding. Using vector instructions available on the newer generations of CPUs made it possible to do the calculations for a 1500-particle cluster in a few days, which was considered the practical limit.

We used in the calculations a sinusoidal laser field (linearly polarized) with a sine-squared envelope, of 2.66 fs optical period, and 150 fs full width at half maximum (FWHM). We ran the calculations for a peak intensity of 3.5×10^{14} W/cm². The cluster contains 1500 carbon atoms (500 propane molecules), and the initial radius is 26.5 Å. The laser pulse starts at 0 fs and lasts for 426 fs, with the maximum intensity of 3.5×10^{14} W/cm² at 213 fs. Describing the process chronologically, we notice from Fig. 5.7 that the ionization starts after 100 fs from the beginning of the pulse, and for almost 50 fs most of the electrons are trapped inside the cluster. At this time, the resonant heating of the electrons begins, after the density dropped from a maximum of 3.8×10^{22} cm⁻³ to the critical value of 1.6×10^{22} cm⁻³, because of the expansion. The large number of electrons present inside the cluster points to an expansion triggered by the hydrodynamic pressure. The average charge state stays for a short while constant (4+), till the electrons get enough energy to further impact ionize the ions. (In fact, only 5% of the total number of free electrons is a result of tunneling ionization.) Slowly, the hot electrons are leaving the cluster volume, but 40% of the total number does not have enough energy to overcome the potential barrier. The average kinetic energy of the trapped electrons reaches a maximum of 300 eV, including the ponderomotive energy, at $t = 200$ fs, when the pulse intensity is close to maximum. By this time the final average charge state is reached (5.12+). (The electrons have a Boltzmann distribution of their energies.) From now on the electrons get colder, most of them are outside the cluster, and the expansion is mainly due to the Coulomb repulsion between ions. It can be deduced that the pulse duration is close to optimum for this cluster size. Calculations done using a pulse of 56 fs

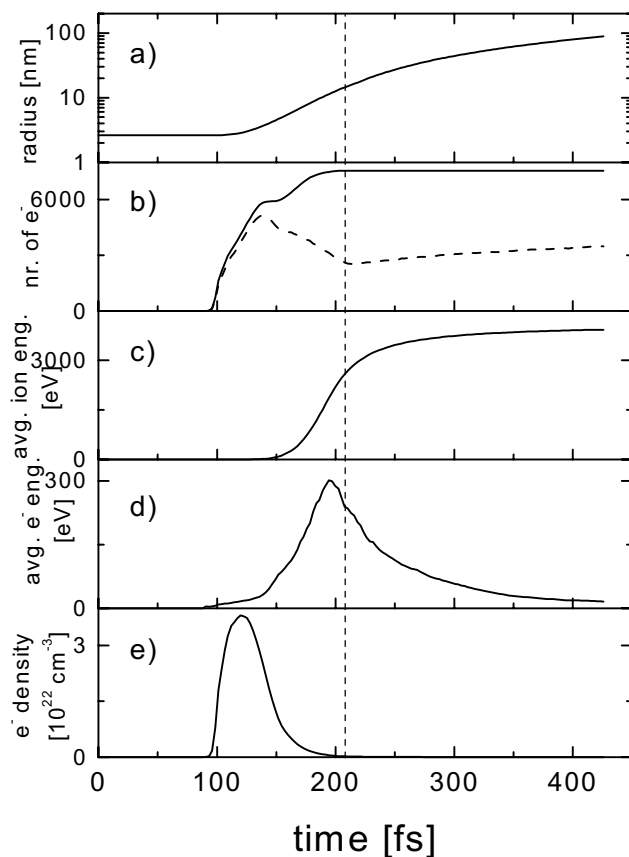


Figure 5.7: Results of numerical simulations for a 1500 atom cluster and a pulse of $3.5 \times 10^{14} \text{ W/cm}^2$ peak intensity and 150 fs FWHM. The graph represents as a function of time: the radius of the cluster (a), the total number of free electrons (solid line) and the number of free electrons trapped inside the cluster (dashed line) (b), the average kinetic energy of the ions (c), and of the trapped electrons (d), the electron density inside the cluster (e). The vertical dashed line marks the peak of the laser pulse.

5.4. Theoretical model of the explosion

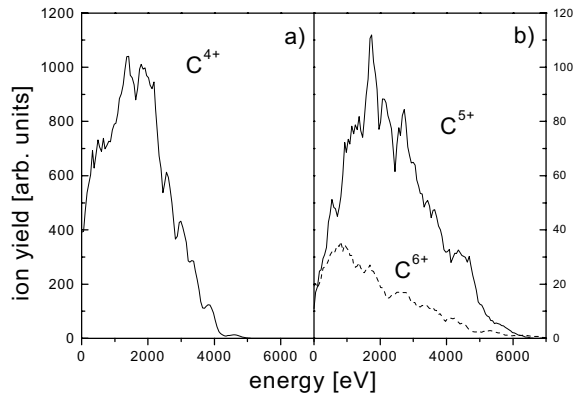


Figure 5.8: *Peak profiles resulting from averaging numerical calculations run at different intensities, for charge states: 4+ (a), 5+ and 6+ (b).*

FWHM, showed a 1.5 times smaller maximum of the average electron energy, reached after the peak-intensity moment. Calculations done for a cluster of 620 atoms, using our pulse of 150 fs FWHM, gave a maximum average energy of only 220 eV for the trapped electrons, and a final average ionic state of only 4.4+.

Some electrons that have left the cluster still feel the attraction of the cluster's positive charge and do not depart far from it. They are reincorporated in the cluster by expansion, but their number is quite small, around 500. The cluster radius at $t = 426$ fs is 890 Å, and the cluster charge is 4072+. After a maximum of 950 V at $t = 180$ fs, the potential at the surface of the cluster decreases rapidly to only 70 V at the end of the pulse. The final average energy of the ions is 3.9 keV. The saturation has been reached soon after the peak of the laser pulse, which indicates that mainly the hydrodynamic expansion is responsible for the high ion velocities. At the end, 33% of the ions is C⁶⁺ (in contrast to the experimental data, where no distinct peak corresponding to C⁶⁺ was measured), 46% C⁵⁺, and the rest C⁴⁺. It shall be stressed that we used a spatially homogeneous pulse in the calculations, which was not the case in the experiment.

The results from the calculation look quite different from those of the experiment. The main difference, however, is caused by the fact that the experiment integrates over a large range of intensities present in the laser focus, the lower intensities being much more abundant than the higher ones. The focal volume as a function of intensity is described by:

$$dV(I) \sim \frac{1}{I} \sqrt{\frac{I_0}{I} - 1} \left(\frac{I_0}{I} + 2 \right) dI,$$

where I_0 is the maximum intensity. To simulate such focal volume, we also ran calculations at six smaller intensities: 0.29, 0.35, 0.44, 0.66, 0.88, and 1.75×10^{14} W/cm². Nothing happens in the numerical simulations if the intensity is lower than 0.25×10^{14} W/cm². The integrated results can be seen in Fig. 5.8. The energy distributions of the main charge states (4+ and 5+) peak between 1.5 and 1.8 keV, indicating an average potential of 350 V at the surface of the cluster. (The experimental peaks depicted in Fig. 5.5 suggest a slightly lower potential of 300 V.) The profiles are much more similar to those measured in the experiment. The tails of the some peaks stretch beyond 3 keV. In the experimental spectrum these tails could not be distinguished from the peaks corresponding to higher-charge ions. All these numbers are closer to the experimental results than the values obtained from the peak-intensity calculation. With the volume integration, the number of C⁴⁺ ions produced is ten times larger than the number of C⁵⁺ and thirty times larger than C⁶⁺. In the experiment, we measured a C⁵⁺/C⁴⁺ ratio of 40% at 3.5×10^{14} W/cm². The amount of C³⁺ given by the calculations is far less than measured, and the maximum energy of these ions is only 200 eV.

It is interesting that the C⁶⁺ yield peaks at 1 keV, which might suggest that the highest-charge ions are not created at the surface of the cluster, but somewhere inside the cluster volume, in a region where less fields are present. From Fig. 5.9b we can see that by the end of the pulse (when no ionization takes place anymore), the C⁴⁺ ions are only present at the surface of the cluster, while C⁶⁺ ions are distributed over the entire volume. These results are obtained at 3.5×10^{14} W/cm². At the surface of the cluster the electron energy is lower, because the hottest electrons have either escaped the cluster or have been attracted towards the centre of the potential well, and the C⁴⁺ ions can survive ionization. The fields are also stronger at the surface because of lower electron density, and the ions from that region are accelerated more. The hottest trapped electrons are found mostly in the center of the cluster. At $t = 160$ fs, 1200 carbon ions are in the charge state 4+, 250 in state 5+, and they all fill the entire volume of, at that time, 5 nm radius (see Fig. 5.10). 25 fs later, the cluster radius is twice larger, the C⁴⁺ ions (in number of 470) are located in a shell at least 5 nm far from the cluster centre, and the 700 C⁵⁺ ions are now continuously distributed up to a distance of 8 nm from the centre. From the numerical calculations it looks like the ionization of the K-shell takes place predominantly in the core of the cluster, which is more or less neutral, and the ions originating there are not accelerated very much. At this time, 185 fs, the average ionic charge state is already 5+, the positive-charge density slightly exceeds the negative one (Fig. 5.9a), while the hydrodynamic pressure drives the cluster into expansion.

The differences between the numerical results and the experimental ones can be

5.4. Theoretical model of the explosion

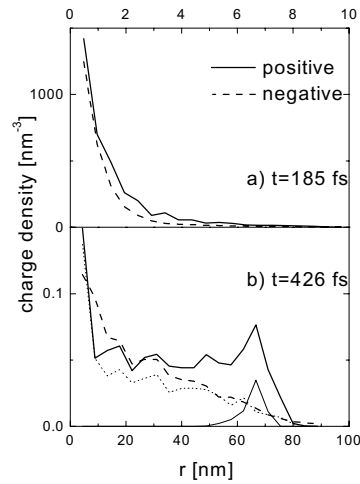


Figure 5.9: Positive and negative charge densities at two different moments of time: 185 fs from the beginning of the laser pulse (a), and at the end of the pulse (b). The pulse intensity is considered spatially homogeneous with a peak value of $3.5 \times 10^{14} \text{ W/cm}^2$. r is the distance from the cluster's centre. In the lower graph (b), in thin lines, the contributions of only 4+ ions (solid) and 6+ ions (dotted) are also depicted.

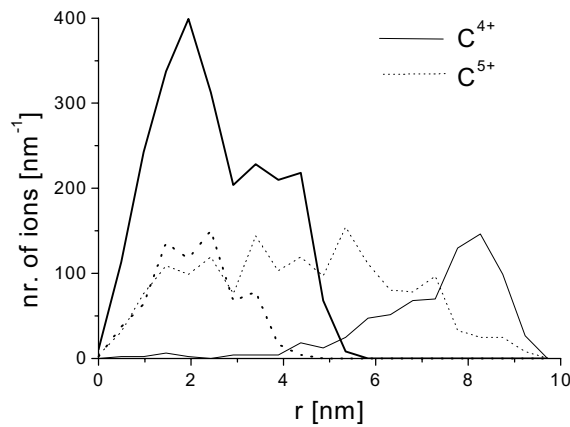


Figure 5.10: Number of ions as a function of the distance from the centre of the cluster, at $t = 160 \text{ fs}$ (thick lines) and at $t = 185 \text{ fs}$ (thin lines).

explained by the differences between the experimental conditions and the assumptions we made in the simulations, mainly regarding the focal intensity distribution, the cluster size and the cluster structure and composition. Note that the cluster used in the calculation still contains two orders of magnitude fewer particles than the propane clusters in the experiment. All quantities are expected to approach some asymptotic value with cluster size, though. Even if the simulation does not reproduce exactly the experimental results, it still gives a valuable insight in the way the explosion occurs.

5.5 Conclusions

We have reported in this paper some results obtained in an experiment of infrared-laser irradiation of clusters of propane (50000 molecules on average) and carbon dioxide (4500 molecules). The determination of the cluster size was done using the Rayleigh-scattering technique, an indirect method of measurement, yet the only one available in the absence of mass-spectroscopy means. Ions of C^{5+} and O^{6+} , with kinetic energies up to 2 keV, were produced starting from 1.5×10^{14} W/cm², a much lower intensity than required for tunneling ionization. Numerical simulations confirm the occurrence of resonant heating of the electrons by absorption of laser energy and the importance of this process in the production of highly charged ions by electron collisional ionization. The simulations indicate that the hydrodynamic pressure triggers the process of expansion, but it is the Coulomb repulsion that is responsible for the high energies of the ions.

At 800 nm, it proved to be very difficult to obtain completely stripped carbon ions, even when very large clusters were used. It was not possible to obtain only high-charge states because of the large dominance of low intensities in the focus that produced a lot of triply or quadruply charged carbon. It might be interesting to do this experiment at a single intensity, using a spatially shaped focus, because the calculations indicate that under this condition it is possible to create predominantly highly charged ions.

Chapter 6

X-ray emission from cluster debris

We present in this chapter a study of the radiation emitted after the explosion of clusters of propane and carbon dioxide. The highly charged ions produced in the explosion can resonantly transfer an electron from the buffer gas, helium, into highly excited states. Radiation of wavelength as short as 11.6 nm was measured from O^{5+} , and shorter than 4 nm from C^{4+} .

6.1 Introduction

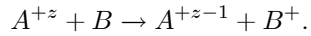
In the previous chapter, we described the measurement of ion production in Coulomb explosions of propane and carbon-dioxide clusters, describing also the mechanism of explosion. In this chapter we go one step further and analyze the radiation emitted after the process of explosion. We focused our research on the process of resonant charge transfer as the main mechanism of excitation in the explosion-produced highly charged ions. This study is part of the investigation of new sources of X-ray radiation, aiming at the development of a table-top X-ray laser. A description of lasing schemes in the X-ray domain and a survey of soft-X-ray lasers developed up to now are contained in the last section of **Chapter One**.

The clusters are formed by adiabatic expansion from high pressure into the vacuum. The condensation is enhanced by mixing carbon-containing molecules (propane or carbon dioxide) with a light gas, helium. The laser is interacting with the cluster jet very close to the nozzle, such that the clusters explode in an environment that contains a large amount of helium atoms. The helium also acts as electron source in the process of charge transfer. By collisions with the helium atoms, a highly charged ion can capture an electron into a highly excited state, from where the electron de-

6.2. Experimental setup

cays to the lower states, emitting photons. The capture process can be resonantly enhanced if the initial and final state are degenerate.

The process of resonant charge transfer is described by the reaction:



This process is the prevailing one at impact velocities lower than 10^3 km/s. At higher velocities, impact ionization becomes dominant. The total cross sections are reasonably large, 10^3 Mb for C^{3+} and 2.5×10^3 Mb for C^{5+} colliding with H at 50 keV [139]. The contribution is mostly due to resonant charge transfer to excited states that at some interaction distance cross the energy level of the electron on the source atom. The capture cross section for O^{6+} in collision with He, in the $n = 3$ levels of O^{5+} , bound at $\simeq -55$ eV is 7×10^{-16} cm², while in the $n = 4$ levels, bound 25 eV higher, it is less than 10^{-16} cm² (at 10 eV) [140].

In our experiment the neutral is helium, of ionization potential $I_p = 24.6$ eV, so only states of binding energy lower than this I_p are likely to capture electrons. There are also carbon neutrals around the focus, but with an average path of $\simeq 5$ μ m, the ions formed in the most intense part of the focus are not likely to escape to those regions without being partly neutralized. On the other hand, for the experiment on propane (C_3H_8), neutral H resulting from dissociation of H_2^+ can also transfer electrons, but the amount of H_2^+ is far less than helium.

We cannot exclude the case that some ions are excited by collisions with fast electrons in the explosion process, but numerical simulations have shown that the probability of such an event is very low (see **Chapter Five**).

We detect the photons by electron spectroscopy. The photon spectrum is reconstructed by measuring the electrons created by these photons in the ionization process of a detection gas.

6.2 Experimental setup

The experimental setup is similar to that described in **Chapter Five**, and can be seen in Fig. 6.1. The cluster explosion is done in a chamber installed on the top of a magnetic-bottle electron spectrometer. The jet containing the clusters flows horizontally through this chamber and is crossed by the laser at a distance of 5 mm from the pulsed valve. Highly-charged ions, hot electrons and photons are produced in the process of cluster explosion. The explosion chamber is separated by a 1.5-mm-diameter aperture from the ionization chamber, which acts as a gas resistance for differential pumping. The radiation emitted in the explosion propagates in a straight line to the ionization chamber, where it ionizes the atoms of the detection gas. A strong magnetic field applied between the pole-pieces collects half of the photoelectrons and guides them towards the time-of-flight (TOF) tube, where the

electron trajectories are parallelised by the adiabatic transition to a weak magnetic field. The electrons are detected after 1 m by micro-channel plates (MCP).

The energy resolution of the spectrometer is $\simeq 5\%$. A retarding voltage could be applied on a cylindrical grid, inside the flight tube, slowing down the electrons. Because of imperfect parallelisation of the trajectories of the high-energy electrons, cyclotron oscillations spaced by 80 ns can appear and can be detected in the spectrum close to the retarding-voltage edge, where the resolution is high enough. The over-all detection efficiency of the spectrometer is roughly 25%.

In the adiabatic expansion, the mixture of propane and helium or CO₂ and helium cools to the saturation point after which the molecules condensate into clusters. The light atomic gas, helium, enhances the cooling by increasing the adiabatic constant of the mixture, favoring the formation of clusters from gases that would not condense in pure form (the case of propane). The nozzle had a throat diameter $d = 500 \mu\text{m}$ and an angle of 45° . From the theory of expansion [135], we estimated that at 5 mm from the nozzle, the temperature dropped to $0.05T_0$, (where T_0 is the source temperature), and the particles reached already the terminal velocity $v_\infty = \sqrt{2c_p T_0}$ ($= 1.3 \text{ km/s}$ for a 15% mixture of propane and He, and slightly less for the mixture containing CO₂), where c_p is the specific heat of the mixture. The density changes in the expansion according to:

$$n = n_0 \left(\frac{T}{T_0}\right)^{\frac{1}{\gamma-1}} = n_0 \left(1 + \frac{\gamma-1}{2} M^2\right)^{-\frac{1}{\gamma-1}},$$

where γ is the adiabatic constant of the mixture (1.4 for 15% propane and 1.56 for 15% CO₂), and M is the Mach number, given by the ratio v/a , a being the local speed of sound. The location of the Mach disc, where the shock transition to a subsonic flow occurs, is quite insensitive to γ and is given by $(x_M/d) = 0.67(p_0/p_b)^{1/2}$. For a backing pressure $p_0 = 20 \text{ atm}$ and a background pressure $p_b = 10^{-10} \text{ atm}$, which we usually had in the experiment, the terminal Mach number (31 for propane) is reached after 150 m. Of course, our setup was much shorter, and the shock waves were of no concern. At 5 mm from the nozzle, the density is $\simeq 3 \times 10^{17} \text{ cm}^{-3}$, 1000 times lower than at the source, and the collision frequency drops 10000 times [135]. We conclude that by this distance, the clusters are already formed and follow a collision-free flow.

6.3 Results

When measuring the electron TOF trace, a very strong signal was detected at more than $1 \mu\text{s}$, which did not move or disappear when changing the retarding voltage. This signal was caused by secondary electrons produced in the collisions of the photoelectrons with the walls of the right-hand-side pole-piece. These secondaries had energies lower than 5 eV and were created in a region of high potential, thus unretardable

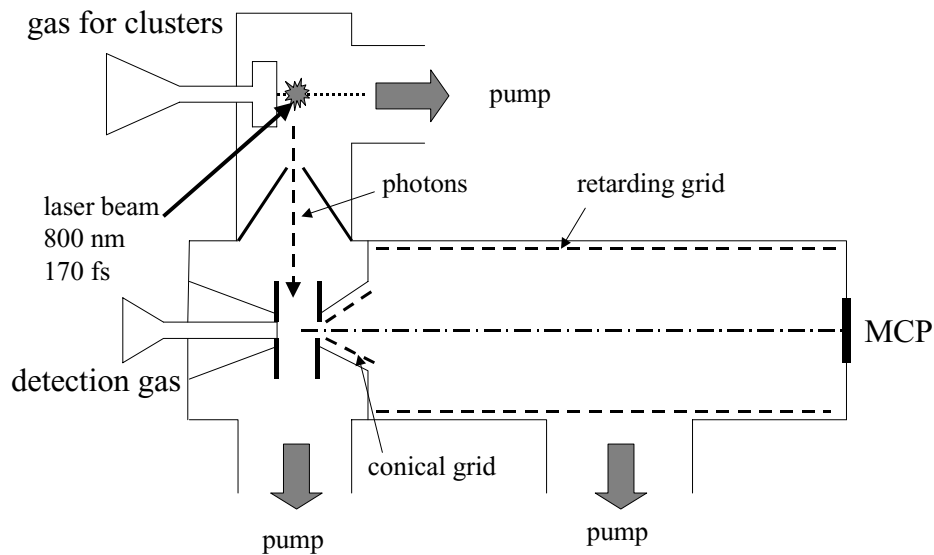


Figure 6.1: Schematic of the experimental set-up. (I) is the expansion chamber, where the clusters are formed. The jet flows horizontally and the infrared laser interacts with the clusters very close to the nozzle. The photons emitted by the highly charged ions produced in the explosion propagate into the spectrometer, interacting with the detection gas in chamber (II), and creating photoelectrons that are detected in the time-of-flight tube (III).

by the cylindrical grid. The conical grid inside the pole-piece was therefore disconnected from the grid in the flight tube, so that it could be connected to a voltage 5 V less negative than this main grid. This eliminated the secondary electrons from the spectrum, while still retarding the electrons as early as possible in the parallelization process.

Free electrons produced in the cluster explosions cannot pass through the strong magnetic field applied on the two conical pole-pieces, and thus do not give any contribution to the detected signal. Two vertical plates were installed below the skimmer to deflect ions from a possible trajectory from explosion chamber towards the ionization point. This, however, caused no change in the observed signal. We can safely say that the electrons detected in the TOF tube come exclusively from photoionization of the detection gas.

6.3.1 CO₂

In the first experiment, we irradiated clusters of CO₂ of 3500 molecules on average. This cluster size was determined with a relative error of 50%, using the Rayleigh-scattering technique (see **Chapter Five**). Although taken at a lower pressure, the ion spectrum is very similar to that in Fig. 5.3, obtained from somewhat larger clusters. The highest charge states observed were O⁶⁺ and C⁴⁺. The C⁵⁺ ions should have appeared at 2.2 μ s if produced with zero initial kinetic energy. This time region is covered by the tail of O⁶⁺ peak. The difference in ionization potential between O⁶⁺ and C⁵⁺ is 254 eV, and we tend to believe that no significant amount of C⁵⁺ was produced.

Note that for the spectra in Fig. 5.3 and 5.4, the cluster disintegration took place 20 cm from the nozzle, compared to a distance of only 5 mm now. We also used a more intense beam, 10¹⁵ W/cm², for the present experiment, focused slightly behind the gas jet in order to increase the focal volume, so that the clusters were exposed to an intensity of 3×10^{14} W/cm². For the radiation spectra, the volume increase made an important difference in terms of number of counts. Except for these differences, we maintained all the other parameters, of the gas source and of the laser, the same.

We used helium and neon as detection gases of the emitted radiation. Helium has the advantage of a simpler atomic structure, making it possible to unambiguously deduce the photon energy from the observed energy of the photo-electron. In the case of neon ($1s^2 2s^2 2p^6$), ionization can take place from both the $2p$ and the $2s$ level if the photon energy exceeds 48 eV. Nevertheless, the absorption cross-section of Ne is larger than that of He (σ_{Ne} changes between 9 and 3 Mb in the region 21.6 – 124 eV; $\sigma_{\text{He}} = 0.3 - 7$ Mb for the same region, with values lower than 1 Mb for more than 62 eV [141]). We were especially interested in the region 90 to 120 eV (10.3 – 13.8 nm), where the most energetic transitions occurred in O⁵⁺ (Li-like ion, with an ionization potential of 138 eV), from the $n = 4$ levels to the L-shell (see Fig. 6.2). Assuming C⁴⁺ to be the highest ionic state of carbon resulting from the explosion, the charge

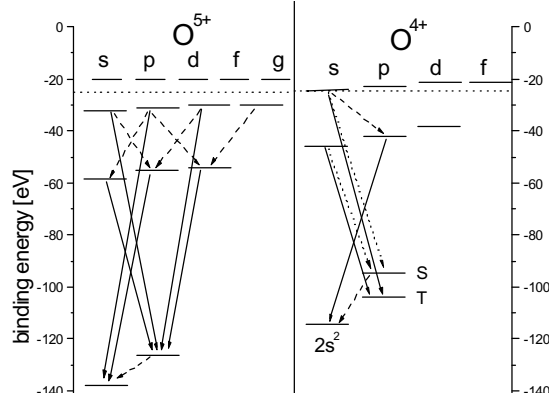


Figure 6.2: *Level schemes in O^{4+} and O^{5+} . The solid arrows indicate observed transitions, while the dashed arrows indicate transitions of too low an energy to be detected by photoionization of neon (also because of the secondary electrons), but which are expected to occur. The dotted arrows in O^{4+} represent singlet transitions that do not appear clearly in the spectrum. The singlets and the triplets for states of $n \geq 3$ in O^{4+} are too close to be depicted separately. The dotted horizontal line near the top of the figure marks the binding energy of the ground state of helium.*

transfer can produce then excited C^{3+} , also Li-like, but with $I_p = 64.5$ eV, from which we did not expect transitions of more than 40 eV.

The quality of the helium spectra is quite poor because of the low counting rate, but these spectra help us to distinguish between the lines due to $2p$ ionization and the lines due to $2s$ ionization in neon. We present in Fig. 6.3 photoelectron spectra of neon measured at different retarding voltages. The contribution of carbon consists of only three lines, all in C^{3+} : $3s, d \rightarrow 2p$ at 29.6 and 32.3 eV (peak **1**), and $3p \rightarrow 2s$ at 40 eV (peak **2**). The M-shell states in C^{3+} have binding energies of -27 to -24 eV ([142] for all energy levels in this chapter). All the transitions involved in the following discussion are presented in Table I, at the end of the chapter.

Oxygen accounts for most of the lines in the spectra, with transitions in three ionic states. The M-shell in O^{3+} has states of $n = 3$ bound between -25 and -33 eV, and probably all of them are populated via charge transfer but only the two transitions to $2p$ occur, at 44.3 and 52 eV (peaks **3** and **4**), because the $2s$ level is already occupied. The sub-structures of peak **4** is probably not real, but an artifact of the spectrometer, for reasons explained in the section describing the setup.

In O^{4+} , with the exception of $4s$, all levels of the N shell are bound above -24 eV, and do not capture electrons by charge transfer. Excited states of O^{4+} already have

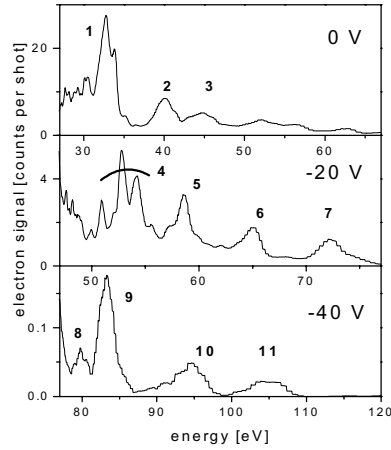


Figure 6.3: Neon spectra produced by ionization with photons emitted in the explosion of 3500-molecules CO_2 clusters, at different retarding voltages: 0, -20 , and -40 V, from top to bottom. The ionization potential of neon (21.6 eV) was added to the detected kinetic energies of the electrons, and to the retarding potential in the energy scale.

one electron in the $2s$ ground state, whose interaction with the excited electron splits the excited states into singlets and triplets. (If the spacing between the triplet and the singlet state is small, the state is depicted as only one line in Fig. 6.2.) The level $4s$ decays to $3p$ (17.6 eV for the triplet, and 18.6 eV for the singlet transition) or to $2p$ emitting a photon of 79.4 eV (peak **8**) in the triplet transition, or 71 eV in the singlet transition, which does not appear clearly in the spectrum. The transition $2s4p \rightarrow 2s^2$ at 91.5 eV (13.6 nm) was not detected. The singlet transition $2s3p \rightarrow 2s^2$, at 72.3 eV, is visible in peak **7**. From the four transitions $3 \rightarrow 2p$, only the triplet $3s \rightarrow 2p$ at 57.6 eV appears as peak **5** in Fig. 6.3. If the singlet $3s \rightarrow 2p$ at 50 eV might be hidden in the structure of peak **4**, there is no trace of the two $3d \rightarrow 2p$ transitions at 56.3 and 64.3 eV.

The lines of O^{5+} are the most important. The K shell of O^{5+} is completely filled and the ground state is thus $2s$. The levels of $n = 5$ are lying above the ionization potential of He, somewhere at -20 eV, and most probably are not populated (Fig. 6.2). The transition $5p \rightarrow 2s$ at 118 eV (10.5 nm) was not observed. The capture can occur on the levels of $n = 4$, bound in the range -32.4 to -30.6 eV. The transitions $4 \rightarrow 3$ have quite low energies, $23 - 28$ eV, making them of less practical interest, but in the transitions $4 \rightarrow 2$ photons of very short wavelength are emitted. The probability to go from $n = 4$ to $n = 2$ is higher than from 4 to 3 , excepting $4f$, of

6.3. Results

course (60% for $4s$, 77% for $4p$ and d). The transition $4s \rightarrow 2p$ at 94 eV (13.2 nm), contributes to peak **10** together with $4d \rightarrow 2p$ at 95.5 eV (13 nm). Peak **11** is the result of transition $4p \rightarrow 2s$ at 107 eV (11.6 nm). The three transitions $3 \rightarrow 2$ are also visible in the spectrum: $3p \rightarrow 2s$ as peak **9** (82.6 eV), $3s \rightarrow 2p$ as peak **6** (67.4 eV), and $3d \rightarrow 2p$ in peak **7** (71.7 eV).

The number of photo-electrons detected in our setup (N_e) is related to the number of photons that were originally produced in the cluster explosion and subsequent charge transfer (N_{photons}) by a proportionality factor that involves the gas pressures in both jets, photo-ionization cross sections, and geometric factors. The number of counts we have is $N_e = (N_{\text{photons}}/S)c_{\text{eff}}N_{\text{at}}\sigma_{\text{ionz}}$, where $S = 4\pi r^2$ ($r = 20$ cm being the distance from the source to the detector axis), c_{eff} is the detector efficiency ($\simeq 25\%$), N_{at} the number of atoms exposed in the sensitivity volume of the spectrometer, and σ_{ionz} the ionization cross-section of the detection gas. Even if the estimation of the detection gas density between the pole-pieces cannot not be done with much accuracy, it is still useful to give even a rough value for the number of photons produced after the explosion. The contribution of carbon via low-energy lines in C^{3+} (peaks **1** and **2**) amounts to 2×10^{11} photons, which is equal to the contribution of O^{3+} , O^{4+} , and O^{5+} together. The number of photons of 11.6 nm (peak **11**) is $\simeq 0.8 \times 10^9$, and the number of photons in peak **10**, from two transitions, is $\simeq 10^9$, according to our calculations. These values are corrected for the angular selectivity of the detection scheme, assuming isotropic emission, and they represent numbers of photons in the focus.

The ionization threshold for the $2s$ level in neon is $\simeq 47.6$ eV, so each peak in the spectra shall have a companion at an energy lower by $\simeq 26$ eV. For different reasons, these additional transitions do not appear clearly in the spectrum. Peaks **11**, **10**, **9**, and **8**, are small themselves, and their companions (approximately at 81, 69, 57, and 53 eV) are hidden by other peaks or in the background. The companions of peaks **7**, **6**, and **5** (at 46, 41, and 32 eV) coincide accidentally with peaks **3**, **2**, and **1**, respectively, and mix with other transitions.

6.3.2 C_3H_8 . Auger decay in argon

The large propane clusters, 50000 molecules on average, allowed the production of C^{5+} (Fig. 5.4). The detection of radiation was done with helium and argon. Because of the larger number of molecules in the cluster, the radiation emission increases, and the quality of the helium spectrum is pretty good, although not much is measured beyond 65 eV due to the rapid decrease of the helium cross section. Argon has a very high ionization cross section, $\simeq 12$ Mb from 15.8 eV, the ionization potential by removing a $3p$ valence electron, to 29 eV, which is the threshold for $3s$ ionization. After this range the cross-section drastically drops to $\simeq 0.2$ Mb, only to increase to 4 Mb at 248 eV, the edge of L-shell ionization [141]. It is this L-shell edge that makes argon very useful for our measurement, because it permits the detection of

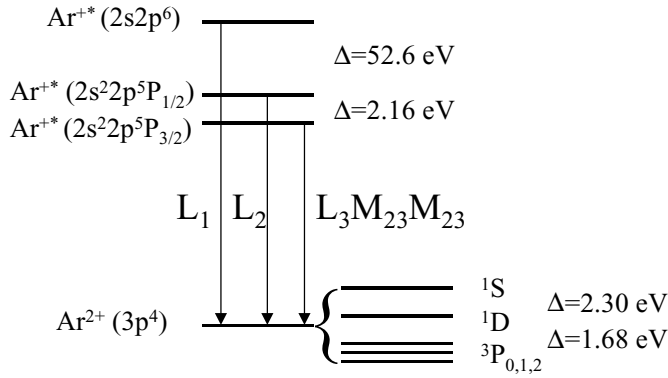


Figure 6.4: Level scheme of Ar^{+*} and Ar^{2+} including only the states that intervene in the Auger process described in this chapter.

high-energy transitions (more than 300 eV) to the K shell in C^{4+} (or eventually C^{5+}) via an Auger-decay process in argon.

An Auger process consists of photoionization from an inner shell, followed by the decay of an electron from a higher level to fill the hole, the excess energy being released in the excitation or ionization of another high-level electron. Thus two free electrons result from this process: the primary electron, which has an energy equal to the energy of the photon minus the inner-shell edge, and the Auger electron (if released into the continuum) of energy equal to the energy gained in the Auger decay minus its binding energy. The configuration of Ar is $1s^22s^22p^63s^23p^6$. L-shell photoionization can occur by removing an s (L_1) or a p (L_{23}) by a photon of more than 313 or 248 eV, respectively. The state of configuration $2p^53s^23p^6$ in Ar^{+*} is a doublet spaced by 2.16 eV (Fig. 6.4). The ground state of configuration $2p^63s^23p^4$ in Ar^{2+} is split by the spin-orbit interaction in state 1S_0 , 1D_2 , and the triplet $^3P_{0,1,2}$. Thus ten transitions of type $L_{23}M_{23}M_{23}$ can occur at energies between 201 and 207.14 eV, and five of type $L_1M_{23}M_{23}$ in the range 279 – 283 eV [143–145].

In Fig. 6.5 we present two spectra taken on Ar and He, at 0 V retarding voltage. The signal drops significantly in the Ar spectrum above 35 eV, but the main differences are the absence of peak **5** in the Ar spectrum (peak **7** can be seen on a smaller scale), and the different ratio between peaks **3** and **4** in the two spectra (although peak **3** is raised on the slope of the secondary electrons in the He spectrum). Ar spectra (or He) taken on different days showed to be quite similar to each other. More to it, we could not assign any carbon transition to peak **5**. The $5 \rightarrow 3$ transition in C^{5+} occurs indeed at 35 eV, but the amount of C^{6+} we create (if at all) is certainly too little to explain such a strong line.

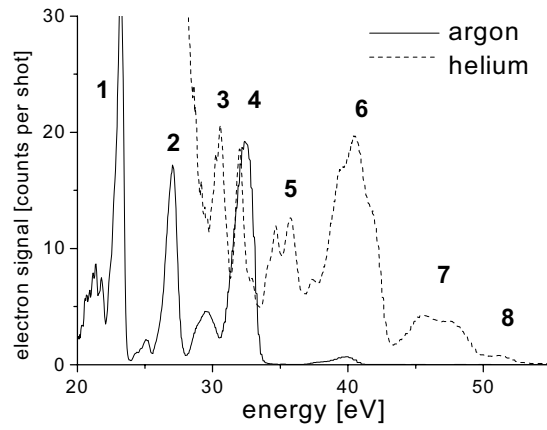


Figure 6.5: Argon (solid line) and helium (dashed line) spectra produced by ionization with photons emitted in the explosion of 50000-molecules C_3H_8 clusters, measured without retarding voltage. The spectra are scaled including the ionization potential of the detection gas.

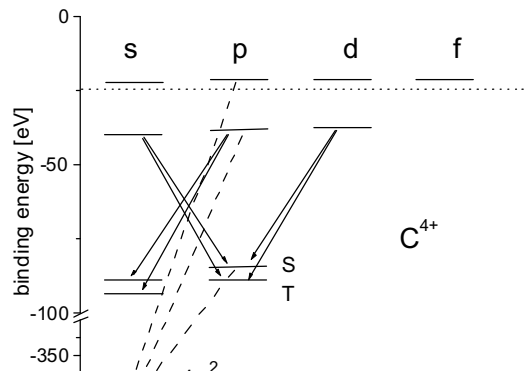


Figure 6.6: Level scheme in C^{4+} . The solid arrows indicate transitions detected directly, while the dashed arrows indicate transitions observed via an Auger-decay process in argon. The singlets and the triplets for states of $n \geq 3$ are not depicted separately. The dotted horizontal line near the top of the figure marks the binding energy of the ground state of helium. The vertical scale is broken between -100 and -300 eV.

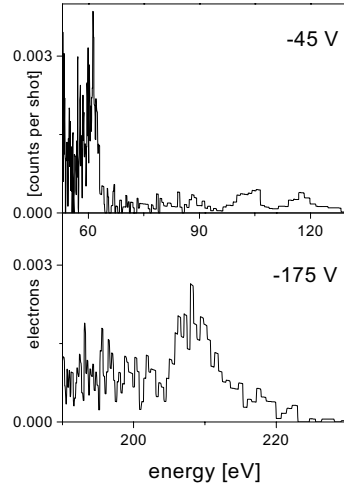


Figure 6.7: *Argon spectra at two different retarding voltages: -45 and -175 eV. The ionization potential of argon is NOT included in the energy scales.*

Peaks **1** and **2** are lines in the doubly charged carbon: the $3d \rightarrow 2p$ transitions at 21.6 eV (singlet) and 27 eV (triplet), and the triplet $3s \rightarrow 2p$ transition at 23 eV (the singlet occurs at 18 eV and cannot be seen because of the secondary electrons). The singlet $2s3p \rightarrow 2s^2$ at 32.1 eV contributes to peak **4** (see also Table I). The M-shell states in C^{2+} have binding energies between -13.6 and -15.8 eV. Population of these levels from helium should thus be energetically impossible, which makes appearance of these lines rather puzzling. The possibility exists that they are populated by charge transfer from hydrogen atoms produced by cluster explosions in the lower-intensity regions of the focus. Transitions in triply charged carbon appear in peaks **3**, **4**, and **6**: $3s, d \rightarrow 2p$ at 29.6 and 32.3 eV, $3p \rightarrow 2s$ at 40 eV. The wide peak **7** and the small peak **8** result from $3 \rightarrow 2$ transitions in C^{4+} (Fig. 6.6). There are three triplet transitions and three singlet transitions, four at energies between 45.3 and 50 eV, with $2p$ as final state, and two at 51.6 and 54.6 eV with final state $2s$.

There is no signal detected in the He spectrum after 55 eV, which suggests that there are no transitions to $n = 2$ from $n = 4, 5, \dots$ in C^{4+} (or $n = 3, 4, \dots$ in C^{5+}). Nevertheless, with Ar as detection gas, there are electrons present in the spectrum at very high energies, in the range 203 – 215 eV (Fig. 6.7b), which is the energy range of Auger electrons from $L_{23}M_{23}M_{23}$ transitions. (The $L_1M_{23}M_{23}$ transitions could not be clearly detected.) The low counting rate and the poor resolution make any attempt to distinguish individual lines futile. The peak in Fig. 6.7b sums all Auger electrons. Only transitions to the ground state in C^{4+} (or C^{5+}) have energies larger

6.4. Conclusions

than 248 eV, and they are responsible for the production of these electrons. From the low-energy spectrum we know that states of principal quantum numbers 3 or 2 are certainly populated, so we focus our attention on transitions from the singlet states $3p$ and $2p$ to the ground state. To make the identification we have to look for the primary electrons, as well. If the 308-eV (4-nm) photon emitted in the $1s2p \rightarrow 1s^2$ transition of C^{4+} L-shell ionizes Ar, an electron of 60 eV is created, while an electron of 106.4 eV is produced by the 354.4-eV (3.5-nm) photon of the deexcitation $1s3p \rightarrow 1s^2$. These electrons do appear in Fig. 6.7a as the first two peaks in the spectrum. (The energy scales of Fig. 6.7 do not include the ionization potential of Ar, they only indicate detection energies plus the retarding potential.) There is also a third peak in Fig. 6.7a, at $\simeq 118$ eV, which is most likely produced by L-shell photoionization of Ar with a 371-eV (3.3-nm) photon from the transition $1s4p \rightarrow 1s^2$, although we do not have any clear evidence from the low-energy part of the spectrum that the levels of $n = 4$ are populated. The $1s3p, 4p \rightarrow 1s^2$ transitions have very small branching ratios: 0.03 and 0.01, respectively. The main contribution to the Auger peak belongs to photons emitted in the $1s2p \rightarrow 1s^2$ transition.

The estimated total number of photons triggering the Auger decay is 0.54×10^9 , in accordance with the number given by the peaks of primary electrons. The contribution of the 4-nm photons is 67% of it, the other two lines share equally the rest.

6.4 Conclusions

From the large number of photons with energy more than 248 eV (0.54×10^9), for example, we detect only 0.015 per shot, due to our very low detection efficiency, $\simeq 3 \times 10^{-11}$. At 30 eV, also on argon, the detection efficiency is only three times larger. One conclusion of this experiment is the fact that electron spectroscopy is not an efficient method of detecting radiation, unless the detection could occur very close to the source, where the density of photons is larger.

On the other hand, it is encouraging that so many photons are produced, and that the charge-transfer process occurs with such a high probability. The total number of photons indicated by the argon spectrum is $\simeq 10^{12}$, while we estimate the numbers of carbon atoms in the focus to be $\simeq 3.5 \times 10^{12}$. If 80% of the propane molecules are forming clusters, this means 2.8×10^{12} potential emitters. C^+ and C^{2+} cannot transfer electrons from helium because of their low electron affinities, but they make only 10% of the ions. C^{5+} ions are actually able to transfer electrons three times till they reach the C^{2+} state, and C^{4+} twice. The number of potential emitters is thus 4.6×10^{12} , which gives 22% for the transfer efficiency.

We cannot estimate what sub-shells are preferentially populated, because we cannot always resolve individual lines. Nevertheless, our data confirm the fact that O^{5+} captures electrons mainly in the M shell (around 10 to 15 times more than in the N shell, including the correction for $4 \rightarrow 3$ deexcitations). All other ions capture

electrons only in the M shell, the first energetically allowed to transfer electrons from helium, except for O^{4+} , which also gets electrons in level 4s.

A rough estimate of the energy balance of the propane cluster explosion is as follows. The $\simeq 2.8 \times 10^{12}$ carbon ions carry an average kinetic energy of $\simeq 400$ eV per particle (as seen from Fig. 5.6), which makes a total of 1.1×10^{15} eV. Most of the hydrogen ions have very small kinetic energies, and we will neglect them. The energy needed to create the ions is, according to the charge-state percentages indicated by Fig. 5.4, $\simeq 0.5 \times 10^{15}$ eV. We estimated the number of electrons at $\simeq 10^{13}$, and using for the average kinetic energy per electron the value given by the numerical calculations described in **Chapter Five** ($\simeq 50$ eV, at the end of the pulse), we find a total of 0.5×10^{15} eV. We seem to produce $\simeq 10^{12}$ photons of more than 16 eV. The average energy per photon is roughly 100 eV, which amounts to 0.1×10^{15} eV. We can conclude that only a small fraction (5.5%) of the total energy of the 6-mJ pulse used in the experiment is actually absorbed by the clusters, which is consistent with our experimental observations. 23% is used for ionization, 50% of the absorbed energy is converted into ionic kinetic energy, 23% is taken by the electrons, and only 4% is converted into photons.

6.4. Conclusions

Ion	Transition	Energy [eV]	In CO ₂ [Fig. 6.3]	In C ₃ H ₈ [Fig. 6.5 Ar]
O ³⁺	3d-2p	52	4	
	3s-2p	44.3	3	
O ⁴⁺	4s-2p (S)	71	–	
	4s-2p (T)	79.4	8	
	3d-2p (S)	56.3	–	
	3d-2p (T)	64.3	–	
	2s3p-2s ²	72.3	7	
	3s-2p (S)	50	4	
	3s-2p (T)	57.6	5	
O ⁵⁺	4d-2p	95.5	10	
	4p-2s	107	11	
	4s-2p	94	10	
	3d-2p	71.7	7	
	3p-2s	82.6	9	
	3s-2p	67.4	6	
C ²⁺	3d-2p (S)	21.6		1
	3d-2p (T)	27		2
	2s3p-2s ²	32.1		4
	3s-2p (S)	18		–
	3s-2p (T)	23		1
C ³⁺	3d-2p	32.3	1	4
	3p-2s	40	2	6
	3s-2p	29.6	1	3
C ⁴⁺	3d-2p (S)	47.3		7
	3d-2p (T)	50		7
	3p-2s (S)	51.6		8
	3p-2s (T)	54.6		8
	1s3p-1s ²	354.4		Auger
	3s-2p (S)	45.3		7
	3s-2p (T)	47.5		7
	1s2p-1s ²	308		Auger

Table I. *Table of transitions.*

Bibliography

- [1] G. S. Voronov, N. B. Delone, *JETP Lett.* **1**, 66 (1965).
- [2] J. L. Hall, E. J. Robinson, L. M. Branscomb, *Phys. Rev. Lett.* **14**, 1013 (1965).
- [3] P. Agostini, F. Fabre, G. Mainfray, G. Petite, N. Rahman, *Phys. Rev. Lett.* **42**, 1127 (1979).
- [4] R. R. Freeman, P. H. Bucksbaum, H. Milchberg, S. Darack, D. Schumacher, M. E. Geusic, *Phys. Rev. Lett.* **59**, 1092 (1987).
- [5] H. G. Muller, H. B. van Linden van den Heuvell, P. Agostini, G. Petite, A. Antonetti, M. Franco, A. Migus, *Phys. Rev. Lett.* **60**, 565 (1988).
- [6] R. R. Freeman, P. H. Bucksbaum, *J. Phys. B* **24**, 325 (1991).
- [7] S. Augst, D. Strickland, D. D. Meyerhofer, S. L. Chin, J. H. Eberly, *Phys. Rev. Lett.* **63**, 2212 (1989).
- [8] E. Mevel, P. Breger, R. Trainham, G. Petite, P. Agostini, A. Migus, J. P. Chambaret, A. Antonetti, *Phys. Rev. Lett.* **70**, 406 (1993).
- [9] L. V. Keldysh, *Sov. Phys.-JETP* **20**, 1307 (1965).
- [10] H. B. van Linden van den Heuvell, H. G. Muller, in *Multiphoton Processes*, eds S. J. Smith and P. L. Knight (Cambridge: University Press) (1988).
- [11] G. G. Paulus, W. Becker, W. Nicklich, H. Walther, *J. Phys. B* **27**, L703 (1994).
- [12] G. G. Paulus, F. Grasbon, A. Dreischuh, H. Walther, *Phys. Rev. Lett.* **84**, 3770 (2000).
- [13] M. Schnürer, C. Spielmann, P. Wobrauschek, C. Strelt, N. H. Burnett, C. Kan, K. Ferencz, R. Koppitsch, Z. Cheng, T. Brabec, F. Krausz, *Phys. Rev. Lett.* **80**, 3236 (1998).

- [14] J. W. G. Tisch, D. D. Meyerhofer, T. Ditmire, N. Hay, M. B. Mason, M. H. R. Hutchinson, *Phys. Rev. Lett.* **80**, 1204 (1998).
- [15] P. M. Paul, E. S. Toma, P. Breger, G. Mullot, F. Augé, Ph. Balcou, H. G. Muller, P. Agostini, *Science* **292**, 1689 (2001).
- [16] T. M. Shuman, M. E. Anderson, J. Bromage, C. Iaconis, L. Waxer, I. A. Walm-
sley, *Optics Express* **5**, 134 (1999).
- [17] A. L'Huillier, L. A. Lompré, G. Mainfray, C. Manus, *Phys. Rev. A* **27**, 2503
(1983).
- [18] B. Walker, E. Mevel, B. Yang, P. Breger, P. Agostini, L. F. DiMauro, *Phys.*
Rev. A **48**, R894 (1994).
- [19] D. Charalambidis, P. Lambropoulos, H. Schröder, O. Faucher, H. Xu, M. Wag-
ner, C. Fotakis, *Phys. Rev. A* **50**, R2822 (1994).
- [20] D. N. Fittinghoff, P. R. Bolton, B. Chang, K. C. Kulander, *Phys. Rev. Lett.* **69**,
2642 (1992).
- [21] B. Walker, B. Sheehy, L. F. DiMauro, P. Agostini, K. J. Schafer, K. C. Kulander,
Phys. Rev. Lett. **73**, 1227 (1994).
- [22] H. G. Muller, *Optics Express* **8**, 417 (2001).
- [23] Results to be published.
- [24] K. Burnett, V. C. Reed, P. L. Knight, *J. Phys. B* **26**, 561 (1993).
- [25] J. Parker, C. R. Stroud, Jr., *Phys. Rev. A* **40**, 5651 (1989).
- [26] M. V. Fedorov, M. Yu. Ivanov, A. M. Movsesian, *J. Phys. B* **23**, 2245S (1990).
- [27] B. Piraux, E. Huens, P. Knight, *Phys. Rev. A* **44**, 721 (1991).
- [28] R. R. Jones, P. H. Bucksbaum, *Phys. Rev. Lett.* **67**, 3215 (1991).
- [29] J. H. Hoogenraad, R. B. Vrijen, L. D. Noordam, *Phys. Rev. A* **50**, 4133 (1994).
- [30] M. Pont, M. Gavrilă, *Phys. Rev. Lett.* **65**, 2362 (1990).
- [31] C. K. Law, Q. Su, J. H. Eberly, *Phys. Rev. A* **44**, 7844 (1991).
- [32] R. J. Vos, M. Gavrilă, *Phys. Rev. Lett.* **68**, 170 (1992).
- [33] M. P. de Boer, J. H. Hoogenraad, R. B. Vrijen, R. C. Constantinescu, L. D.
Noordam, H. G. Muller, *Phys. Rev. A* **50**, 4085 (1994).

- [34] N. J. van Druten, R. C. Constantinescu, J. M. Schins, H. Nieuwenhuize, H. G. Muller, *Phys. Rev. A* **55**, 622 (1997).
- [35] R. C. Elton, *X-Ray Lasers* (San Diego: Academic Press) (1990).
- [36] D. L. Matthews *et al.*, *Phys. Rev. Lett.* **54**, 110 (1985).
- [37] B. J. MacGowan, S. Maxon, L. B. Da Silva, D. J. Fields, C. J. Keane, D. L. Matthews, A. L. Osterheld, J. H. Scofield, G. Shinkaveg, G. F. Stone, *Phys. Rev. Lett.* **65**, 420 (1990).
- [38] B. E. Lemoff, G. Y. Yin, C. L. Gordon III, C. P. J. Barty, S. E. Harris, *Phys. Rev. Lett.* **74**, 1574 (1995).
- [39] H. C. Kapteyn, R. W. Lee, R. W. Falcone, *Phys. Rev. Lett.* **57**, 2939 (1986).
- [40] S. Suckewer, C. H. Skinner, H. Milchberg, C. Keane, D. Voorhees, *Phys. Rev. Lett.* **55**, 1753 (1985).
- [41] N. H. Burnett, P. B. Corkum, *J. Opt. Soc. Am. B* **6**, 1195 (1989).
- [42] P. Amendt, D. C. Eder, S. C. Wilks, *Phys. Rev. Lett.* **66**, 2589 (1991).
- [43] Y. Nagata, K. Midorikawa, S. Kubodera, M. Obara, H. Tashiro, K. Toyoda, *Phys. Rev. Lett.* **71**, 3774 (1993).
- [44] M. Murphy, C. Glasheen, F. A. Moscatelli, T. D. Donnelly, *Phys. Rev. A* **55**, R2543 (1997).
- [45] M. Ferray, A. L'Huillier, X. F. Li, L. A. Lompré, G. Mainfray, C. Manus, *J. Phys. B: At. Mol. Opt. Phys.* **21**, L31 (1988).
- [46] X. F. Li, A. L'Huillier, M. Ferray, L. A. Lompré, G. Mainfray, *Phys. Rev. A* **39**, 5751 (1989).
- [47] A. L'Huillier, L. A. Lompré, G. Mainfray, C. Manus, in *Atoms in Intense Laser Fields*, ed M. Gavrilá (New York: Academic Press), p 139 (1992).
- [48] A. L'Huillier, Ph. Balcou, S. Candel, K. J. Schafer, K. C. Kulander, *Phys. Rev. A* **46**, 2778 (1992).
- [49] P. Salières, A. L'Huillier, M. Lewenstein, *Phys. Rev. Lett.* **74**, 3776 (1995).
- [50] M. Lewenstein, P. Salières, A. L. Huillier, *Phys. Rev. A* **52**, 4747 (1995).
- [51] Ph. Balcou, P. Salières, A. L'Huillier, M. Lewenstein, *Phys. Rev. A* **55**, 3204 (1997).

- [52] P. B. Corkum, *Phys. Rev. Lett.* **71**, 1994 (1993).
- [53] K. J. Schafer, K. C. Kulander, *OSA Proceedings on Shortwavelength V, Vol. 17*, eds P. B. Corkum and M. D. Perry, p108 (1993).
- [54] A. L'Huillier, M. Lewenstein, P. Salières, Ph. Balcou, M. Yu. Ivanov, J. Larsson, C. G. Wahlström, *Phys. Rev. A* **48**, R3433 (1993).
- [55] M. Lewenstein, Ph. Balcou, M. Yu. Ivanov, A. L'Huillier, P. B. Corkum, *Phys. Rev. A* **49**, 2117 (1994).
- [56] W. Becker, A. Lohr, M. Kleber, M. Lewenstein, *Phys. Rev. A* **56**, 645 (1997).
- [57] A. L'Huillier, Ph. Balcou, L. A. Lompré, *Phys. Rev. Lett.* **68**, 166 (1992).
- [58] Ph. Balcou, A. L'Huillier, *Phys. Rev. A* **47**, 1447(1993).
- [59] J. K. Crane, S. W. Allendorf, K. S. Budil, M. D. Perry, *OSA Proceedings on ShortWavelength Coherent Radiation*, Vol. **11**, eds P. H. Bucksbaum and N. M. Ceglio, p 28 (1991).
- [60] K. Miyazaki, H. Sakai, *J. Phys. B: At. Mol. Opt. Phys.* **25**, L83 (1992).
- [61] B. W. Shore, P. L. Knight, *J. Phys. B: At. Mol. Opt. Phys.* **20**, 413 (1987).
- [62] J. H. Eberly, Q. Su, J. Javanainen, *Phys. Rev. Lett.* **62**, 881 (1989).
- [63] J. H. Eberly, Q. Su, J. Javanainen, *J. Opt. Soc. Am. B* **6**, 1289 (1989).
- [64] K. J. Schafer, B. Yang, L. F. DiMauro, K. C. Kulander, *Phys. Rev. Lett.* **70**, 1599 (1993).
- [65] B. Yang, K. J. Schafer, B. Walker, K. C. Kulander, P. Agostini, L. F. DiMauro, *Phys. Rev. Lett.* **71**, 3770 (1993).
- [66] M. P. Hertlein, P. H. Bucksbaum, H. G. Muller, *J. Phys. B: At. Mol. Opt. Phys.* **30**, L197 (1997).
- [67] H. G. Muller, F. C. Kooiman, *Phys. Rev. Lett.* **81**, 1207 (1998).
- [68] H. G. Muller, *Laser Physics* **9**, 138 (1999).
- [69] Ph. Antoine, A. L'Huillier, M. Lewenstein, P. Salières, B. Carre, *Phys. Rev. A* **53**, 1725 (1996).
- [70] M. B. Gaarde, Ph. Antoine, A. L'Huillier, K. J. Schafer, K. C. Kulander, *Phys. Rev. A* **57**, 4553 (1998).
- [71] H. G. Muller, *Phys. Rev. A* **60**, 1341 (1999).

- [72] J.P. Zhou *et al.*, *Opt. Lett.* **20**, 64 (1995).
- [73] I. D. Jung, F. X. Kärtner, N. Matuschek, D. H. Sutter, F. Morier-Genoud, G. Zhang, U. Keller, V. Scheuer, M. Tilsch, T. Schudi, *Opt. Lett.* **22**, 1009 (1997).
- [74] K. Yamakawa, M. Aoyama, S. Matsuoka, H. Takuma, *Opt. Lett.* **23**, 525 (1998).
- [75] L. Xu, G. Tempea, Ch. Spielmann, F. Krausz, A. Stingl, K. Ferencz, S. Takano, *Opt. Lett.* **23**, 789 (1998).
- [76] A. Baltuska, Z. Wei, M. S. Pshenichnikov, D. A. Wiersma, *Opt. Lett.* **22**, 102 (1997).
- [77] S. Sartania, Z. Cheng, M. Lenzner, G. Tempea, Ch. Spielmann, F. Krausz, K. Ferencz, *Opt. Lett.* **22**, 1562 (1997).
- [78] A. Brun, P. Georges, G. Le Saux, F. Salin, *J. Phys. D* **24**, 1225 (1991).
- [79] Y. Gontier, N.K. Rahman, M. Trahin, *Phys. Rev. A* **34**, 1112 (1986).
- [80] Y. Kobayashi, T. Sekikawa, Y. Nabekawa, S. Watanabe, *Opt. Lett.* **23**, 64 (1998).
- [81] T. Sekikawa, T. Ohno, T. Yamazaki, Y. Nabekawa, S. Watanabe, *Phys. Rev. Lett.* **83**, 2564 (1999).
- [82] T.E. Glover, R. W. Schoenlein, A. H. Chin, C. V. Shank, *Phys. Rev. Lett.* **76**, 2468 (1996).
- [83] J. M. Schins, P. Breger, P. Agostini, R. C. Constantinescu, H. G. Muller, A. Bouhal, G. Grillon, A. Antonetti, A. Mysyrowicz, *J. Opt. Soc. Am. B* **13**, 197 (1996).
- [84] A. Bouhal, R. Evans, G. Grillon, A. Mysyrowicz, P. Breger, P. Agostini, R. C. Constantinescu, H. G. Muller, D. von der Linde, *J. Opt. Soc. Am. B* **14**, 950 (1997).
- [85] A. Bouhal, P. Salieres, P. Breger, P. Agostini, G. Hamoniaux, A. Mysyrowicz, A. Antonetti, R. Constantinescu, H. G. Muller, *Phys. Rev. A* **58**, 389 (1998).
- [86] J.M. Schins, P. Breger, P. Agostini, R. C. Constantinescu, H. G. Muller, G. Grillon, A. Antonetti, A. Mysyrowicz, *Phys. Rev. Lett.* **73**, 2180 (1994).
- [87] M.H. Sher, U. Mohideen, H. W. K. Tom, O. R. Wood II, G. D. Aumiller, R. R. Freeman, T. J. McIlrath, *Opt. Lett.* **18**, 646 (1993).
- [88] Y. Kobayashi, O. Yoshihara, Y. Nabekawa, K. Kondo, S. Watanabe, *Opt. Lett.* **21**, 417 (1996).

- [89] S.P. Le Blanc, Z. Qi, R. Sauerbrey, *Opt. Lett.* **20**, 312 (1995).
- [90] E. Constant, V. D. Taranukhin, A. Stolow, P. B. Corkum, *Phys. Rev. A* **56**, 3870 (1997).
- [91] M.D. Davidson, J. Wals, H. G. Muller, H. B. van Linden van der Heuvell, *Phys. Rev. Lett.* **71**, 2192 (1993).
- [92] K.J. Schafer and K.C. Kulander, *Phys. Rev. Lett.* **78**, 638 (1997).
- [93] P. Salières, A. L’Huillier, P. Antoine, M. Lewenstein, in *Adv. At. Mol. Opt. Phys.* **41**, eds B. Bederson and H. Walther (New York: Academic Press), p 83 (1999).
- [94] A. E. Kaplan, *Phys. Rev. Lett.* **73**, 1243 (1994).
- [95] A. V. Sokolov, D. R. Walker, D. D. Yavuz, G. Y. Yin, S. E. Harris, *Phys. Rev. Lett.* **85**, 562 (2000).
- [96] M. Ivanov, P. B. Corkum, T. Zuo, A. Bandrauk, *Phys. Rev. Lett.* **74**, 2933 (1995).
- [97] E. S. Toma, H. G. Muller, P. M. Paul, P. Breger, M. Cheret, P. Agostini, C. Le Blanc, G. Mullot, G. Cheriaux, *Phys. Rev. A* **62**, 061801(R) (2000).
- [98] M. Drescher, M. Hentschel, R. Kienberger, G. Tempea, Ch. Spielmann, G. Reider, F. Krausz, *Science* **291**, 1923 (2001).
- [99] G. Farkas, C. Toth, *Phys. Lett. A* **168**, 447 (1992).
- [100] S. E. Harris *et al.*, *Opt. Commun.* **100**, 487 (1993).
- [101] P. Antoine, A. L’Huillier, M. Lewenstein, *Phys. Rev. Lett.* **77**, 1234 (1996).
- [102] P. Antoine, D. B. Milošević, A. L’Huillier, M. B. Gaarde, P. Salières, M. Lewenstein, *Phys. Rev. A* **56**, 4960 (1997).
- [103] I. P. Christov, M. M. Murnane, H. C. Kapteyn, *Phys. Rev. A* **57**, 2285 (1998).
- [104] N. A. Papadogiannis, B. Witzel, C. Kalpouzos, D. Charalambidis, *Phys. Rev. Lett.* **83**, 4289 (1999).
- [105] V. Veniard, R. Taïeb, A. Maquet, *Phys. Rev. A* **54**, 721 (1996).
- [106] S. Klarsfeld, A. Maquet, *J. Phys. B* **12**, L553 (1979).
- [107] M. Aymar, M. Crance, *J. Phys. B* **13**, L287 (1980).

- [108] L. F. DiMauro, P. Agostini, in *Adv. At. Mol. Opt. Phys.* **35**, eds B. Bederson and H. Walther (New York: Academic Press), p 79 (1995).
- [109] M. Protopapas, C. H. Keitel, and P. L. Knight, *Rep. Prog. Phys.* **60**, 389 (1997).
- [110] A. McPherson, B. D. Thompson, A. B. Borisov, K. Boyer, and C. K. Rhodes, *Nature* **370**, 631 (1994).
- [111] T. Ditmire, T. Donnelly, R. W. Falcone, and M. D. Perry, *Phys. Rev. Lett.* **75**, 3122 (1995).
- [112] S. Dobosz, M. Leszius, M. Schmidt, P. Meynadier, M. Perdrix, and D. Normand, *Phys. Rev. A* **56**, R2526 (1997).
- [113] T. Ditmire, J. Zweiback, V. P. Yanovsky, T. E. Cowan, G. Hays, and K. B. Wharton, *Nature* **398**, 489 (1999).
- [114] T. Ditmire, J. W. G. Tisch, E. Springate, M. B. Mason, N. Hay, R. A. Smith, J. Marangos, and M. H. R. Hutchinson, *Nature* **386**, 54 (1997).
- [115] T. Ditmire, J. W. G. Tisch, E. Springate, M. B. Mason, N. Hay, J. P. Marangos, and M. H. R. Hutchinson, *Phys. Rev. Lett.* **78**, 2732 (1997).
- [116] T. Ditmire, E. Springate, J. W. G. Tisch, Y. L. Shao, M. B. Mason, N. Hay, J. P. Marangos, and M. H. R. Hutchinson, *Phys. Rev. A* **57**, 369 (1998).
- [117] Y. L. Shao, T. Ditmire, J. W. G. Tisch, E. Springate, J. P. Marangos, and M. H. R. Hutchinson, *Phys. Rev. Lett.* **77**, 3343 (1996).
- [118] B. D. Thompson, A. McPherson, K. Boyer, and C. K. Rhodes, *J. Phys. B* **27**, 4391 (1994).
- [119] A. McPherson, T. S. Luk, B. D. Thompson, A. B. Borisov, O. B. Shiryaev, X. Chen, K. Boyer, and C. K. Rhodes, *Phys. Rev. Lett.* **72**, 1810 (1994).
- [120] E. M. Snyder, S. A. Buzza, and A. W. Castleman, Jr., *Phys. Rev. Lett.* **77**, 3347 (1996).
- [121] C. Rose-Petruck, K. J. Schafer, K. R. Wilson, and C. P. J. Barty, *Phys. Rev. A* **55**, 1182 (1997).
- [122] T. Ditmire, *Phys. Rev. A* **57**, R4049 (1998).
- [123] T. Ditmire, T. Donnelly, A. M. Rubenchik, R. W. Falcone, and M. D. Perry, *Phys. Rev. A* **53**, 3379 (1996).
- [124] J. Zweiback, T. Ditmire, and M. D. Perry, *Phys. Rev. A* **59**, R3166 (1999).

- [125] M. Lezius, S. Dobosz, D. Normand, and M. Schmidt, *Phys. Rev. Lett.* **80**, 261 (1998).
- [126] E. Springate, N. Hay, J. W. G. Tisch, M. B. Mason, T. Ditmire, M. H. R. Hutchinson, and J. P. Marangos, *Phys. Rev. A* **61**, 063201 (2000).
- [127] R. C. Constantinescu, S. Hunsche, H. B. van Linden van den Heuvell, H. G. Muller, C. LeBlanc, and F. Salin, *Phys. Rev. A* **58**, 4637 (1998).
- [128] O. F. Hagen and W. Obert, *J. Chem. Phys.* **56**, 1793 (1972).
- [129] O. F. Hagen, *Surface Science* **106**, 101 (1981).
- [130] O. F. Hagen, *Z. Phys. D* **4**, 291 (1987).
- [131] O. F. Hagen, *Rev. Sci. Instrum.* **63**, 2374 (1991).
- [132] O. F. Hagen, *The Physics of Fluids* **17**, 894 (1974).
- [133] J. Farges, M. F. de Feraudy, B. Raoult, and G. Torchet, *J. Chem. Phys.* **84**, 3491 (1986).
- [134] J. Wörmer, V. Guzielski, J. Stapelfeldt, and T. Möller, *Chem. Phys. Lett.* **159**, 321 (1989).
- [135] D. R. Miller, in *Atomic and Molecular Beam Methods*, ed by G. Scoles (Oxford: Univ. Press), vol. I, p 14 (1988).
- [136] W. Lotz, *Z. Phys.* **216**, 241 (1968).
- [137] I. Last, and J. Jortner, *Phys. Rev. A* **62**, 013201 (2000).
- [138] N. B. Delone, and V. P. Krainov, *Physics-Uspekhi* **41**, 469 (1998).
- [139] R. E. Olson, A. Salop, *Phys. Rev. A* **77**, 531 (1977).
- [140] J. P. M. Beijers, R. Hoekstra, A. R. Schlatmann, R. Morgenstern, F. J. de Heer, *J. Phys. B* **25**, 463 (1992).
- [141] J. Berkowitz, *Photoabsorption, Photoionization, and Photoelectron Spectroscopy* (New York: Academic Press) (1979).
- [142] C. E. Moore, *Atomic Energy Levels* (Circular of the National Bureau of Standards 467) (1949).
- [143] K. G. Dyall, F. P. Larkins, *J. Phys. B* **15**, 2793 (1982).
- [144] J. Bruneau, *J. Phys. B* **16**, 4135 (1983).
- [145] J. M. Schins, P. Breger, P. Agostini, R. C. Constantinescu, H. G. Muller, G. Grillon, A. Antonetti, A. Mysyrowicz, *Phys. Rev. A* **52**, 1272 (1995).

Summary

This thesis is concerned with two main topics: a study of the process of high-harmonic generation (HHG), and a study of the interaction of clusters with infrared laser radiation.

The process of HHG results in the emission of radiation at multiples of the incident light frequency, when a laser beam is focused into a gaseous medium, due to the non-linear response of the medium. The highest efficiencies are obtained when the medium consists of rare-gas atoms. Because of the symmetry of the atoms, only odd frequencies are emitted. The power spectrum of the harmonic emission, consisting of equidistant peaks, spaced by twice the frequency of the driving field, can be easily measured either by detection on a light-sensitive detector, after diffraction on a grating, or by detection in an electron spectrometer, after ionizing a detection gas. The last method was used in our experiments.

The power spectrum gives direct information about the intensities of the harmonic fields, and about the emission efficiency. The width of the peaks is related to the duration of the harmonic pulses (that is the pulses corresponding to individual harmonic fields), but even if these pulses were bandwidth limited, this information is hard to extract because of additional broadening in the detection process. Because the harmonic generation is very sensitive to the intensity, only the most intense part of the driving pulse contributes to the process and the harmonic pulses are shorter than the fundamental. The temporal profile of the harmonic emission (that is the sum of all harmonic fields) cannot be measured directly, because there is no device sensitive enough to resolve this process, which occurs on a very fast scale, in the attosecond range.

In a strong field, the ionization threshold and the high Rydberg states of the atoms are Stark shifted to higher energies, linearly in the intensity of the incident field. At certain intensities, some bound states are shifted into resonance with a multiple number of incident photons. If so, it happens that the radiation emitted by deexcitation to the ground state is strongly enhanced, increasing the emission efficiency at that wavelength. The harmonic-emission dependence on intensity, and the occurrence of resonant enhancement are studied in the second chapter of the

thesis. The intensity resolution was increased using a spatially-shaped incident pulse, which produced a homogeneous intensity distribution in the focus.

The duration of the high-order harmonics can be so short (a few femtoseconds) that it is hard to find a shorter and more intense pulse of known profile, to make a cross-correlation measurement possible. Correlation of the harmonic pulse with itself or with a higher harmonic is not possible because of the very low efficiency of non-linear processes, like two-photon ionization, at these short wavelengths and low intensities of the harmonics. Chapter Three describes a new method for the measurement of ultrashort pulses of short wavelength, based on the ponderomotive streaking of the atomic ionization potential in the presence of a strong infrared pulse, of longer duration. The method uses a process of single-photon ionization with the harmonics, in an atomic environment which is changing in time according to the variation of the infrared intensity. The temporal profile of the infrared intensity acts as a time scale on which the much shorter harmonic pulses can be measured via the changes that appear in the photoelectron spectrum (mainly shift and extra broadening of the peaks), at different delays with respect to the infrared.

A weaker pulse of the frequency of the fundamental, unable to induce a shift of the ionization threshold of the atoms, can be very useful for the more interesting matter regarding the reconstruction of the temporal profile of the total harmonic emission. Two-photon, two-color ionization causes two new peaks to appear on either side of the harmonic peak. To reconstruct the total field, we need, besides the relative amplitudes of the harmonics given by the power spectrum, also information about the relative phases of the harmonic fields. The intermediate peaks (sidebands) which appear equidistantly in between the harmonic peaks, are the result of interferences between transitions involving only the neighbouring harmonics and the dressing field. This makes their amplitudes proportional to a cosine function of the phase difference between the contributing harmonics. Doing a measurement at different delays between the weak pulse and the harmonics, we can map these cosine functions in time, and extract the phase differences between consecutive harmonics, from which the relative phases of all harmonics easily follow. The experiment is described in Chapter Four.

The second part of the thesis is concerned with a study of cluster explosions. Clusters are conglomerates of atoms or molecules bound together by Van-der-Waals forces, which, because of their high local density, absorb the laser radiation more efficiently than single particles. As a consequence, very fast highly charged ions and hot electrons are produced at reasonably low laser intensities. Our study is focused on clusters of carbon-containing molecules (propane and carbon dioxide).

The fifth chapter is a study of the ion production from clusters. The measured charge distributions and ion energies are presented, together with a theoretical model of the laser-cluster interaction, which gives a valuable description of the explosion process.

The highly charged ions are a very useful material for radiation emission at very short wavelengths. If the clusters are mixed with a noble gas, insensitive to the laser

in terms of ionization, the cluster explosion will be followed by collisions between the highly charged ions and the noble-gas atoms. Such a collision can result in resonant charge transfer from the neutral to an excited state of the ion, from where the electron decays with certain probability to the ground state, emitting a photon of very short wavelength. This radiation emission is studied in Chapter Six, and conversion efficiencies at some high frequencies are presented.

Samenvatting

Dit proefschrift handelt over twee onderwerpen: de studie van de opwekking van hogere harmonischen (high-harmonic generation, HHG), en de studie van de interactie van clusters met infrarood laserlicht.

Bij HHG wordt straling gemaakt bij frequenties die een veelvoud zijn van de frequentie van het bronlicht, door dit licht te focuseren in een gas. De productie van harmonischen is een gevolg van niet-lineaire eigenschappen van het gas. De hoogste efficiënties worden gehaald wanneer edelgassen worden gebruikt. Door de symmetrie van de atomen worden alleen oneven harmonischen geproduceerd (licht bij frequenties die een oneven veelvoud zijn van die van het oorspronkelijke licht).

Het 'power spectrum' van de geproduceerde harmonischen bestaat uit pieken op gelijke afstand, gelijk aan tweemaal de frequentie van het oorspronkelijke licht, en kan eenvoudig gemeten worden met een ultra-violet lichtgevoelige detector of door middel van een electron spectrometer na ionisatie van een detectiegas. De laatste methode is gebruikt in onze experimenten. Het power spectrum geeft directe informatie over de intensiteiten van de harmonischen en over de opbrengst. De breedte van de pieken hangt samen met de pulsduur van de bijbehorende harmonische, maar zelfs als de pulsen bandbreedte-begrensd zijn is het moeilijk deze breedte te bepalen als gevolg van verbredings processen tijdens de detectie. Omdat de opwekking van harmonischen zeer sterk afhangt van de licht-intensiteit, draagt alleen het meest intense deel van het bronlicht bij aan de generatie, met als gevolg dat de harmonische pulsen korter zijn dan de bronpuls. Het tijdsprofiel van de uitgezonden harmonischen, dat wil zeggen van de som der harmonischen, kan niet direct gemeten worden, omdat geen apparaat snel genoeg is om deze attoseconde pulsen te meten.

In een sterk electro-magnetisch veld verschuiven de ionisatie-limiet en de hoge Rydberg toestanden van de atomen naar hogere energieën. De mate van verschuiving is evenredig met de intensiteit van het veld. Bij bepaalde intensiteiten schuiven sommige gebonden toestanden in resonantie met een veelvoud van de lichtfrequentie. Hierdoor kan de straling die wordt uitgezonden bij de-excitatie naar de grondtoestand versterkt worden. De opbrengst van straling bij die golflengte neemt dan sterk toe. De afhankelijkheid van de harmonischen-emissie van intensiteit, en het optreden van

resonante versterking worden bestudeerd in het tweede hoofdstuk van dit proefschrift. De intensiteits-resolutie werd verhoogd door gebruik te maken van een ruimtelijk gevormde bronpuls, waardoor in het focus een homogene intensiteit werd verkregen.

De duur van hogere-orde harmonische pulsen kan zo kort zijn (enkele femtoseconden) dat het moeilijk is een puls te vinden met bekend tijdsprofiel, die voldoende kort en intens is om te gebruiken in een cross-correlatie meting. Correlatie van de harmonische puls met zichzelf of met een hogere harmonische is niet mogelijk door de lage efficiëntie van niet-lineaire processen, zoals twee-foton ionisatie, bij de korte golflengtes en lage intensiteiten van de harmonischen. In Hoofdstuk Drie wordt een nieuwe methode voor de meting van ultrakorte pulsen bij korte golflengtes beschreven, die is gebaseerd op de snelle verschuiving van de atomaire ionisatie-potentiaal in aanwezigheid van een sterke infrarode puls. De methode is gebaseerd op ionisatie door een enkel harmonische foton in een atomaire omgeving die in de tijd verandert door verandering van de intensiteit van het infrarode licht. Het tijdsprofiel van het infrarode licht werkt als een tijdsschaal waarop de veel kortere harmonische pulsen gemeten kunnen worden via de veranderingen die zichtbaar zijn in het fotoelectronspectrum (voornamelijk verschuiving en extra verbreding van de pieken) op verschillende tijden na het infrarode licht.

Een zwakkere puls met de frequentie van de bronpuls, te zwak om een verandering in de ionisatie-potentiaal van de atomen te induceren, kan gebruikt worden voor de meer interessante reconstructie van het tijdsprofiel van de totale harmonischen-emissie. Twee-foton, twee-kleuren ionisatie leidt tot het verschijnen van twee nieuwe pieken ("zijbanden") aan weerszijden van de harmonische piek. Om het totale veld te reconstrueren hebben we, behalve de relatieve amplitudes van de harmonischen, gegeven door het power spectrum, ook hun relatieve fasen nodig. De zijbanden die midden tussen de harmonischen verschijnen, zijn het gevolg van interferenties tussen overgangen die verband houden met naburige harmonischen en het infrarood veld. Dit maakt dat hun amplitudes afhangen van de cosinus van het faseverschil tussen de bijdragende harmonischen. Door met verschillende vertragingen tussen de zwakke puls en de harmonischen te meten, kunnen we deze cosinus functie als functie van de tijd bepalen. Hieruit vinden we de faseverschillen tussen opeenvolgende harmonischen, waarna de bepaling van de faseverschillen van alle harmonischen een koud kunstje is. Dit experiment wordt beschreven in Hoofdstuk Vier.

Het tweede deel van het proefschrift beschrijft een studie van cluster-explosies. Clusters zijn door Van-der-Waals krachten bijeengehouden conglomeraties van atomen of moleculen die, door hun hoge lokale dichtheid en de resulterende hoge botsingskans van de fragmenten, laserlicht veel efficiënter absorberen dan enkele deeltjes. Hierdoor kunnen reeds bij vrij lage laser-intensiteiten in zeer korte tijd sterk geladen ionen en hete electronen worden geproduceerd. Onze studie is gericht op clusters van koolstof-bevattende moleculen (propaan en koolstofdioxide).

Het vijfde Hoofdstuk bevat een studie naar de ionen productie uit clusters. De gemeten ladingsverdelingen en ionen-energieën worden gepresenteerd, samen met een

theoretisch model van de laser-cluster interactie. Hiermee wordt een waardevolle beschrijving van het proces van de explosie verkregen.

De sterk geladen ionen vormen een zeer bruikbaar materiaal voor de productie van straling bij zeer korte golflengtes. Als de clusters worden gemengd met een edelgas, dat zelf niet door de laser kan worden geïoniseerd, zal de cluster-explosie worden gevolgd door botsingen tussen de sterk geladen ionen en de edelgas-atomen. Zo'n botsing kan een resonante ladingsoverdracht van de neutrale naar een geëxciteerde toestand van het ion tot gevolg hebben, waarna het electron met een zekere waarschijnlijkheid vervalt naar de grondtoestand onder uitzending van een foton met een zeer korte golflengte. Deze uitzending van straling wordt bestudeerd in Hoofdstuk Zes, waarin tevens conversie efficiënties bij sommige hoge frequenties worden gepresenteerd.

Acknowledgment

The moment of the thesis defence has come. It is a great feeling to receive the final reward after more than four years of hard and challenging work. This work might not have been so successful, and certainly not so pleasant without the help of the wonderful people from FOM-Amolf Institute, whose kindness and diligence I shall always remember. There are not many places like Amolf on this planet, and I will always be grateful that I have been given the chance to work at this institute.

The person who helped me most with my work (experiments and papers) is my promotor, prof. Dr. Harm Geert Muller. I warmly thank him for his intelligent solutions, generously given in critical situations, for his wise advice, not necessarily scientific, and for the many interesting things I have learn from him during all these years. I might well live fifty years from now, and never meet again another person with such a brilliant and comprehensive mind as Harm. I was very happy to work with him, and to enjoy his 'broadband' conversations, which I will certainly miss.

It was a great pleasure for me to meet Dr. Pierre Agostini, and to work with him during the time I spent in Palaiseau, France, using the laser facilities of Laboratoire d'Optique Applique. If his important contribution to the physics of atoms in strong laser fields was well-known to me before, I was happy to discover, after meeting him, a very kind person, with a very elegant way of expressing himself.

The first person to tell me about Amolf, strongly encouraging me to apply here for a Ph.D. position, was Dr. Mihai Gavrilă, to whom I am most grateful. Afterwards, he was always interested in the progress of my experiments, and he always encouraged me.

I generally thank to all my professors from the University of Bucharest for helping me enlarge my knowledge of physics, and building the basis on which my further development occurred.

I would like to mention now few other people, who helped me in doing the experiments and writing the papers: Dr. Philippe Antoine and Dr. Armelle de Bohan from Belgium, Pierre Marie Paul (soon to become Dr.) and Pierre Breger from France. Many thanks to all of them, and my best wishes for the future!

I am also very grateful to the technicians from Amolf, especially to Rob, Anton,

Ilja, Ad, and Don Hincote, to Wim Brouwer and his people from the workshop, to the people from E&I, and from the 'Constructie Bureau', for their generous and effective support. I thank to Hans Zeijlemaker for his help in providing, in time and in abundance, all the gases I needed for my experiments. I also mention the scientists and technicians from LOA that helped me with the experiments I did in Palaiseau. The contribution of all these people to the success of my experiments was very important.

Special thanks to Dirk-Jan for helping me with the design of the cover of this thesis, and to Michel for his help with the Dutch summary.

I would not have managed with all the papers and documents necessary for my residence in Holland without the help of the personal officers, Esther, Danielle, and Wouter, to whom I kindly thank. I thank to the librarians, Saskia, Elin, Ingrid, and Kirsten for their help with the submission of my papers. I also thank to Piet Kistemaker and all the people from the administration for their help. I am very grateful to the ladies from the reception for the many Xs they put for me in the presence list, every time I arrived at the institute after half past nine in the morning. I express my gratitude to Ed Kruller for telling me so many things about Holland, and, especially, about the Dutch soccer.

My life in Holland and at Amolf would not have been so charming without the presence of Florentina and Nicu, Anouk and Pascal, Georgiana and Stella, Roxana and Iulian. I thank them all, and I wish them all the best! I am very grateful to Raluca and Marc Paul for the kindness they have showed me since I moved to Amsterdam, and for their help in getting used to the place and the people. My special thanks to the rest of the Romanian community at Amolf: Laura, Cătălin Primero, and Cătălin Segundo. I thank to all the other people in the groups of Marc, Bart, Huib, Wim and Jook for being such nice colleagues, and I apologize that, for the sake of brevity, I do not mention all of them by name.

My thoughts turn now to my friends from Romania, especially to Mirela, Mihai, and Simona, whose moral support was very helpful for me, and whose visits in Holland made me very happy.

I thank with all my heart to my parents, my grandparents and my brother for their love, and for everything they did for me.

Le mulțumesc părinților și bunicilor mei pentru dragostea lor și pentru tot ce au făcut pentru mine, fără de care nimic nu ar fi fost cu putință. Îi mulțumesc deasemenea fratelui meu Adrian, pe care am putut mereu conta și a cărui prezență în Olanda îmi e de mare ajutor sufletec, și îi urez multă fericire alături de soția lui, Mariana. Vouă tuturor vă dedic această teză împreună cu dragostea și recunoștința mea.

Elena Monica, December 2001.

Curriculum Vitae

Elena-Simona Toma was born on October 20, 1972, in Bucharest, Romania. From 1987 to 1991 she studied at the Computers High School (Liceul de Informatică) in the same city. Afterwards, from 1991 to 1996, she attended the courses of the Faculty of Physics, at the University of Bucharest. She specialized in Atomic and Molecular Physics. She came to Amsterdam in 1997, when she started her Ph.D. research at FOM-Amolf Institute, in the group of prof. Dr. Harm Geert Muller.